Dissertation

submitted to the

Combined Faculties of the Natural Sciences and Mathematics
of the Ruperto-Carola University of Heidelberg, Germany

for the degree of

Doctor of Natural Sciences

Put forward by

Dipl.-Phys. Michael Haas

born in Wuppertal, Germany

Oral examination: December 10, 2014

Spectral functions in finite temperature SU(3) gauge theory and applications to transport phenomena

Referees: Prof. Dr. Jan M. Pawlowski
Prof. Dr. Jörg Jäckel

Abstract: In this thesis, gluon spectral functions in SU(3) gauge theory are calculated at finite temperature. The temperature range covers the confining regime below T_c to the high temperature regime, where perturbation theory is applicable. The numerical tool is the Maximum Entropy Method (MEM) employing euclidean, non-perturbative, Landau gauge gluon propagators, obtained with the Functional Renormalisation Group and Lattice QCD, as input. The spectral function is related to the propagators by an integral equation. MEM is a complex multidimensional optimisation algorithm to invert such integral equations, corresponding to an analytic continuation of the numerical data. A continuation of a discreet set of data cannot be unambiguous. The occuring ambiguities are resolved by introducing a priori knowledge of the asymptotic shape of the spectral function, in the form of a model function. Thereby, MEM simultaneously optimizes the spectral function to the input propagators and the model, leading to a unique model-dependent solution. Standard-MEM assumes positive definite spectral functions, whereas gluons show a violation of positivity in the spectral function, due to confinement. Therefore, an extended-MEM algorithm is proposed. The main application of this thesis is the calculation of the shear viscosity in units of the entropy density. A Kubo relation connects shear viscosity to the low frequency limit of a certain energy-momentum tensor correlation function. For this correlation function a loop representation of finite order in terms of gluon spectral functions is derived. That allows to calculate $\frac{\eta}{s}$ from first principles in SU(3) for the first time for arbitrary temperatures. Further, a mapping of the SU(3) results for $\frac{\eta}{s}$ to QCD is proposed.

Abstract: In dieser Arbeit werden Gluon-Spektralfunktionen bei endlicher Temperatur in der SU(3) Eichgruppe bestimmt. Der Temperaturbereich umfasst die farbgebundene Phase unterhalb der kritischen Temperatur bis in den Hochtemperaturbereich, in dem Störungstheorie anwendbar ist. Das numerische Werkzeug ist die Maximum Entropie Methode (MEM), die euklidische, nicht-störungstheoretische Gluon Propagatoren in Landau-Eichung als Input verwendet, die mit der Funktionalen Renormierungsgruppe und Gitter-Eichtheorie bestimmt wurden. Die Spektralfunktion kann über eine Integralgleichung mit den Propagatoren in Verbindung gesetzt werden. MEM ist ein komplexer mehrdimensionaler Optimierungsalgorithmus um solche Integralgleichungen zu invertieren, was einer analytischen Fortsetzung der numerischen Daten entspricht. Eine Fortsetzung von diskreten Datensätzen ist jedoch nicht eindeutig. Die auftretenden Mehrdeutigkeiten werden aufgelöst durch das Einbringen von apriori Informationen des asymptotischen Verhaltens der Spektralfunktion in Form einer Modell-Funktion. So optimiert MEM die Spektralfunktion simultan auf die Input Propagatoren und die Modell-Funktion, was zu einer eindeutigen Modell-abhängigen Lösung führt. Der Standard-MEM Algorithmus setzt positiv-definite Spektralfunktionen voraus, wohingegen Gluonen eine positivitätsverletzende Spektralfunktion besitzen, die Folge der Farbbindung ist. Daher wird ein erweiterter MEM Algorithmus ausgearbeitet. Die Hauptanwendung dieser Arbeit is die Berechnung der Scherviskosität in Einheiten der Entropiedichte. Kubo-Relationen lieferen eine Beziehung zwischen der Scherviskosität und dem Nieder-Frequenzverhalten einer bestimmten Korrelationsfunktion des Energie-Impuls Tensors . Für diese Korrelationsfunktion wird eine Loop-Dartellung mit endlicher Ordnung in Produkten von Gluon Spektralfunktionen hergeleitet. All das erlaubt die erstmalige ab initio Berechnung von $\frac{\eta}{s}$ in SU(3) für beliebige Temperaturen. Weiterhin wird eine Abbildung der SU(3) Ergebnisse für $\frac{\eta}{s}$ auf die volle QCD vorgeschlagen.

Contents

List of Figures

1 Introduction

'Eine neue wissenschaftliche Erkenntnis lässt sich gewöhnlich nicht so darstellen, dass ihre Gegner überzeugt sind. Diese sterben vielmehr aus, und die nachwachsende Generation ist von Anfang an mit der Wahrheit vertraut.'

Max Planck

1.1 General introduction

The strong interaction, the interaction that holds together nuclei and their constituents, the protons and neutrons, is one of the four fundamental interactions in nature [1]. It is described by Quantum Chromodynamics (QCD) [2], which claims the existence of six fundamental particles, the quarks, carrying electric charge $+\frac{2}{3}$ (u,c,t) or $-\frac{1}{3}$ (d,s,b). Quarks are Dirac fermions with spin $s = \frac{1}{2}$, also carrying a color charge, that can assume three values (usually called 'red', 'green' and 'blue'). In addition, for each quark there is an anti-quark with opposite quantum numbers.

The interactions between the quarks are mediated by spin $s = 1$, electrically neutral gauge bosons, called gluons. However, gluons also carry color charge, and therefore can interact with each other. That is a distinct feature of QCD compared to e.g. QED, where the photons carry no charge, and do not generate pure photon vertices.

Even though quarks carry fractional electric charge, only particles with integer multiples of the electron charge are observed freely. The reason points to another important feature of QCD, confinement [3,4]. It explains the fact, that a colorneutral bound state of particles carrying color charge, cannot be seperated into the free constituents by any finite amount of energy. That feature distinguishes the strong interaction from interactions like gravitation or electromagnetism, where a finite amount of energy suffices to seperate i.e the electron from the proton in a hydrogen atom. If one tries, however,

to seperate a meson, which is a color neutral quark anti-quark bound state, the energy stored in the binding increases until it hits the pair production threshhold, leading to the creation of a new quark-antiquark pair and instead of ending up with free quark and anti-quark, one ends up with two mesons.

QCD is a SU(3) Yang-Mills gauge theory [5] coupled to the Dirac fermions in the fundamental representation. SU(3) is asymptotically free[1], meaning that in the limit of high energy transfers (or short distances) the interaction strength tends to zero and quarks and gluon become (quasi-)'free' [7, 8]. Therefore, the hadronic phase of colorless quark bound states with 2 quarks (mesons) or 3 quarks (baryons), undergoes a phase transition as temperature is increased to a phase of free quarks and gluons, first proposed by Perry and Collins [9] and independently by Cabibbo and Parisi [10]. This phase is usually referred to as quark-gluon plasma (QGP) [11–14]. For reviews on the QGP see e.g. [15–20].
The nature of this phase transtion is not conclusively explored for arbitrary values of the baryon chemical potential μ_b. In colliders like the Large Hadron Collider (LHC) [21] and the Relativistic Heavy-Ion Collider (RHIC) [22] a cross-over between the hadronic phase and the QGP phase is observed for low μ_b [23]. By increasing μ_b one expects to find a critical point, beyond which a first order phase transition line starts, ending at the $T = 0$ axis [24].
The phase transition is two-fold. The intuitively understood confinement/deconfinement transition is accompanied by a chiral phase transition [25]. Chiral symmetry is only an approximate symmetry for finite quark masses, as mass breaks chiral symmetry on the level of the Lagrangian explicitly [26]. Both symmetries are spontaneously broken below their respective critical temperatures and are in principle distinct phase transitions with the expectation value of the Polyakov-Loop and the chiral condensate as respective order parameters. However, in QCD the critical temperatures are found to be suspiciously close to each other, so that the question of a possible deeper connection is of interest. However, this question has not yet been conclusively answered [27–30]. The topic of phase transitions is discussed in more detail in chapter 2.

For low temperatures and high baryon densities, deconfined quark matter is expected to exist in the interior of neutron stars, making the understanding of the QGP essential for describing these stellar objects [31]. Comparable energy densities were also present

[1] For asymptotic freedom to occur, Yang-Mills fields are actually required [6]

in the early universe, making the QGP dynamics also crucial for early universe models [32].

An obstacle for studying the QGP lies in its short life-time in any experimental setup that can be realized so far. Direct measurements are therefore inaccessible. In the above mentioned collider experiments, bunches of heavy-ion cores are accelerated to extremely high energies and brought to collision. Besides the energy per nucleon (which is of the order ≈ 100 GeV), the impact parameter b can be tuned. It describes the non-centrality of the collision, i.e. the relative displacement of the two particle sheets[2]. After the collision a highly non-equilibrium state is produced, that is found to thermalize rapidly ($t_{th} \approx 1$fm) and to form a QGP in its core region [33, 34].

Due to strong density gradients, the system expands rapidly and cools down in the process. Once temperature drops below the confinement/deconfinement transition temperature, hadrons are formed, that are eventually producing signals in the detectors.

Fortunately, the momentum distribution allows conclusions about the intermediate

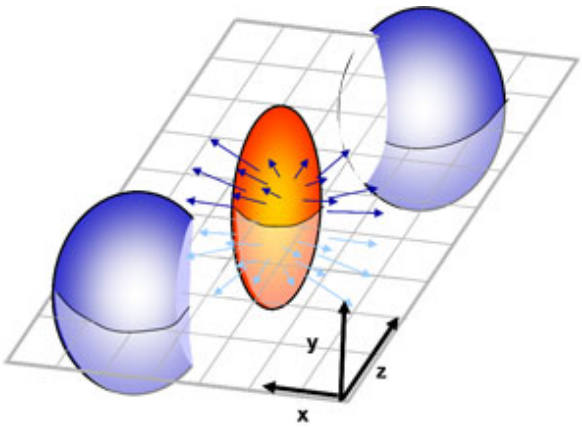

Figure 1.1: Two colliding nuclei with finite impact parameter b form a elliptic overlap region, leading to anisotropic density gradients after the collision, causing an anisotropic momentum distribution of the detected particles.

dynamics: a non-central collision, i.e a finite impact parameter b leads to an anisotropic momentum distribution of the final state particles (see. Fig. 1.1). The plane spanned by the beam direction and the direction of the impact parameter is called the plane of collision. Momentum anisotropy can be quantized by measuring the anisotropic flow coefficients ν_n [35–38]. They are defined as the expansion coefficients of the momentum distribution perpendicular to the beam direction in $\cos(n\theta)$ ($n \in \mathbb{N}$), where θ measures the angle between the direction in the plane of collsion and the out-of-plane

[2] the highly accelerated particle bunches are approximately described by sheets, due to Lorentz length contraction.

direction. The efficiency of the conversion from an initial state spatial anisotropy to a final state momentum anisotropy, i.e. the magnitude of ν_n ($n \neq 0$) is governed by the internal dynamics of the QGP phase [39]. In particular, the elliptic flow coefficient ν_2 is the main experimental observable in anisotropic flow studies in heavy-ion collisions [40].

When the theory of a deconfined phase of quarks and gluons was first recognized in the 1970s, general agreement was, to expect a gas of weakly interacting quasi-particles, that could be studied perturbatively [41, 42]. While poorly converging perturbation series indicated, that in the vicinity of the critical temperature, strong coupling effects were important, it still came as a surprise when the first results at RHIC showed [43, 44], that the effective interaction in the QGP was quite strong. In fact, the limit of strong interactions and small mean free paths - ideal hydrodynamics - was in much better agreement with the data than a weakly interacting gas [45–49]. It even turned out, that the QGP is very close to being a perfect liquid, defined be a minimal value for the shear viscosity to entropy density ratio $\frac{\eta}{s}$ [50–56].

A strong motivation to study the $\frac{\eta}{s}$-ratio further was delivered in 2004 when Kovtun, Son and Starinets claimed the existence of an universal (non-zero) lower bound $\frac{\eta}{s} \geq \frac{1}{4\pi}$. The conjecture is based on conformal arguments and is known as the AdS/CFT conjecture [57]. Besides ultra cold atomic gases, QGP was the most promising candidate to saturate the bound[3]. Experimental data indeed suggests a small $\frac{\eta}{s} \equiv (1-5)\frac{1}{4\pi}$ for the QGP [58–62].
The minimum of $\frac{\eta}{s}$ is assumed in the vicinity of the critical temperature, where the running coupling α_s is large and perturbation theory does not converge. Thus, calculations of the shear viscosity require non-perturbative methods.

In principle two classes of methods exist, continuum methods and lattice QCD. They mostly have in common to calculate euclidean correlation functions, i.e. time evolutions can only be accessed by analytic continuation of the imaginary (Euclidean) time back to real (Minkowski) time.

Lattice QCD [63] discretizes space and time and solves the equations of motion numerically on a finite lattice. This brings about some immediate advantages: The lattice spacing a implicitly introduces a cutoff, so that all quantities are finite and

[3] or to violate it, depending on each one's personal trust in string theory

renormalization can be avoided (or at least postponed). Further, it is straight forward to translate physical parameters into the lattice quantities and error handling is well defined. However, there are also some serious drawbacks. The computing effort increases dramatically with lattice size, while too small lattices suffer from finite size artifacts, that can show signals absent in a continuum approach, and vice versa. Parallelization, the use of GPU's and highly reduced hardware costs have however, extended the feasible lattice sizes in the recent decade. Related to the issue of lattice artifacts, is the extrapolation to continuum. Any quantity on the lattice will depend on the lattice spacing and in order to compare to continuum quantities needs to be extrapolated to $a \to 0$. The need for regularisation and renormalisation comes through the backdoor, as the continuum limit will give the (possibly divergent) bare quantities. Lattice QCD is further restricted to small baryon densities, due to the yet unsolved sign problem [64]. It describes the numerical problem of integrating highly oscillatory integrands to a predictive accuracy and occurs e.g. for a finite background density of interacting fermions.

Examples for continuum methods are the Dyson-Schwinger equations (DSE's) and the Functional Renormalization Group (FRG) solving the full theory or effective models as the Nambu Jona-Lasinio (NJL) model [65–68] or the quark-meson model [69–71]. DSE's are the quantum field theory equivalent to the Euler-Lagrange equations of classical mechanics, and are thus the equations of motion for the correlation functions. They are given by an infinite hierarchy of coupled differential equations that can be solved approximately by introducing a suitable truncation [72].

FRG on the other hand solves the (exact) Wetterich flow equation [73] for the effective action. The flow equation interpolates between the classical action and the full quantum action by successively integrating out momentum shells and rescaling the system, which is an RG-transformation interpreted as a flow. In general, the flow equation cannot be solved exactly and, similar to the DSE's, truncations are necessary [74].

Once the euclidean correlation functions are computed by the method of choice, the aim of this thesis is to connect them to transport coefficients, especially shear viscosity. The relation is established by the Kubo relation [75], that yields - within linear response theory - shear viscosity in terms of the zero frequency limit of the frequency derivative of the spectral function $\rho_{\pi\pi}$ of a certain energy-momentum tensor correlation function.

It will be shown, that $\rho_{\pi\pi}$ can be expressed in terms of products of spectral functions of the fundamental fields in a diagrammatic expansion with a finite number of diagrams. The spectral functions of the fundamental fields are obtained from the (FRG and lattice) euclidean correlation functions by analytic continuation.
Here, methods like the Tikhonov regularisation [76], Pade approximation or the Maximum Entropy Method (MEM) are feasible tools. In this thesis the latter is employed, being a numerical method to determine the most likely analytic continuation given the correlator and any available prior knowledge on the shape of the spectral function. Originally, MEM was designed for image reconstruction [77,78], but is today also widely used in High Energy Physics for analytic continuations of numerical data [79–82].
For gluon spectral functions, confinement imposes a complication, as it is reflected in a positivity violation of the spectral function. As, in general, particle spectral functions are positive definite, MEM was designed, to a priori assume a positive definite spectral function. Here, an extension of standard-MEM is proposed, to allow the reconstruction of spectral functions with (finite) violation of positivity.

1.2 Outline of the thesis

The thesis is structured as follows: In the following chapters 2-5 the needed theoretical background is established. First, in chapter 2 a basic introduction to the quantum field theory under consideration is given. Important features of quantum chromodynamics like asymptotic freedom as a consequence of the non-abelian gauge group, the phase diagram and the topic of conformal field theory are discussed. In particular, pure (quarkless) SU(3) gauge theory is introduced, with special emphasis on the differences to QCD.

Chapter 3 will introduce hydrodynamics. The theory is used to study the dynamics of the quark-gluon plasma, which can be treated as an almost perfect liquid. Here, the AdS/CFT conjecture of a lower bound for the viscosity over entropy ratio is introduced. Further, Kubo formulae are derived within linear response theory. They relate the viscosity to static correlation functions of the energy-momentum tensor, and thus build a bridge between hydrodynamics and field theory.

Chapter 4 discusses thermal field theory i.e. field theory at finite temperature. There

are two conceptually different approaches. The 'imaginary time formalism' trades the time variable for temperature. It can thus only describe systems in thermal equilibrium. It is straightforward to apply, and does not create much calculational trouble. The second approach, the 'real-time formalism', treats temperature as an additional variable. This allows to calculate non-equlibrium quantities. The inclusion of a thermal bath, can be obtained by a doubling of the degrees of freedom for the field variables and the sources. A generic loop intergral is evaluated in both formalisms to demonstrate their equivalence.

In chapter 5, correlation functions are discussed, with special interest in the spectral function, which will be the key object of this thesis. It will be shown, that in Minkowski spacetime, the spectral function is related to the imaginary part of the retarded Greens function, while after Wick rotation to Euclidean space, the spectral function is related via an integral equation to the euclidean (imaginary time) correlation function. This relation will be the starting point for the Maximum Entropy Method discussed in chapter 7.

In chapter 6 the knowledge assembled in chapters 2-5 is combined to derive a diagrammatic expansion for the shear viscosity in terms of the spectral functions of the fundamental fields and (Bose) distribution functions. The leading order and next-to-leading order diagrams are classified and discussed in detail.

In chapter 7, the numerical method MEM will be discussed extensively. After the introduction of the general algorithm, modifications are pointed-out to deal with gluon spectral functions, which violate positivity as a consequence of confinement. Also a proof for the uniqueness of the MEM solution is given, using Bayes' theorem of conditional probabilities.

Finally, in chapter 8, the results of the extended-MEM simulations for finite temperature Yang-Mills theory are presented. In the first part of the chapter, sources for systematic errors are analysed and quantified. In the second part, the features of the gluon spectral functions are dicussed and compared to previous results. Both the limit of zero temperature and high temperature are studied.

Chapter 9 presents the main application of gluon spectral functions in this thesis,

The shear viscosity over entropy density ratio $\frac{\eta}{s}$ is calculated, studied in the vicinity of the critical temperature and extrapolated to the perturbative hard thermal loop (HTL) results. To the author's knowledge, $\frac{\eta}{s}$ is calculated for such a wide temperature range from first principles for the first time.

The thesis is summarized in chapter 10 and an outlook to further interesting applications of spectral functions and the MEM algorithm is given.

2 Quantum Chromodynamics and Yang-Mills theory

'Die Gefahr, dass der Computer so wird wie der Mensch, is nicht so gross, wie dass der Mensch so wird wie der Computer.'
Konrad Zuse

In this chapter, QCD is introduced, beyond the qualitative introduction given in the preceeding chapter, with special emphasis on the gauge sector.

2.1 SU(N) gauge group

In this section the gauge group of Yang-Mills theory is introduced. The aim is to derive gauge invariant tensors, that can be used to build the most simple Lagrangian, which will be the Yang-Mills Lagrangian.
The special unitary group SU(N) is the Lie group of $N \times N$ unitary matrices with determinant 1. It is a continous, simple connected group, such that that any infinitesimal group element[1] $g(\epsilon)$ can be written in terms of Hermitian operators T^a - the generators - as

$$g(\epsilon) = 1 + i\,\epsilon^a T^a + O(\epsilon^2) \tag{2.1}$$

The generators span the space of infinitesimal group transformations, such that a basis can be found. In particular, for such a basis $\{T^a\}$ the commutator of each pair of generators can be written as:

$$[T^a, T^b] = i\,f^{abc}T^c \tag{2.2}$$

The numbers f^{abc} are characteristic for the group and are called structure constants. The space of generators together with the operation (2.2) forms a Lie algebra usually

[1] infinitesimal with respect to deviations from the neutral element, which is the unity matrix

denoted by $\mathfrak{su}(N)$. Apart from the commutation relation (2.2) the generators have not yet been further specified. In particular, their dimenionality is not fixed by the group. The 'fundamental representation' is a N-dimensional representation given by a basis of the matrix group SU(N). An example is SU(2), for which the most commonly used fundamental representation is given by the Pauli matrices

$$\sigma_1 = \begin{pmatrix} 0 & 1 \\ 1 & 0 \end{pmatrix} \quad (2.3) \qquad \sigma_2 = \begin{pmatrix} 0 & -i \\ i & 0 \end{pmatrix} \quad (2.4) \qquad \sigma_3 = \begin{pmatrix} 1 & 0 \\ 0 & -1 \end{pmatrix} \quad (2.5)$$

Another important representation is the (N^2-1)-dimensional 'adjoint representation' given by

$$(T_A^a)^{bc} = -i\, f^{abc} \tag{2.6}$$

Let us now consider a local gauge transformation of a $N-$component Dirac field Ψ of the form

$$\Psi(x) \to V(x)\Psi(x) \tag{2.7}$$

with

$$V(x) = e^{i\,\alpha^a(x)T^a} \tag{2.8}$$

Obviously, this is an example for a local SU(N) transformation, which shall leave the Lagrangian invariant. As the local gauge transformation changes the phase of fields at different positions independently, taking derivatives naively is no longer well defined:

$$n^\mu \partial_\mu \Psi = \lim_{\epsilon \to 0} \frac{1}{\epsilon}(\psi(x+\epsilon n) - \psi(x)) \tag{2.9}$$

The problem is solved by introducing the covariant derivative

$$n^\mu D_\mu \Psi = \lim_{\epsilon \to 0} \frac{1}{\epsilon}(\psi(x+\epsilon n) - U(x+\epsilon x, x)\psi(x)) \tag{2.10}$$

in terms of the comparator $U(y,x)$. The comparator is defined via its transformation law under the local gauge transformation $V(x)$

$$U(y,x) \to\ V(y)U(y,x)V^\dagger(x) \tag{2.11}$$

and the normalisation $U(x,x) = 1$. It ensures that only objects with the same transformation properties are substracted. $U(y,x)$ can be chosen to be unitary and thus can

be expressed in terms of the SU(N) generators for an infinitesimal seperation:

$$U(x+\epsilon x, x) = 1 + i\, g\epsilon n^\nu A^a_\mu T^a + O(\epsilon^2) \tag{2.12}$$

Here, a new field A^a_μ is introduced, called gauge field. From this point of view gauge fields simply follow from the requirement of parallel transport for fields after local gauge transformations. The covariant derivative reads in terms of the gauge fields

$$D_\mu = \partial_\mu - i\, g A^a_\mu T^a \tag{2.13}$$

By construction, covariant derivatives of the Dirac fields transform under (2.7) according to

$$D_\mu \Psi \to (1 + i\,\alpha^a T^a) D_\mu \Psi + O(\alpha^2) \tag{2.14}$$

One more object is needed to build the Yang-Mills Lagrangian, the field strength tensor $F^a_{\mu\nu}$. It is defined as

$$F^a_{\mu\nu} T^a \equiv \tfrac{i}{g}[D_\mu, D_\nu] \tag{2.15}$$

or, expanding the covariant derivatives according to (2.13)

$$F^a_{\mu\nu} = \partial_\mu A^a_\nu - \partial_\nu A^a_\mu + g f^{abc} A^b_\mu A^c_\nu \tag{2.16}$$

Note, that the last term is only present in non-Abelian gauge theories and permits pure gauge field vertices. The transformation law for the field strength tensor is

$$F^a_{\mu\nu} T^a \to V(x) F^a_{\mu\nu} T^a V^\dagger(x) \tag{2.17}$$

2.2 The Yang-Mills Lagrangian

Now, the Yang-Mills Lagrangian can be constructed. The scalar

$$\mathcal{L}_g = -\frac{1}{4} F^a_{\mu\nu} F^{\mu\nu}_a \tag{2.18}$$

is gauge invariant, which can simply be checked by performing a local gauge transformation (2.7). It constitutes the kinetic energy term for the gauge fields A^a_μ. Note, however, that (2.18) describes a full interacting (gauge) field theory, due to the non-Abelian nature of $F^a_{\mu\nu}$ in (2.16). This non-trivial gauge sector strongly distiguishes SU(N) from abelian gauge theories like QED. Equation (2.18) is called Yang-Mills La-

grangian (without quarks).
The coupling to Dirac fermions is achieved by adding the Dirac Lagrangian

$$\mathcal{L}_{Dirac} = \sum \bar{\psi}(i(\gamma^\mu \partial_\mu) - m)\psi \tag{2.19}$$

with the partial derivative ∂_μ promoted to the covariant derivative D_μ:

$$\mathcal{L}_{YM} = \mathcal{L}_g + \sum \bar{\psi}_f(i(\not{D}_\mu) - m_f)\psi_f \tag{2.20}$$

Here, the quark fields ψ_f acquire an additional index for their flavor. The number of flavour is denoted by n_f. In particular, Quantum Chomodynamics is the current best effective theory for the strong interaction with $N = 3$, $n_f = 6$ and experimentally determined masses for the quarks. Note, that the coupling between quarks and gauge fields is generated by the gauge field dependence of the covariant derivative.
The phase diagram of QCD is very rich. In addition, interesting phenomena can occur, when the number of colors, the number of flavours or the quark masses are varied. In this thesis it is only possible to concentrate on the aspects of the phase diagram, that will be of importance for the remainder of the thesis.

2.3 Aspects of the Yang-Mills Lagrangian

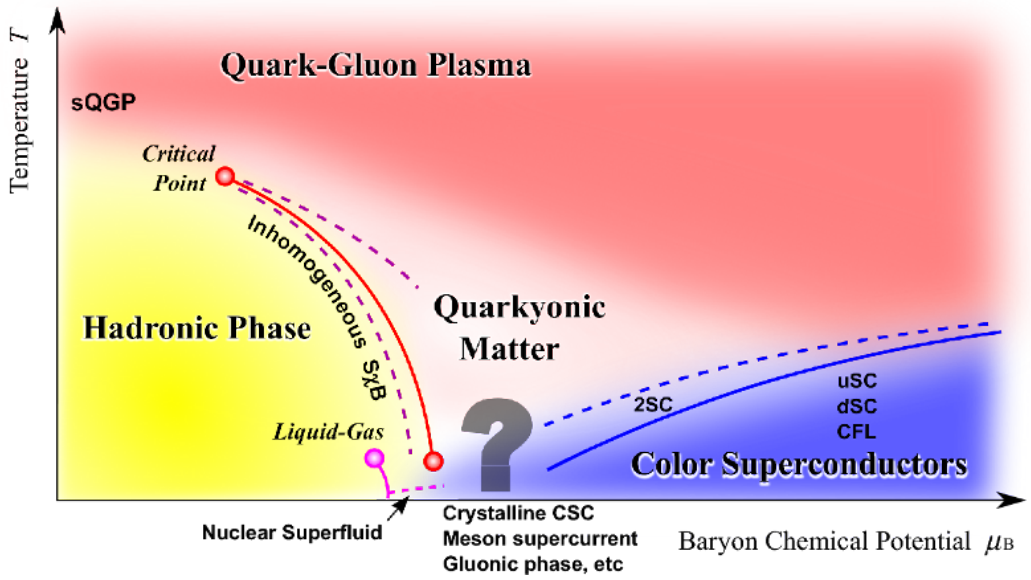

Figure 2.1: Qualitative sketch of the QCD phase diagram.

Figure 2.1 shows a sketch of the current understanding of the QCD-phase diagram,

as a function of temperature and baryon chemical potential. In the first chapter, a rough qualitative overview has already been given, with special emphasis on the historic developement of the understanding of the strong interaction. Here, the topic of symmetries and spontaneous symmetry breaking are discussed from a modern point of view. Current methods of studying the QCD/Yang-Mills phases are discussed.

2.3.1 Phase transitions

A phase transition is the transformation of a system from a state of matter (phase) to another. Common examples are the different phases of water: ice, liquid water and vapor, or the phase transition in the ferromagnetic Ising model, from a ordered phase, where all spins are aligned to a disordered phase signaled by a vanishing total magnetisation. The two examples already cover many aspects of phase transitions. The magnetisation in the Ising model is an example for an order parameter, that is associated with any phase transition. This reflects, that a phase transition occurs, when a symmetry of a system is spontaneously broken. A spontaneous symmetry breaking describes the effect, that a system's Lagrangian respects a certain symmetry but the ground state does not. A simple example is again the square lattice Ising model with zero external magnetic field $h = 0$ and a ferromagnetic coupling $J > 0$ in the nearest neighbour approximation. Its Hamiltonian reads

$$H(\vec{\sigma}) = -J \sum_{<ij>} \sigma_i \sigma_j \tag{2.21}$$

and is symmetric under the flipping of all spins $\sigma_i \to -\sigma_i$. However, below the Curie temperature, the spins will align and spontaneously break the spin-flip symmetry. Thus, in the symmetry broken phase, an additional parameter is needed to fully describe the system, which is the value of the total magnetisation.
Phase transitions are divided in two classes: First order phase transitions, i.e phase transitions associated with latent heat and second order (or continuous) phase transitions, where the order parameter changes continuously across the transition.

In Yang-Mills theories, there are two symmetries associated with the transition between the hadronic phase and the QGP phase: Chiral symmetry and center symmetry. The Yang-Mills Lagrangian would be chiral symmetric, if the matter part allows a

decompostion into

$$\bar{\psi}(\not{D} - m)\psi = \bar{\psi}_L(\not{D} - m)\psi_L + \bar{\psi}_L(\not{D} - m)\psi_L \tag{2.22}$$

with $\psi_L = \frac{1-\gamma_5}{2}\psi$ and $\psi_R = \frac{1+\gamma_5}{2}\psi$. This decomposition is, however, only possible for, $m \equiv 0$, i.e. finite quark masses break chiral symmetry explictly. In the case of vanishing quark masses, left- and right-handed fields can be rotated separately in flavor space, representing a $U_L(n_f) \times U_R(n_f)$ symmetry. The order parameter of chiral symmetry is the chiral condensate $\langle \bar{q}q \rangle$. For physical quark masses, chiral symmetry can at least be considered an approximate symmetry for the lightest ($u-/d$-)quarks.
Center symmetry is related to gauge transformations, that are periodic in the temporal direction modulo a twist belonging to the center of SU(3)[2]. In pure SU(N) gauge theory, center symmetry is an exact symmetry of the action, however dynamical quarks break center symmetry explictly. The order parameter of center symmetry is the expectation value of the Polyakov loop

$$\langle P(x) \rangle \equiv \mathrm{Tr} \left\{ \mathrm{T} \exp \left[i \int_0^\beta A_0(\vec{x}, \tau) d\tau \right] \right\} \tag{2.23}$$

The center symmetric phase is the (confining) hadronic phase, while the center broken phase is related to the deconfined phase[3].

2.3.2 Phase transitions in Yang-Mills theory

The nature of the phase transitions in QCD is still under discussion. The reason for the difficulty to explore the phase diagram is rooted in the behaviour of the running coupling α_s. In the vicinity of the phase transitions it is large and causes a breakdown of perturbation series. The complexity of phenomena occuring in the vicinity of the chiral phase transition and the confinement/deconfinement phase transition has lead to a variety of effective theories, that, in principle, pursue the goal to neglect certain effects of the full Yang-Mills or QCD Lagrangian to make one of the symmetries exact in the symmetric phase.

[2]The centre Z of a group G is the set of elements $g^* \in G$, such that $g^*g = gg^*$ for all $g^* \in G$. The center of SU(N) are the N-th roots of unity $Z_N = \{zI_{N\times N} | z^N = 1\}$.
[3]Again, this is exact for pure gauge theory only.

The simplest approach is to drop the fermionic part of the Yang-Mills Lagrangian entirely. The critical temperature was determined to [83]

$$T_c^{\mathrm{SU}(3)} \approx 270 \pm 10\mathrm{MeV} \tag{2.24}$$

by lattice QCD studies. The phase transition is first order [84]. Interestingly, in pure SU(N) gauge theory the order of the phase transition depends on the dimensionality of the gauge group. For SU(2) the phase transition is second order while the discontinuity of the Polyakov loop expectation value, signaling a first order transition becomes stronger with increasing N [85].

This limit is not to be mixed with the limit of infinite quark masses, where center symmetry is excact, but chiral symmetry has no meaning. The reason for the restoration of center symmetry is this limit is the absense of dynamical quarks. Thus the free energy cost necessary to create a non-zero center charge (for example a test quark) is infinite, as the color flux string cannot be broken by a static quark [86].

For physical quark masses, only the lightest quarks, 'up', 'down', 'strange' are dynamical at energies of the order of the confinement/deconfinement transition temperature , as the other quarks are too heavy to have a quantitative effect on the phase transition. However, center symmetry is no longer exact and the transition broadens to a crossover [87]. The QCD transition temperature has been calculated to [88–91]

$$T_c^{QCD} \approx 150 - 180\mathrm{MeV} \tag{2.25}$$

For finite baryon chemical potential available non-perturbative methods are sparse, as lattice QCD suffers from the sign problem. Studies are mainly reduced to effective models, as the Polyakov-quark-meson model [92,93] or the Polyakov-NJL-model [94,95]. Such studies suggest, that the crossover ends at a second order critical point. The position of the critical point depends strongly on the model and masses of quarks and mesons [96–98]. From the critical point, towards larger chemical potentials, a first order transition line starts. However, there is also debate on whether the critical point is tricritical, and chiral and confinement/deconfinement transition split [99–101].

The last class of studies of Yang-Mills theories are the large N results. The idea is that the $N \to \infty$ theory, unlike the naive expectation is for many cases is easier to solve, as

Feynman amplitudes, that scale with inverse powers of N are suppressed. In two spatial dimensions the meson spectrum could (semi-)analytically be computed [102]. Even though the 4-d equivalent cannot be solved analytically, the large N limit is widely used. The main idea is to expand the original theory in powers of $\frac{1}{\mathrm{N}}$ [103]. Interestingly, the large N limit can be identified with a free string theory. Thus, the large N expansion connects field theory with string theory [104]. The most well-known finding is the AdS/CFT conjecture, that will be discussed in the next chapter.

2.4 The running coupling and asymptotic freedom

One of the most prominent features of QCD is the phenomenon of asymptotic freedom. It can be understood by calculating the β-function, which describes the change of the (renormalized) coupling constant under the change of the energy scale μ.

$$\beta(\alpha_s) = \mu^2 \frac{\partial \alpha_s}{\partial \mu^2} \tag{2.26}$$

In perturbation theory the β-function is expanded in powers of the coupling:

$$\beta(\alpha_s) = -\alpha_s^2(\beta_0 + \beta_2 \alpha_s + ...) \tag{2.27}$$

The respective terms $\beta_0, \beta_1, ...$ are the 1-loop,2-loop,... contributions. The 1-loop result for the running coupling is obtained by only keeping the first term in (2.27) and integrating (2.26):

$$\alpha_s(\mu^2) = \frac{\alpha_s(\mu_0^2)}{1 + \beta_0 \alpha_s(\mu_0^2)\,\mathrm{Log}(\frac{\mu^2}{\mu_0^2})} \tag{2.28}$$

This fixes the functional form of α_s except its value $\alpha_s(\mu_0^2)$ at a scale μ_0^2. Setting

$$\Lambda = \mu_0^2 \exp\left[-\frac{1}{\beta_0}\frac{1}{\alpha_s(\mu_0^2)}\right] \tag{2.29}$$

(2.28) can be expressed in terms of the dimensionful parameter Λ:

$$\alpha_s(\mu^2) = \frac{1}{\beta_0\,\mathrm{Log}(\frac{\mu^2}{\Lambda^2})} \tag{2.30}$$

The value of the expansion coefficient β_0 can be obtained in several ways. The renormalisation Z_α for α_s can be calculated from the quark-gluon vertex, the ghost-gluon vertex, or pure gluon vertices. For a SU(N) gauge group and n_f fermion flavour the

leading order coefficient is [105, 106]:

$$\beta_0 = \frac{1}{4\pi}\left(\frac{11\,N}{3} - \frac{2}{3}n_f\right) \tag{2.31}$$

Also higher-loop expressions for the β-function analytically known. The next coefficients are

$$\beta_1 = \frac{1}{(4\pi)^2}\left(\frac{105\,N}{3} - \frac{38}{3}n_f\right) \tag{2.32}$$

and

$$\beta_2 = \frac{1}{(4\pi)^3}\left(2857\,N6 - \frac{5033}{18}n_f + \frac{325}{52}n_f^2\right) \tag{2.33}$$

Conventionally, for the reference scale μ_0^2, the mass of the Z_0 boson is chosen ($M_Z = 91.2\text{GeV}$) and the current QCD value for the coupling is $\alpha_s(M_Z) = 0.1184 \pm 0.0007$ [107].

In Fig.2.2 the QCD running coupling is shown in the perturbative regime. Towards smaller energies, the coupling increases, until a perturbative treatment breaks down. The plot is taken from [107] and constitutes the average over all relevant results for the running coupling from 2009.

In pure gauge theory there is no experimental data to to fix the absolute scale of the running coupling. This will be further discussed, when the non-perturbative results for $\frac{\eta}{s}$ is extrapolated to the Hard-Thermal-Loop regime.

The sign of the β-function is of particular interest. If it is negative the coupling strength decreases with increasing energy scale. This is the case for QCD, as can be seen in Fig. 2.2. The phenomenon of asymptotic freedom, is a unique property of non-Abelian gauge sectors. It leads to converging perturbation series (2.27) at large energy scales. Interestingly, the feature of asymptotic freedom depends on the ratio $\lambda = \frac{n_f}{N}$. For $\lambda \geq \frac{11}{2}$ the corresponding field theory is no longer asymptotically free.

At finite temperature far less is known about the running coupling, as $\alpha_s(Q, T)$ will also be dependent on temperature. In the limit $Q >> T$, temperature will be not be a relevant scale and

$$\alpha_s(Q >> T, T) \approx \alpha_s(Q) \tag{2.34}$$

apart from this obvious limit, there are only few results for the finite temperature running coupling. [108–111]. In this thesis for the two-loop diagrams in the viscosity expansion, the running coupling is determined via the ghost-gluon vertex, employing

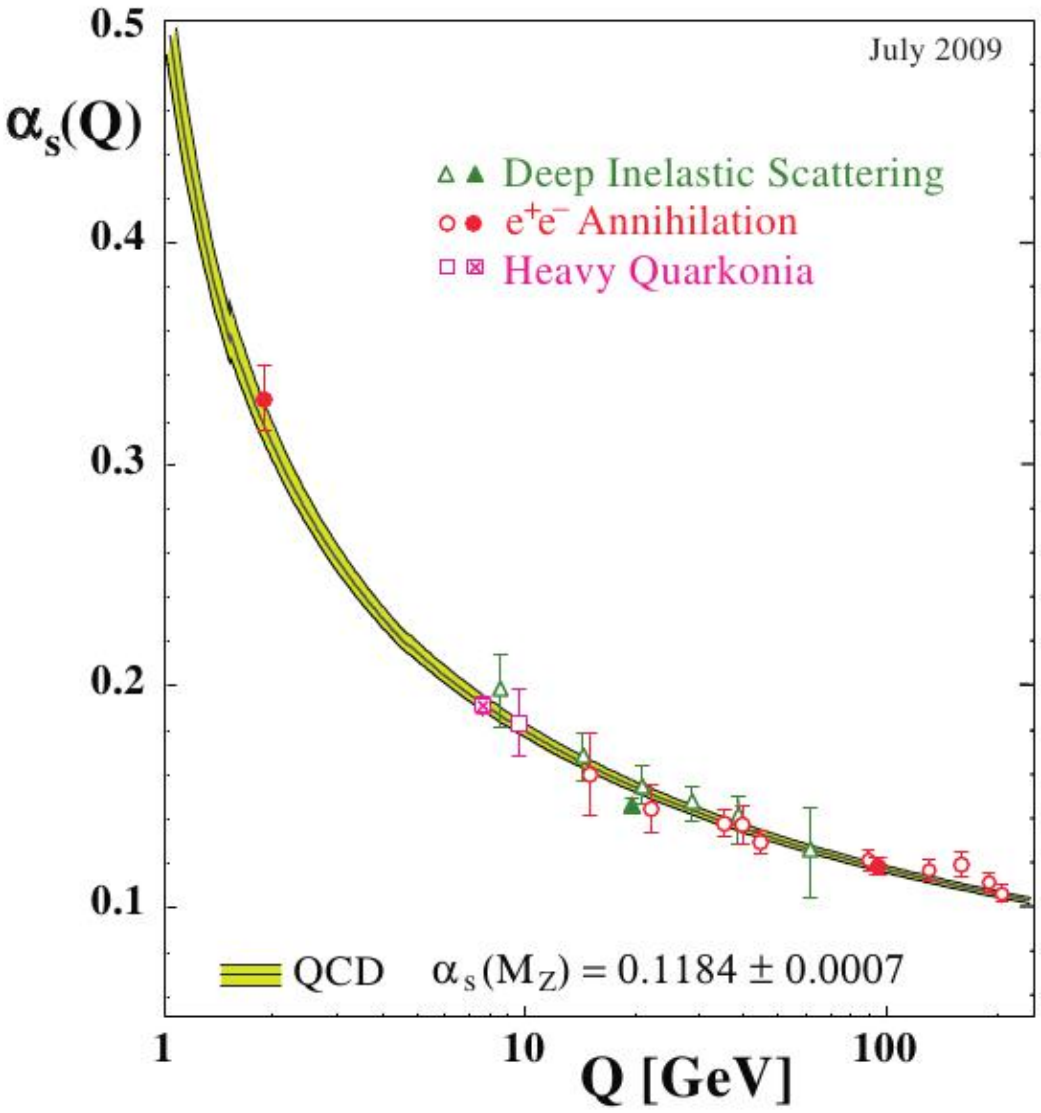

Figure 2.2: World average for the perturbative QCD running coupling.

the same source as for the propagators. For the extrapolation to the perturbative regime the zero temperature α_s in two-loop approximation is employed.

2.5 Deconfined QCD matter

In this concluding section, examples for observable deconfined QCD matter are discussed.

From the previous section, it is obvious, that the best known part of the QCD phase diagram is the high temperature and/or high baryon chemical potential region, as it allows a perturbative description. In particular, two limits are of interest.

In the radiation dominated early universe, free quarks and gluons, leptons and photons made up the particle content. During its expansion the universe cooled and reached the confinement/deconfinement transition temperature at $t \approx 10^{-6}$s. To study the QCD phase transition, one needs observables in the today universe, that were affected by the dynamics at temperatures of the order of the QCD critical temperature. For example, the anisotropies of the cosmic mircrowave background (CMB) yields direct information about the inflationary phase. The reason is, that during inflation the relevant wavelengths became causally disconnected from microphysics, but re-entered the Hubble radius after inflation but prior to photon decoupling. The remnants of the QCD phase transition however occured after inflation. Therefore, they never got disconnected from equiblibrating effects and were washed out. Note, that the timescale of the cosmic QCD phase transition is expected to be of the order $t_{QCD} \approx 10^{-5}$s, whereas the typical timescale for the strong interaction is $t_s \approx 10^{-23}$s. Possible remnants of the QCD phase transition can thus not be of radiative nature.
Indirect information about the QCD phase transition might be found in the baryon asymmetry [112, 113] or in primordial magnetic fields [114, 115].

The second, opposite limit is the limit of high baryon densities and comparably small temperatures. Such conditions are found in the interior of neutron stars. The deconfined QCD matter is in this context usually called 'quark matter'. Neutron stars can (to some extend) be understood perturbatively with aid of the Pauli exclusion principle, which will lead to the formation of a degenerate Fermi sea. If some kind of attractive interaction is present, the quarks near the Fermi surface will condensate into Cooper pairs inducing color Meissner effects, leading to color superconductivity. There are many reviews found on this and related topics of the color-flavor-locked phase, mixed phases and effective theories, which cannot be covered here [24, 116, 117]

The most well-known realisation of deconfined QCD matter is experimentally realized the collider experiments at CERN and RHIC. As discussed qualitatively in the introductory chapter of this thesis, heavy-ion cores are brought to collision at high energies, such that a highly non-equilibrated, dense plasma is created. A typical heavy-ion collision is depicted in Fig.2.3. Spatial anisotropies due to a non-central collision, cause an elliptic overlap region of the nucleons, participating in the collision. This leads to anisotropic density gradients, which cause the expansion of the produced plasma to be anisotropic as well. When the system is cooled down, such that it decouples, the final

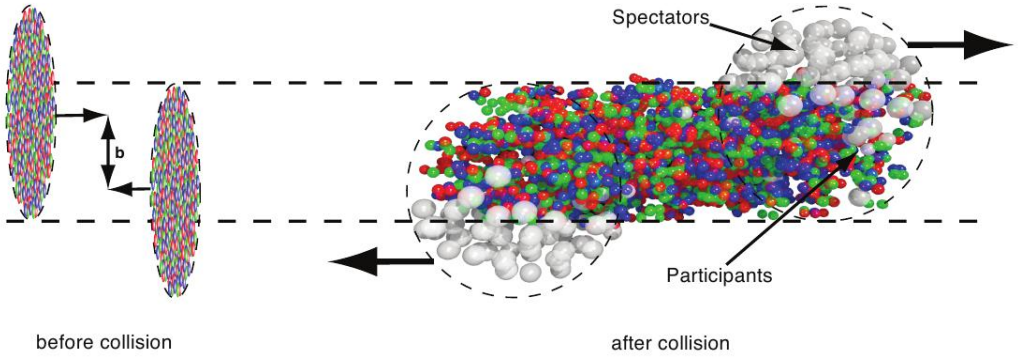

Figure 2.3: Sketch of a non-central heavy-ion collision. The initial state spatial anisotropy causes a momentum anisotropy of the final state (see also Fig.1.1).

state particles are detected, and the momentum anisotropy can be calculated. The anisotropy is quantified, by measrung the anisotropic flow coefficients ν_n, defined as the expansion coefficients in

$$E\frac{d^3N}{d^3p} = \frac{1}{2\pi}\frac{d^2N}{p_t dp_t dy}\left(1 + 2\sum_{n=0}^{\infty}\nu_n \cos\left[n(\phi - \Psi_R)\right]\right) \tag{2.35}$$

with the particle energy E, momentum p, transverse momentum p_t and rapidity y. ϕ denotes the azimuthal angle and Ψ_R the reaction plane angle. The flow coefficients are obtained by projection, and yield:

$$\nu_n(p_t, y) = \langle \cos\left[n(\phi - \Psi_R)\right]\rangle \tag{2.36}$$

The first coefficent ν_1 is called directed flow and vanishes at midrapidity for the collision of identical nuclei[4], while the second coefficient ν_2 is the elliptic flow. It is sensitive on the early stage dynamics, and therefore constitutes a good probe for the quark-gluon plasma. In particular, the dynamics of the quark gluon plasma is strongly influenced by the ratio $\frac{\eta}{s}$. In Fig.2.4 the dependence of the reaction plane eccentricity ϵ, which is proportional to the elliptic flow coefficient ν_2, on $\frac{\eta}{s}$ as a function of after-collision time. The qualitative effect is, that a higher $\frac{\eta}{s}$-ratio dampens the momentum anisotropy. This is expected, as shear viscosity is a dissipative effect, that generally tends to smear out signals.

The measurement of the elliptic flow has become an active field of research in the preceeding decade, with the general agreement, that quark-gluon plasma is close to being a perfect liquid [118–120]. With increasing accuracy, also higher anisotrpic flow

[4]Indeed, all odd coefficients vanish at midrapidity

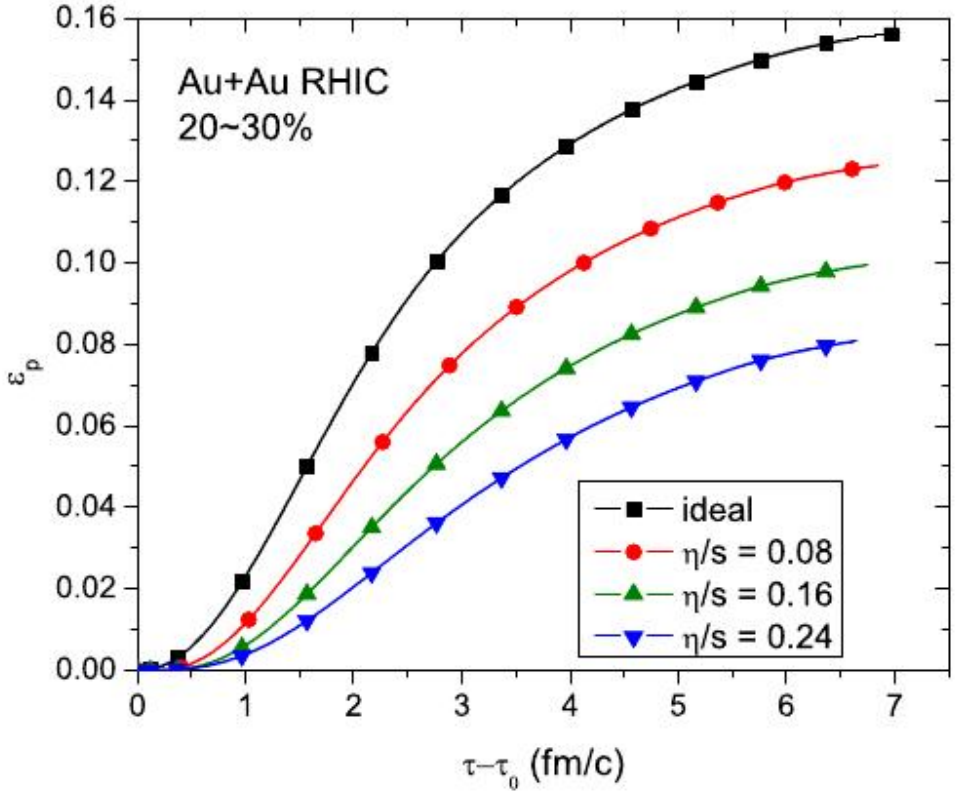

Figure 2.4: Effect of $\frac{\eta}{s}$ on the eccentricity ϵ for Au/Au collisions modeled within the MCGlauber model.

coefficients are measured [121, 122].

For the modelling of heavy-ion collisions the structure of the beams is an important issue. The nucleons are highly located, such that a naive uniform distribution cannot cover the real structure. As the elliptic flow is dependent on anisotropy effects in the early dynamics, such pre-collision configurations will effect ν_2 - even the averaged result. Information on the effect of the nucleonic structure is obtained from event-by-event analysis [123–125].

3 Hydrodynamics

'It is impossible to convey the beauty of the laws of nature
to someone, who is not familiar with the principles of mathematics.
I regret it, but it seems true.'
Richard Feynman

In the first chapter, it was already mentioned that hydrodynamics is well-suited to describe the dynamics of the quark-gluon-plasma stage in heavy-ion collisions [126,127]. Therefore, in this chapter an introduction is given to the main concepts of this theory, following to some extend the review article [128] and references therein. Further, linear response theory is introduced and the Kubo formulae are derived. They form the basis of connecting experimental data of anisotropic flow coefficients to the theoretical models for the shear viscosity over entropy density ratio $\frac{\eta}{s}$. The issue of perfect fluidity is adressed and the well-known AdS/CFT conjecture for a universal lower bound for $\frac{\eta}{s}$ is motivated.

3.1 Non-relativistic hydrodynamics

Hydrodynamics is based on the observation, that in fluids the behaviour of correlation functions at small energy and momentum is dominated by the evolution of conserved charges. "Conserved" indicate, that these charges cannot disappear locally, but will propagate large distances compared to the mean free path of the fluid. For a classical non-relativistic fluid the conserved quantities are energy, mass and momentum. These quantities obey conservation laws:

$$\frac{\partial \epsilon}{\partial t} + \vec{\nabla} \cdot \vec{j} = 0 \tag{3.1}$$

$$\frac{\partial \rho}{\partial t} + \vec{\nabla} \cdot \vec{g} = 0 \tag{3.2}$$

$$\frac{\partial g_i}{\partial t} + \nabla_j \Pi_{ij} = 0 \tag{3.3}$$

The conservation laws are easily understood: Equation (3.1) for example states, that a change in the energy density ϵ at some position $\vec{x}$ can only occur if the net energy flow $\vec{\nabla} \cdot \vec{j}(\vec{x})$ to and from this position does not vanish. In integral form

$$\frac{\partial}{\partial t} \int_V d^3x\, \epsilon(x) = - \int_{\partial V} \vec{j} \cdot d\vec{a} \tag{3.4}$$

this interpretation is even more intuitive: The energy of some volume V changes due to energy flow through the boundary ∂V. Note, that the differential area element $d\vec{a}$ always points outwards, explaining the minus sign.
Equation (3.1) is retrieved by applying Gauss' theorem to (3.4) and assuming the validity for all volumes:

$$\begin{aligned} 0 &= \frac{\partial}{\partial t} \int_V d^3x\, \epsilon(x) + \int_{\partial V} \vec{j} \cdot d\vec{a} && (3.5)\\ &= \frac{\partial}{\partial t} \int_V d^3x\, \epsilon(x) + \int_V d^3x\, \vec{\nabla} \cdot \vec{j(x)} && (3.6)\\ &= \int_V d^3x\, (\tfrac{\partial \epsilon(x)}{\partial t} + \vec{\nabla} \cdot \vec{j(x)}) && (3.7)\\ & && (3.8) \end{aligned}$$

Analog interpretations hold for (3.2) and (3.3). In general, equations (3.1) − (3.3) cannot be solved analytically and approximations are needed. A common approach is to solve them order by order in derivatives of the fluid velocity $\vec{v}$ and the thermodynamic variables pressure P, energy density ϵ and mass density ρ. The conservation laws are not sufficient to unambiguously determine the six unknown quantities, energy density, mass density, pressure and fluid velocity. However, there is a sixth equation, the equation of motion (EoM), to close the system.

The leading order result in the velocity gradient expansion is called ideal hydrody-

namics and yields

$$\vec{j} = \vec{v}(\epsilon + P) \tag{3.9}$$

$$\vec{g} = \rho\vec{v} \tag{3.10}$$

$$\Pi_{ij} = P\delta_{ij} + \rho v_i v_j \tag{3.11}$$

Ideal hydrodynamics is characterized by the absence of dissipative forces, i.e. irreversible processes in the fluid[1]. Dissipative processes can, however, occur at the next order in the derivative expansion. The next-to-leading order is called viscous hydrodynamics and is governed by new parameters: the transport coefficients η (shear viscosity), ζ (bulk viscosity) and κ (thermal conductivity):

$$\vec{j}_i = v_i(P + \epsilon) + v_j\delta\Pi_{ij} + Y_i \tag{3.12}$$

$$\vec{g} = \rho\vec{v} \tag{3.13}$$

$$\Pi_{ij} = P\delta_{ij} + \rho v_i v_j + \delta\Pi_{ij} \tag{3.14}$$

with $Y_i = -\kappa\vec{\nabla}T$ and $\delta\Pi_{ij} = -\eta(\nabla_i v_j - \nabla_j v_i - \frac{2}{3}\delta_{ij}\vec{\nabla}\cdot\vec{v}) - \zeta\delta_{ij}\vec{\nabla}\cdot\vec{v}$
Transport coefficients are proportional to the gradients of the fluid velocities, such that they induce forces to dampen the gradients. In that sense, they are the fluid analog to frictional forces. This was already discussed in the preceeding chapter in the context of the interpretation of Fig.2.4. Bulk viscosity is proportional to the velocity gradients along the flow direction of the fluid, i.e. it contains information on the non-ideal behaviour of the fluid under compression. In particular, bulk viscosity vanishes for incompressible fluids. Shear viscosity on the other hand contains information on velocity gradients transverse to the flow direction of the fluid. Figure 3.1 shows the intuitive definition of shear viscosity: A resting fluid is put between two plates. If one of the plates is now set into constant motion, a velocity gradient in the fluid will build up perpendicular to the plates. The reason is the shear force exerted by the plates. The constant of proportionality between the shear force and the velocity gradient is the shear viscosity.
Equation (3.3) with the shear stress tensor (3.14) is known as Navier-Stokes equation.

[1]In particular, the entropy of an ideal fluid is constant

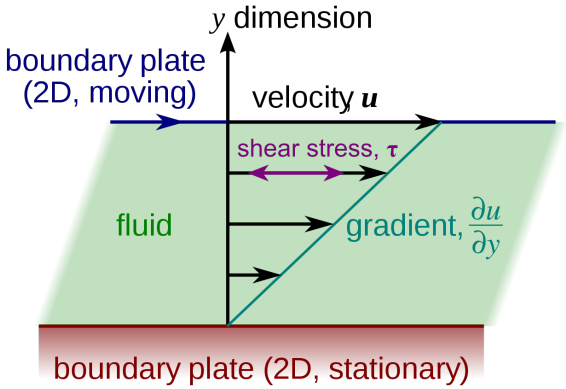

Figure 3.1: A fluid is located between two plates, which are moving relative to each other. Shear forces will indude a velocity gradient in the fluid, perpendicular to the plates.

3.2 Relativistic hydrodynamics

So far non-relativistic fluid were considered. For QCD matter, however, a Lorentz-invariant formulation of hydrodynamics is required. The relativistic generalization to non-relativistic hydrodynamics takes into account relativistic effects either due to relativistic motion of the macroscopic system or due to relativistic motion of the fluid constituents.
The central quantity is the fluid 4-velocity $u^\mu(x)$, obeying

$$u^\mu(x)u_\mu(x) = 1. \tag{3.15}$$

It is always possible to find a (local) Lorenz transformation such that

$$u^\mu(x) = (1, \vec{0}) \tag{3.16}$$

and the corresponding frame is called local fluid rest frame.
All properties of the fluid are determined by its energy-momentum tensor $T^{\mu\nu}(x)$ and - in case there is a conserved current - by the flux $J^\mu(x)$. Analog to non-relativistic hydrodynamics, where the constitutive equations (3.1)-(3.3) were expanded in gradients of the fluid velocity, the energy-momentum tensor (and all conserved currents) is expanded in gradients of the fluid 4-velocity. The leading order and next-to-leading order results are called ideal relativistic hydrodynamics and viscous relativistic hydrodynamics, respectively.

The leading order result for the energy-momentum tensor reads

$$T^{\mu\nu}_{LO} = (\epsilon + P)u^\mu u^\nu + P\eta^{\mu\nu} \tag{3.17}$$

which is diagonal $T^{\mu\nu}_{(LRF)} = \mathrm{Diag}(\epsilon, P, P, P)$ in the local rest frame, where the convention $\eta = \mathrm{Diag}(-1, 1, 1, 1)$ is employed[2]. The correction to the energy-momentum tensor $\delta T^{\mu\nu}$ from next-to-leading order is

$$\delta T^{\mu\nu} = -\eta\Delta^{\mu\alpha}\Delta^{\nu\beta}(\partial_\alpha u_\beta + \partial_\beta u_\alpha - \tfrac{2}{3}\eta_{\alpha\beta}\partial\cdot u) - \zeta\Delta^{\mu\nu}\partial\cdot u \tag{3.18}$$

with $\Delta^{\mu\nu} = \eta_{\mu\nu} + u^\mu u^\nu$. The explicit form of the first order correction can vary, depending on the precise definition of the fluid velocity. The above expression (3.18) is consistent with the Landau frame, such that in the local rest frame $T^{00} = \epsilon$ and $T^{0i} = 0$. The complete viscous energy-momentum tensor reads

$$T^{\mu\nu} = T^{\mu\nu}_{LO} + \delta T^{\mu\nu} \tag{3.19}$$

For future use, the traceless, spatial part of the energy momentum tensor is defined as:

$$\pi^{ij} = T^{ij} - \tfrac{1}{3}\delta^{ij}T^k_k \tag{3.20}$$

In principle, the expansion in derivatives of the flow velocity can be carried out further [129]. In that sense the transport coeffcients of viscous hydrodynamics are only the leading order of the transport coefficients of the full expansion. However, for nearly perfect fluids, the leading order viscous coefficients are supposed yield already quantitaively accurate results, because the derivative expansion can be thought of an expansion in powers of the inverse Reynolds number, which is small for nearly perfect fluids. Further, experimental results for the QGP's viscosity do not yet have the precision beyond viscous hydrodynamics [130].

There are numerous studies of transport coefficients for various systems and temperature regimes. Here, only a short selection can be given. The most natural choice for a first calculation of tranport coefficients are scalar field theories with different types of interactions [131,132], the O(N)-symmetric model either for weak coupling or the large-N limit [133,134] and the Linear sigma model in the large-N-limit [135]. The examples

[2]Here, η denotes the metric, not shear viscosity.

and restrictions already indicate, that the calculation of transport coefficients is not a trivial problem, but rather needs elaborate methods, especially in non-perturbative regimes.

Of particular interest is the non-perturbative region of non-abelian gauge theories in the vicinity of the critical temperature, where the minimum of $\frac{\eta}{s}$ is expected. The results so far are quite sparse, beyond the one's mentioned already in the introduction. The perturbative regime of high temperatures gauge theories, however, is well explored [132, 136]. The main tool is the Hard Thermal Loop (HTL) expansion which, in principle, is a reorganization of the perturbation series leading to improve convergence. The detail of HTL perturbation theory will be discussed in chapter 4.

3.3 Linear response theory

In the previous section transport coefficients were defined as constants appearing in the first order correction of the energy-momentum tensor in a derivative expansion in gradients of the fluid velocity. They are characteristic for the fluid and depend on the microscopic dynamics. The connection between the macroscopic fluid and the microscopic details is established by Kubo relations, that use the concept of linear response. In this section a short introduction to linear response theory is presented. For simplicity, the non-relativistic case is considered. However, anything derived here is also valid for relativistic fluids.
Consider a Hamiltonian $H = H_0 + \lambda H_{ext}$, with ground state $|0\rangle$ of H_0 and an external perturbation H_{ext}, that is adiabatically switched on and off. Let us adress the problem of how H_{ext} changes the ground state of H_0. This is frequently used in many fields of physics: An isolated system H_0 is to be probed. Therefore, the response of the system to a small (external) perturbation λH_{ext} is studied.
Consider an observable $A(\vec{x}, t)$. The expectation value is changed by H_{ext} according to

$$\langle 0|A(\vec{x},t)|0\rangle \;\rightarrow\; \langle 0|U^{-1}(t)A(\vec{x},t)U(t)|0\rangle \tag{3.21}$$

with the time evoultion operator

$$U(t) = Te^{-i\lambda \int_{-\infty}^{t} dt' H_{ext}(t')} \tag{3.22}$$

If $\lambda > 0$ is sufficiently small, the exponential can be expanded in powers of λ:

$$U(t) \approx 1 - i\,\lambda \int_{-\infty}^{t} dt'\, H_{ext}(t') \equiv 1 - \lambda X(t) \tag{3.23}$$

The leading order correction to (3.21) is

$$\begin{aligned} \delta\langle 0|A(\vec{x},t)|0\rangle &= \langle 0|(1+\lambda X(t))A(\vec{x},t)(1-\lambda X(t))|0\rangle - \langle 0|A(\vec{x},t)|0\rangle & (3.24)\\ &= \lambda\langle [X(t), A(\vec{x},t)]\rangle + \mathbb{O}(\lambda^2) & (3.25)\\ &\approx i\,\lambda \int_{-\infty}^{t} dt' \langle [H_{ext}(t'), A(\vec{x},t)]\rangle & (3.26) \end{aligned}$$

Equation (3.26) is called the linear response to the perturbation λH_{ext}. Note, that (3.26) explicitly obeys causality, as the observed time t is always later than the times t' during which the perturbation acts.

3.4 The Kubo relations

If $A(\vec{x},t)$ is a local observable, in general, $H_{ext}(t)$ constitutes an external source, that couples linearly to $A(\vec{x},t)$:

$$H_{ext}(t) = \int d^3x\, A(\vec{x},t) f(\vec{x},t) \tag{3.27}$$

Further, if the observable is defined, such that $\langle 0|A(\vec{x},t)|0\rangle = 0$, i.e. $A(\vec{x},t)$ measures fluctuations from the expecatation value, then

$$\begin{aligned} \delta\langle 0|A(\vec{x},t)|0\rangle &= i \int_{-\infty}^{t} dt' \int d^3x'\, \langle 0|[A(\vec{x}',t'), A(\vec{x},t)]|0\rangle\, f(\vec{x}',t') & (3.28)\\ &= \int_{-\infty}^{t} dt' \int d^3x' \chi(\vec{x},t;\vec{x}',t') f(\vec{x}',t') & (3.29) \end{aligned}$$

with the (generalized) susceptibility

$$\chi(\vec{x},t;\vec{x}',t') \equiv i\,\Theta(t-t')\langle 0|[A(\vec{x}',t'), A(\vec{x},t)]|0\rangle \tag{3.30}$$

If the fluid is further isotropic with respect to the observable $A(\vec{x},t)$, χ depends on the differences $\Delta t = t - t'$ and $\Delta\vec{x} = \vec{x} - \vec{x}'$ only, giving rise to the definition

$$\chi(\vec{x},t) \equiv \chi(\vec{x},t;0,0) = -i\,\Theta(t)\langle 0|[A(\vec{x},t),A(\vec{0},0)]|0\rangle \tag{3.31}$$

The (generalized) susceptibility is nothing but the retarded Greens function of the observable $A(\vec{x},t)$. It is often useful to Fourier transform (3.31) to momentum space (such a Fourier transform is sometimes called Kubo transform)

$$\chi(p_0,\vec{p}) = -i\int d^4x\, e^{i\,p_\mu x^\mu}\langle[A(x),A(0)]\rangle_{ret} \tag{3.32}$$

In this thesis, in particular the imaginary part of $\chi(p_0\vec{p})$, the spectral function, is of interest and will be discussed in greater detail in the next chapters. Here, two spectral functions of particular interest are defined:

$$\rho_{ij,ij}(p_0,\vec{p}) = -2\,\mathrm{Im}\,i\int d^4x\, e^{i\,p_\mu x^\mu}\langle[\pi_{ij}(x),\pi_{ij}(0)]\rangle_{ret} \tag{3.33}$$

with the traceless, spatial part of the energy momentum tensor (3.20) and

$$\rho_{ii,jj}(p_0,\vec{p}) = -2\,\mathrm{Im}\,i\int d^4x\, e^{i\,p_\mu x^\mu}\langle[T_{ii}(x),T_{jj}(0)]\rangle_{ret} \tag{3.34}$$

with the energy momentum tensor (3.19).
The Kubo relations connect the spectral functions to transport coefficient. The Kubo relations follow from the fluctuation-dissipation theorem

$$\rho(p_0,\vec{p}) - \frac{\omega}{T}S(p_0,\vec{p}) \tag{3.35}$$

relating the dissipative effects described by the spectral function to the fluctuations described by

$$S(p_0,\vec{p}) = \langle\pi_{ij}\pi_{ij}\rangle_{p_0,\vec{p}} \tag{3.36}$$

for shear viscosity and

$$S(p_0,\vec{p}) = \langle T_{ii}T_{jj}\rangle_{p_0,\vec{p}} \tag{3.37}$$

for bulk viscosity. The relations (3.33) and (3.34) follow from lengthy but standard calculus. For the above spectral functions (3.33) and (3.34) the Kubo relations read:

$$\eta = \tfrac{1}{20} \lim_{p_0 \to 0} \lim_{\vec{p} \to 0} \frac{\rho_{ij,ij}(p_0, \vec{p})}{p_0} \tag{3.38}$$

$$\zeta = \tfrac{1}{18} \lim_{p_0 \to 0} \lim_{\vec{p} \to 0} \frac{\rho_{ii,jj}(p_0, \vec{p})}{p_0}. \tag{3.39}$$

Note, that besides shear and bulk viscosity, there is a third transport coefficient, thermal conductivity κ. While fluid characteristic shear and bulk viscosity assume convervation of energy and momentum, thermal conductivity is an observable if there is a conserved 4-current in the system. In non-relativistic fluids, the conserved current is mass density and the associated charge is the particle number. However, in relativistic fluids, particles can be created and annihilate. Mass is therefore no longer a suitable conserved charge. A conserved current can be charge density or the baryon number density, with the total charge and the net baryon number as associated conserved charges. Here, however, thermal conductivity will not be discussed further.
Interestingly, in the original work of Kubo neither of these transport coefficients was adressed. Kubo studied the electric conductivity σ_{el}, i.e the response of a system to an external electric field. In contrast, transport coefficients are not direct responses to external fields. They are responses to internal inhomogeneities of the fluid, that can be provoked by external forces, but, are not genuinely related a specific external force.

3.5 Shear Viscosity, Reynolds number and the AdS/CFT conjecture

In this section the magnitude of shear viscosity η is studied in more detail. For non-relativistic fluids, a fluids 'quality' is judged by the (non-relativistic) Reynolds number, whose definition is to some extend phenomenological and thus not unique. Here, the following definition is used

$$Re = \frac{n}{\eta} v L \tag{3.40}$$

with the mass density n, characteristic velocity v and characteristic length scale L of the fluid. The size of the Reynolds number gives indication to what extend the fluid tends to exhibit laminar and turbulent flows. Naturally, if the charateristic velocity is

increased, the fluid's flow will more likely to be turbulent. Let us, however, assume, that vL is held constant. Then, the Reynolds number, is governed by $\frac{\eta}{n}$. Larger shear viscosities will decrease Re, keeping the flow laminar. Thus, the 'quality' of a non-relativistic fluid can be measured by $\frac{\eta}{n}$, and the question arises, whether a non-zero lower bound exists.
The relativistic equivalent to $\frac{\eta}{n}$ is $\frac{\eta}{s}$, with entropy density s and a lower bound of

$$\frac{\eta}{s} \geq \frac{1}{4\pi} \tag{3.41}$$

was conjectured by the famous AdS/CFT conjecture. To understand the correspondence of string-theory in certain Anti-de-Sitter spaces to conformal field theory some definitions are necessary. Let $M(n,1)$ be a $(n+1)$-dimensional flat (Minkowski-)spacetime. The n-dimensional Anti-de-Sitter space AdS_n is defined as the n-dimensional hyperbolic hypersurface of $M(n,1)$ given by

$$(x_1)^2 + .. + (x_n)^2 - (x_{n+1})^2 = -1 \tag{3.42}$$

On the other hand, a conformal transformation is a change of coordinates, $x^\mu \to \tilde{x}^\mu(x)$ such that the metric transforms as

$$g_{\mu\nu}(x) -> \Omega^2(x) g_{\mu\nu}(x) \tag{3.43}$$

A field theory is conformal, if it is invariant under such transformations. The idea of the AdS/CFT correspondence is that the boundary of specific AdS-spaces is locally equivalent to a certain conformal field theory. Sometimes this is also called holographic duality [137]. The name was given, because the conformal field theory is one dimension lower than its AdS dual. Thus, the relationship is similar to a hologram and its holographic image. The AdS/CFT correspondence was first explored in many publications around the year 2000 [104, 138, 139].
On a first glance it looks far fetched to obtain information on transport coefficient from a theory of gravitation. On a second look, however, one realizes the connection, that is based on the energy-momentum tensor. It is coupled to gravity an is also related to transport coefficients by the Kubo relations.

In particular, the 5-dimensional Anti-de-Sitter space with 5 compactified extra dimensions $AdS_5 \times S^5$ is equivalent on its boundary to $\mathcal{N} = 4$ Supersymmetric Yang-Mills

theory. For this theory in the conformal limit $N_c \to \infty$ and finite $g^2 N_c$, first calculations yielded [140, 141]

$$\frac{\eta}{s} = \frac{1}{4\pi}(1 + \frac{135\zeta(3)}{8(2g^2N_c)^{3/2}} + ...) \tag{3.44}$$

with the Apery constant $\zeta(3) = 1.20205....$ A few months later Kovtun, Son and Starinets conjectured, that the lower bound (3.41) hold for 'all relativistic quantum field theories at finite temperature and zero chemical poential' [57]. To support what they called 'speculation', a simple motivation based on Heisenbergs uncertainty principle was given: Consider a fluid of particles with energy density ϵ, particle density n and mean free time τ. Shear viscosity is proportional to $\eta \approx \epsilon\tau$ and entropy density $s \approx n$. Thus $\frac{\eta}{s} \approx \frac{\tau\epsilon}{n}$. From the uncertainty principle one gets, that the energy per particle $\frac{\epsilon}{n}$ times the mean free time τ is larger than 1 and it follows $\frac{\eta}{s} \geq c$. With a universal constant $c > 0$. In particular, for $\mathcal{N} = 4$ Supersymmetric Yang-Mills theory $c = \frac{1}{4\pi}$ was found. The validity of the conjecture with this certain lower bound should be taken as a qualitative statement. Whether $c = \frac{1}{4\pi}$ will hold for all geometries is yet to be shown. Even though there is no strict mathematical proof yet for $c = \frac{1}{4\pi}$ the conjecture has not been disproven by experiment [142, 143], either. From the theory side, there is controversal discussion, and counterexamples were pointed-out [144,145]. Nevertheless, for the quark-gluon plasma, which seems to be the best candidate for a perfect fluid, that can experimentally be realized, also theoretical predictions obey the KSS-bound [146, 147].

An important task is to study the temperature dependence of $\frac{\eta}{s}$ to find the position of the minimum. Many findings indicate, that the minimum will be assumed in the vicinity of the critical temperature [148, 149], but also counterexamples are known [150–153].

4 Thermal field theory

'Auch für den Physiker ist die Möglichkeit einer Beschreibung in der gewöhnlichen Sprache ein Kriterium für den Grad des Verständnisses, das in dem betreffenden Gebiet erreicht worden ist.'
Werner Heisenberg

This chapter conveys an introduction yo thermal field theory following the general derivations and arguments given in the introductory books by Das [154] and LeBellac [155].

4.1 Introduction to TFT

Quantum field theories are usually formulated for zero temperature. In an experimental setup such a description is valid, for temperatures small compared to the relevant energy scales, like particles masses or dynamically generated scales. There are however situations, where temperature is not small at all. Examples are the early universe or heavy-ion collisions. Indeed, both system develop from a temperature dominated regime to a regime where temperature, again, becomes an irrelevant scale and zero temperature field theory is applicable.

Thermal Field Theory (TFT), or finite temperature field theory, is a generic quantum field theory to describe interacting many-body systems in a thermodynamical environment. TFT was developed in the early 1970's in the context of early universe studies where the quark-gluon-plasma, before the confinement transition, was almost perfectly thermalized [156]. Especially the discussion of spontaneously broken gauge theories at finite temperature demonstrated the applicability of TFT for the first time in High Energy Physics [157, 158]. TFT has become a central tool also in astrophysics

where in the core of neutron stars and super novae a very dense plasma is present [159].

There are two conceptually different approaches to TFT: The imaginary-time formalism and the real-time formalism. The imaginary-time formalism, or Matsubara formalism, exploits the similarity between the density matrix for a system in thermal equilibrium and the time evolution operator for imaginary times. Within the ITF the time variable is traded in for temperature, so that dynamical, time dependent processes can only be studied after a non-trivial analytic continuation. The real-time formalism on the other hand can deal with time-dependent quantities but is formally more demanding. Here, both formalisms are discussed and applied to a generic one-loop expression.

Further, for a non-Abelian gauge theory like SU(N), for suffficiently high temperatures, the theory can be described perturbatively, due to asymptotic freedom. However, there are some sublteties involved, and conventional perturbation theory breaks down early, because of infrared divergencies. By resumming certain subsets of diagrams over all orders of perturbation theory, a finite series is obtained, called Hard Thermal Loop expansion (HTL). The theory is introduced and a HTL result for the shear viscosity is derived.

4.2 Imaginary-time Formalism

The imaginary time formalism dates back to the work of Matsubara [160] and is based on a close connection of finite temperature field theory and statistical equilibrium thermodynamics. Therefore it is enlightening to review the basictypes concepts of statistical thermodynamics. The central quantity of this theory is the density matrix (for the canonical ensemble)

$$\rho(\beta) = e^{-\beta H} \tag{4.1}$$

where H is the respective Hamiltonian for the system under consideration and $\beta = \frac{1}{T}$ is the inverse equilibrium temperature. One can define the partition function

$$Z(\beta) = \mathrm{Tr}\, \rho(\beta) \tag{4.2}$$

where the trace is taken over a complete set of states. The (ensemble) average of any operator A in the Schrödinger picture is

$$\langle A\rangle_\beta = Z^{-1}(\beta)\mathrm{Tr}\,\rho(\beta)A = \frac{\mathrm{Tr}\,e^{-\beta H}A}{\mathrm{Tr}\,e^{-\beta H}} \tag{4.3}$$

After switching to the Heisenberg picture by dressing the Schrödinger operator with time evolution

$$A_H(t) = e^{iHt}Ae^{-iHt} \tag{4.4}$$

and considering the special case $A_H(t-t') = B_H(t)C_H(t')$ one finds after inserting into (4.3):

$$\begin{aligned}
\langle B_H(t)C_H(t')\rangle_\beta &= Z^{-1}(\beta)\mathrm{Tr}\,\rho(\beta)B_H(t)C_H(t') && (4.5)\\
&= Z^{-1}(\beta)\mathrm{Tr}\,e^{-\beta H}B_H(t)e^{\beta H}e^{-\beta H}C_H(t') && (4.6)\\
&= Z^{-1}(\beta)\mathrm{Tr}\,B_H(t+i\beta)e^{-\beta H}C_H(t') && (4.7)\\
&= Z^{-1}(\beta)\mathrm{Tr}\,e^{-\beta H}C_H(t')B_H(t+i\beta) && (4.8)\\
&= \langle C_H(t')B_H(t+i\,\beta)\rangle_\beta && (4.9)
\end{aligned}$$

Here, one already observes the aforementioned connection between temperature and imaginary time. By setting $B = C = A$, equation (4.9) yields:

$$\langle A_H(t)A_H(t')\rangle_\beta = \langle A_H(t')A_H(t+i\,\beta)\rangle_\beta \tag{4.10}$$

Equation (4.10), the so called Kubo-Martin-Schwinger (KMS) relation, describes a periodicity condition for correlation functions at finite temperature, or equivalent a compactification of the (euclidean) 0-component. The similarity between temperature and a compactified imaginary time evolution might just be a coincidence rooted in the form of the time evolution operator. There might also be some deeper connection, that has not yet been fully understood. To connect the above to field theory the following is observed: If the Hamiltonian can be split into a free part H_0 and a part containing all interaction H' so that the full Hamiltonian is $H = H_0 + H'$, the same can be done (artificially) for the density matrix (4.1):

$$\rho(\beta) = \rho_0(\beta)\rho_{int}(\beta) \tag{4.11}$$

with

$$\rho_0(\beta) = e^{-\beta H_0}, \quad \rho_{int}(\beta) = e^{\beta H_0} e^{-\beta H} \tag{4.12}$$

It it obvious from (4.11) and (4.12) that $\rho_0(\beta)$ and $\rho_{int}(\beta)$ satisfy 'time evolution equations'

$$\frac{\partial \rho_0(\tau)}{\partial \tau} = -H_0 \rho_0(\tau) \tag{4.13}$$

$$\frac{\partial \rho_{int}(\tau)}{\partial \tau} = -H_{int}(\tau) \rho_{int}(\tau) \tag{4.14}$$

with the interaction Hamiltonian

$$H_{int}(\tau) = \rho_0^{-1}(\tau) H' \rho_0(\tau) \tag{4.15}$$

and the interpretation of $0 < \tau \leq \beta$ as a continuous variable. Equation (4.14) can be integrated to yield

$$\rho_{int}(\beta) = T_\tau \, e^{-\int_0^\beta d\tau H_{int}(\tau)} \tag{4.16}$$

with the ordering operator T_τ. For $T \to 0$ (4.16) gives the zero temperature expression for the S-matrix. Therefore, (4.16) is its thermal equivalent and is well-suited to derive a diagrammatic expansion of the theory, simililar to zero-temperature field theory.
Let us consider a complex scalar field theory with field ϕ. The aim is to calculate 2-point correlation functions $G_\beta(\tau - \tau')$. To straighten the notation, the β-subscript is dropped for all correlation functions and expectation values for the remaining part of this chapter. The 2-point correlation function yields

$$G(\tau - \tau') = \langle T_\tau \phi_H(\tau) \phi_H^\dagger(\tau') \rangle = \frac{\langle T_\tau \phi_{int}(\tau) \phi_{int}^\dagger(\tau) \rho_{int}(\beta) \rangle_0}{\langle \rho_{int}(\beta) \rangle_0} \tag{4.17}$$

with $\phi_H(\tau) = \rho_{int}^{-1}(\tau) \phi_{int}(\tau) \rho_{int}(\tau)$. Further, the cyclicity of the trace operator was used. The subcript '0' denotes that the average is calculated with respect to the non-interacting system. Let us first observe, that the thermal Greens function (4.17) is periodic: The (imaginary) time arguments are restricted to the interval $0 \leq \tau, \tau' \leq \beta$. Therefore, the Greens function is defined for $-\beta \leq \tau - \tau' \leq \beta$. However, identifying $\tau = -i\,t$, the KMS relation (4.10) yields:

$$G(-\tau) = G(\tau + \beta) \quad (0 \leq \tau \leq \beta) \tag{4.18}$$

As a direct consequence, only a dicrete set of frequencies contribute to the Fourier transform of (4.17):

$$G(\tau) = \frac{1}{\beta} \sum_n e^{-i\,\omega_n \tau} G(\omega_n) \tag{4.19}$$

In equation (4.19) ω_n are the (bosonic) Matsubara frequencies

$$\omega_n = \frac{2\pi n}{\beta} \tag{4.20}$$

Note, that a similar derivation is possible for fermionic fields with slightly more notational effort, due to the their Grassmannian nature. However, (4.19) is valid for fermionic fields with the fermionic Matsubara frequencies

$$\omega_n = \frac{(2n+1)\pi}{2\beta} \tag{4.21}$$

4.2.1 Scalar example: Imaginary-time Formalism

In this paragraph the scalar field theory example from [132] with Euclidean Lagrangian

$$\mathcal{L} = \frac{1}{2}\partial_\mu \phi \partial^\mu \phi + U(\phi^2). \tag{4.22}$$

is considered. The corresponding energy-momentum tensor is given by

$$T^{\mu\nu} = \frac{\delta S}{\delta g_{\mu\nu}} = \partial^\mu \phi \partial^\nu \phi - \eta^{\mu\nu}\mathcal{L}. \tag{4.23}$$

The spatial traceless part - according to (3.20) reads

$$\pi^{ij} = \partial^i \phi \partial^j \phi - \frac{1}{3}\delta^{ij}\partial^k \phi \partial^k \phi \tag{4.24}$$

and gives rise to vertices (p and q denote incoming momenta of the scalars)

$$V^{ij}_{\pi\phi\phi}(p,q) = -p^i q^j + \frac{1}{3}\delta^{ij} p \cdot q \tag{4.25}$$

The (leading order contribution to the) Euclidean correlation function of the energy-momentum tensor is obtained by evaluating a 1-loop diagram

$$G^E_{\pi\pi}(p) = T \sum_n \int \frac{d^3 q}{(2\pi)^3} V^{ij}_{\pi\phi\phi}(q, q+p) V^{kl}_{\pi\phi\phi}(q+p, q) G^E_\phi(q+p) G^E_\phi(q). \tag{4.26}$$

Inserting the spectral representation

$$G_\phi^E(q^0,\vec{q}) = \int \frac{d\omega}{(2\pi)} \frac{\rho(\omega,\vec{q})}{\omega - i\,q^0} \tag{4.27}$$

for the boson propagator one can write

$$G_\phi^E(q)G_\phi^E(q+p) = \int \frac{d\omega}{(2\pi)} \int \frac{d\omega'}{(2\pi)} \frac{\rho(\omega,\vec{q})\rho(\omega',\vec{q}+\vec{p})}{(\omega - i\,q^0)(\omega' - i\,q^0 - i\,p^0)}. \tag{4.28}$$

Next, the Matsubara sum is evaluated still for Euclidean external momentum [1]

$$T \sum_{q^0=2\pi nT} \frac{1}{(\omega - i\,q^0)(\omega' - i\,q^0 - i\,p^0)} = \frac{n_B(\omega) - n_B(\omega')}{\omega' - \omega - i\,p^0}, \tag{4.29}$$

where the periodicity $n_B(\omega + i\,p^0) = n_B(\omega)$ for $p^0 = 2\pi nT$ is exploited. Thus one gets

$$G_{\pi\pi}^E(p) = \int \frac{d^3q}{(2\pi)^3} \int \frac{d\omega}{(2\pi)} \int \frac{d\omega'}{(2\pi)} V_{\pi\phi\phi}^{ij}(q,q+p)V_{\pi\phi\phi}^{kl}(q+p,q)\rho(\omega,\vec{q})\rho(\omega',\vec{q}+\vec{p}) \tag{4.30}$$

$$\times \frac{n_B(\omega) - n_B(\omega')}{\omega' - \omega - i\,p^0} \tag{4.31}$$

The aim is to calculate the spectral function (3.33) of the spatial traceless part of the energy-momentum tensor:

$$\rho_{\pi\pi}(\omega,\vec{p}) = -2\,\mathrm{Im}\,G_{\pi\pi}^R(\omega,\vec{p}) = 2 \lim_{\epsilon\to 0^+} \mathrm{Im}\,G_{\pi\pi}(-i\,(\omega + i\,\epsilon),\vec{p}), \tag{4.32}$$

where the ϵ prescription ensures the occurrence of the retarded propagator. Applying the Sokhotski-Plemelj theorem [161]

$$\lim_{\epsilon\to 0^+} \int_a^b \frac{f(x)}{x \pm i\,\epsilon} dx = \mp i\,\pi f(0) + \mathcal{P} \int_a^b \frac{f(x)}{x} dx, \tag{4.33}$$

the imaginary part in (4.32) picks out the delta function contribution, yielding

$$\rho_{\pi\pi}^{ijkl}(\omega,\vec{p}) = \int \frac{d^4q}{(2\pi)^4} V_{\pi\phi\phi}^{ij}(q,q+p)V_{\pi\phi\phi}^{kl}(q+p,q)\rho(q^0,\vec{q})\rho(q^0+\omega,\vec{q}+\vec{p})(n_B(q^0)-n_B(q^0+\omega)). \tag{4.34}$$

[1] This step has to involve terms from the vertex if they- unlike here- depend on the zeroth component of the momentum.

In particular for vanishing spatial external momentum and after taking the trace over external indices and including a symmetry factor of 2 one finds

$$\begin{aligned}\rho_{\pi\pi}(\omega,\vec{0}) &= \frac{4}{3}\int \frac{d^4q}{(2\pi)^4}(\vec{q}\cdot\vec{q})^2\rho(q^0,\vec{q})\rho(q^0+\omega,\vec{q})(n_B(q^0)-n_B(q^0+\omega)) \\ &= \frac{4}{3}\int \frac{d^4q}{(2\pi)^4}(\vec{q}\cdot\vec{q})^2\rho(q^0,\vec{q})\left(\rho(q^0+\omega,\vec{q})-\rho(q^0-\omega,\vec{q})\right)n_B(q^0),\end{aligned} \tag{4.35}$$

which matches [132].

4.3 Real-time Formalism

As in the imaginary-time formalism, the starting point to develop the real-time formalism is the density matrix of a generic quantum system with Hamiltonian $H(t)$, that - unlike in the imaginary time formalism - is allowed to be time dependent. Here, however, not the connection between imaginary time evolution and classical statistical mechanics is exploited, but time is treated as a real variable:

$$\rho(t) = U(t,0)\rho(0)U^\dagger(t,0) \tag{4.36}$$

describes the (real-)time evolution of the density matrix, with the time evolution operator defined by

$$i\,\frac{\partial U(t_1,t_2)}{\partial t_1} = H(t_1)U(t_1,t_2) \tag{4.37}$$

with the normalisation condition $U(t,t) = 1$. Let us prepare the system in some equilibrium state at (inverse) temperature β at some large negative time $-T$ given by a time independent (initial) Hamiltonian H_{in}, so that for time $t = 0$ the density matrix reads

$$\rho(0) = \frac{e^{-\beta H_{in}}}{Tr\, e^{-\beta H_{in}}} = \frac{U(-T-i\,\beta,-T)}{Tr\, U(-T-i\,\beta,-T)} \tag{4.38}$$

For $t \geq 0$ the time-dependent Hamiltonian $H(t)$ is (adiabatically) switched on such that the full Hamiltonian can be written as:

$$\mathbf{H}(t) = \begin{cases} H_{in} & : t < 0 \\ H(t) & : t \geq 0 \end{cases}$$

When equation (4.38) is inserted into (4.36) one finds

$$\rho(t) = \frac{U(t,0)U(-T-i\,\beta,-T)U(0,t)}{Tr\,U(-T-i\,\beta,-T)} \tag{4.39}$$

This allows to calculate expectation values of arbitrary operators A:

$$\begin{aligned}
\langle A\rangle(t) &= \mathrm{Tr}\rho(t)A && (4.40)\\
&= \frac{U(t,0)U(-T-i\,\beta,-T)U(0,t)A}{Tr\,U(-T-i\,\beta,-T)} && (4.41)\\
&= \frac{U(-T-i\,\beta,-T)U(0,t)AU(t,0)}{Tr\,U(-T-i\,\beta,-T)} && (4.42)\\
&= \frac{U(-T-i\,\beta,-T)U(0,t)AU(t,0)U(0,-T)U(-T,0)}{Tr\,U(-T-i\,\beta,-T)} && (4.43)\\
&= \frac{U(-T-i\,\beta,-T)U(-T,0)U(0,t)AU(t,0)U(0,-T)}{Tr\,U(-T-i\,\beta,-T)} && (4.44)\\
&= \frac{U(-T-i\,\beta,-T)U(-T,t)AU(t,-T)}{Tr\,U(-T-i\,\beta,-T)} && (4.45)\\
& && (4.46)
\end{aligned}$$

where a 1 was inserted in the form $1 = U(0,-T)U(-T,0)$. Further the cyclicity of the trace operator as well as commutation of the time evolution operators $U(-T-i\,\beta,-T)$ and $U(-T,0)$ was used. Now, another $1 = U(-T,T)U(T,-T)$ is inserted both in numerator and denominator to yield:

$$\begin{aligned}
\langle A\rangle(t) &= \frac{U(-T-i\,\beta,-T)U(-T,T)U(T,-T)U(-T,t)AU(t,-T)}{Tr\,U(-T-i\,\beta,-T)U(-T,T)U(T,-T)} && (4.47)\\
&= \frac{U(-T-i\,\beta,-T)U(-T,T)U(T,t)AU(t,-T)}{Tr\,U(-T-i\,\beta,-T)U(-T,T)U(T,-T)} && (4.48)
\end{aligned}$$

The meaning of(4.48) is straightforward: The time evolution of any operator average at finite temperature can be computed by evaluating the evolution of the system along the time path given by the RHS of (4.48): The system evolves from large negative time -T to some time t at which the operator A is inserted. Then it evolves further to large positive time T and backwards along the real time axis to the initial negative time. Finally the system evolves along the imaginary axis to $-T-i\,\beta$.

This is realized by shifting the backwards branch of the contour by $-i\,\sigma$ with $0 < \sigma < \beta$. The choice of σ defines different classes of real-time formalisms, with advantages and disadvantages in notational effort. Popular choices are the Keldysh-contour with $\sigma = \epsilon$

for some infinitesimal $\epsilon > 0$ and the symmeric contour for $\sigma = \beta/2$. As any averages obviously do not depend one the choice of σ, the Keldish contour is used in this thesis. The different branches of the contour are denoted by $C_{\pm}, C_2, C_4$ as shown in Fig.4.1, so that the complete path in the complex plane is $C = C_+ \oplus C_2 \oplus C_- \oplus C_4$. For the scalar field theory of the previous section, (4.48) gives rise for the definition of the generating functional

$$Z[J_C] = \int D\phi e^{i \int_C dt \int d^3x (\mathcal{L} + J_C \phi)} \tag{4.49}$$

with the branch dependent sources J_c. It can be shown that the contribution of

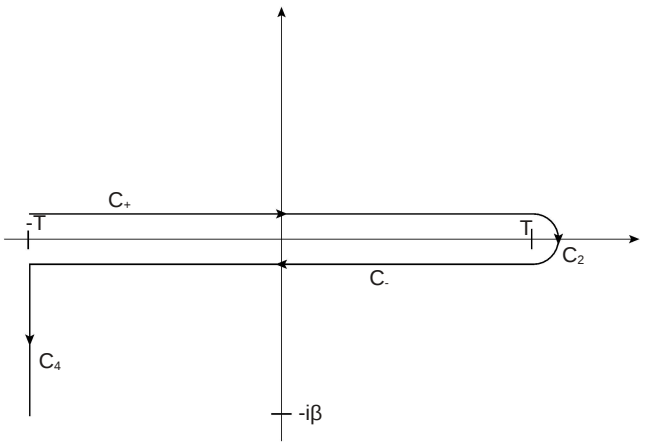

Figure 4.1: Keldysh countour in the real-time formalism.

$C_{24} = C_2 \oplus C_4$ factorizes and can be absorbed in a temperature dependent normalisation [155]. For the averages, the normalisation both appears in numerator and denominator (see (4.48)) and cancels. Therefore the respective sources are set to zero, and one remains with the Keldysh closed time path given by $C_{+-} = C_+ \oplus C_-$ and the sources $J_{\pm}$. There are two implementations of the two contour branches. In the first, one

attaches a label to the time variable, defining the branch it lies on. The second, which will be used here, is to double the field degrees of freedom and introduce $\phi_\pm$ living on the respective branches. By this trick, time can be treated as a real valued variable without any indexing and the two branches are absorbed into the fields. Irrespective of the implementation, the 2-point functions become matrix valued due to the doubling of fields (or of the time indices):

$$G_{\pm\pm}(x,y) = -i \left\langle T_C \phi_\pm(x) \phi_\pm(y) \right\rangle \tag{4.50}$$

with the time ordering operator along the contour T_C. The matrix elements are:

$$\begin{aligned}
G^{++}(x,y) &:= \langle T\phi_+(x)\phi_+(y)\rangle =: G_F(x,y) && (4.51)\\
G^{+-}(x,y) &:= \langle \phi_-(y)\phi_+(x)\rangle =: G_<(x,y) && (4.52)\\
G^{-+}(x,y) &:= \langle \phi_-(x)\phi_+(y)\rangle =: G_>(x,y) && (4.53)\\
G^{--}(x,y) &:= \langle T^*\phi_-(x)\phi_-(y)\rangle =: G_{\tilde{F}}(x,y) && (4.54)\\
& && (4.55)
\end{aligned}$$

where T now denotes the usual time ordering operator and $\tilde{T}$ the anti-time ordering operator. Using the definition of the retarded propagator one obtains

$$G_R(x,y) = G_{++}(x,y) - G_{+-}(x,y)\,. \tag{4.56}$$

4.3.1 Symmetry relations for the propgator

The Real-Time formalism constitutes a key method to derive the diagrammatic expressions for the spectral function of the energy-momentum tensor correlation functions. Therefore, in this section the symmetry properties of $G_{\pm,\pm}(x,y)$ are discussed in some detail.

The components $G_{\pm,\pm}$ of the propagator obey some very convenient relations. In particular,

$$G^*_{-+}(x,y) = -G_{+-}(x,y)\,. \tag{4.57}$$

First, note that for a real, classical scalar field, the corresponding quantum field is a self-adjoint operator (at least symmetric), i.e. $\phi^\dagger = \phi$, and so is the Hamiltonian. Then

one can deduce

$$\begin{aligned} G^*_{-+}(x,y) =& \left(-i \, \frac{\mathrm{Tr}\, \left(e^{-\beta H} \, \phi(x)\phi(y) \right)}{\mathrm{Tr}\, e^{-\beta H}} \right)^* = i \sum_n \frac{\langle f_n \, , \, e^{-\beta H} \phi(x)\phi(y) \, f_n \rangle^*}{\mathrm{Tr}\, e^{-\beta H}} \\ =& i \sum_n \frac{\langle e^{-\beta H} \phi(x)\phi(y) f_n \, , \, f_n \rangle}{\mathrm{Tr}\, e^{-\beta H}} = i \sum_n \frac{\langle f_n \, , \phi(y)^\dagger \phi(x)^\dagger \left(e^{-\beta H} \right)^\dagger \, f_n \rangle}{\mathrm{Tr}\, e^{-\beta H}} \qquad (4.58) \\ =& i \sum_n \frac{\langle f_n \, , e^{-\beta H} \phi(y)\phi(x) \, f_n \rangle}{\mathrm{Tr}\, e^{-\beta H}} \qquad (4.59) \\ =& - G_{+-}(x,y) \qquad (4.60) \end{aligned}$$

which proves equation (4.57). In the above proof f_n is a complete set of asymptotic states. Further, it is used that the operators are symmetric, that the exponential of a symmetric operator is again symmetric and the cyclicity of the trace.
The above identity can also be proven using the machinery of thermo field dynamics, where one constructs a finite temperature vacuum state $f_{0,\beta}$. With such a state one can simply generalize the definition of correlation functions at zero temperature to finite temperature ones by

$$\langle A_1 ... A_n \rangle := \langle f_{0,\beta} \, , \, A_1 ... A_n f_{0,\beta} \rangle \, . \qquad (4.61)$$

With this formalism at hand, relation (4.57) is derived via

$$\begin{aligned} G^*_{-+}(x,y) =& \left(-i \, \langle f_{0,\beta} \, , \, \phi(x)\phi(y) f_{0,\beta} \rangle \right)^* = i \, \langle \phi(x)\phi(y) f_{0,\beta} \, , \, f_{0,\beta} \rangle \\ =& i \, \langle f_{0,\beta} \, , \, \phi(y)^\dagger \phi(x)^\dagger f_{0,\beta} \rangle = i \, \langle f_{0,\beta} \, , \, \phi(y)\phi(x) f_{0,\beta} \rangle \qquad (4.62) \\ =& - G_{+-}(x,y) \, . \qquad (4.63) \end{aligned}$$

By Fourier transform this can be written in momentum space

$$\begin{aligned} G^*_{-+}(p,q) =& \mathcal{FT} \left\{ G_{-+}(x,y) \right\}^* = \left(\int_x \int_y e^{ipx} e^{ipy} G_{-+}(x,y) \right)^* = \int_x \int_y e^{-ipx} e^{-ipy} G^*_{-+}(x,y) \\ =& - \int_x \int_y e^{-ipx} e^{-ipy} G_{+-}(x,y) = -G_{+-}(-p,-q) \, . \qquad (4.64) \end{aligned}$$

Note that the tilde is dropped that indicates the Fourier transform since the arguments are written out explicitly. Under the assumption that the system is space-time translation invariant, the position space propagator is not an arbirtary function of (x,y), but depends only on the difference, i.e.

$$G(x,y) = G(x-y) \, . \qquad (4.65)$$

Therefore a Fourier-transform can be carried out with respect to $z := x - y$:

$$\mathcal{FT}\left\{G(x-y)\right\} = \int_z e^{ipz} G(z) = G(p)\,. \tag{4.66}$$

With this at hand, and using the obvious relation $G_{-+}(x,y) = G_{+-}(y,x)$ (following immediately from (4.52) and (4.53)) , which now translates into $G_{-+}(z) = G_{+-}(-z)$ one immediately arrives at

$$\begin{aligned} G_{-+}(p) &= \int_z e^{ipz} G_{-+}(z) = \int_z e^{ipz} G_{+-}(-z) \\ &= \int_z e^{-ipz} G_{+-}(z) \\ &= G_{+-}(-p) \end{aligned} \tag{4.67}$$

and therefore

$$\begin{aligned} G^*_{-+}(p) &= \left(\int_z e^{ipz} G_{-+}(z)\right)^* = \int_z e^{-ipz} G^*_{-+}(z) = -\int_z e^{-ipz} G_{+-}(z) \\ &= -\int_z e^{-ipz} G_{-+}(-z) = -\int_z e^{ipz} G_{-+}(z) = -G_{-+}(p)\,. \end{aligned} \tag{4.68}$$

Analog to (4.27) the real-time Greens functions can be related to the spectral function. These relations are derived in chapter 5, but are used here without proof:

$$\begin{aligned} G_{++}(p^0,\vec{p}) &= \int \frac{dp^{0\prime}}{2\pi i} \frac{\rho(p^{0\prime},\vec{p})}{p^0 - p^{0\prime} + i\,\epsilon} - n(p^0)\rho(p^0,\vec{p}) \\ &= \mathcal{P}\int \frac{dp^{0\prime}}{2\pi i} \frac{\rho(p^{0\prime},\vec{p})}{p^0 - p^{0\prime}} - (n(p^0) + \tfrac{1}{2})\rho(p^0,\vec{p}) \end{aligned} \tag{4.69}$$

$$G_{+-}(p^0,\vec{p}) = G_< = -\rho(p^0,\vec{p}) n(p^0) \tag{4.70}$$

$$G_{-+}(p^0,\vec{p}) = G_> = -\rho(p^0,\vec{p})(n(p^0)+1) \tag{4.71}$$

$$G_{--}(p^0,\vec{p}) = -\int \frac{dp^{0\prime}}{2\pi i} \frac{\rho(p^{0\prime},\vec{p})}{p^0 - p^{0\prime} - i\,\epsilon} - n(p^0)\rho(p^0,\vec{p}) \tag{4.72}$$

$$= -\mathcal{P}\int \frac{dp^{0\prime}}{2\pi i} \frac{\rho(p^{0\prime},\vec{p})}{p^0 - p^{0\prime}} - (n(p^0) + \tfrac{1}{2})\rho(p^0,\vec{p}). \tag{4.73}$$

Spectral and statistical function are related to $G^<$ and $G^>$ via

$$\begin{aligned} \rho(p^0,\vec{p}) &= G_< - G_> = G^A - G^R \\ F(p^0,\vec{p}) &= \frac{1}{2i}(G_< + G_>) = -i\,\rho(p^0,\vec{p})\left(n(p^0) + \tfrac{1}{2}\right), \end{aligned} \tag{4.74}$$

where the the KMS condition (4.10) is used, and the retarded/advanced propagators are given by

$$\begin{aligned} G^{R/A}(p^0,\vec{p}) &= G_{++}(p) - G_{\pm\mp}(p) \\ &= \mathcal{P}\int \frac{dp^{0\prime}}{2\pi i}\frac{\rho(p^{0\prime},\vec{p})}{p^0-p^{0\prime}} \pm \tfrac{1}{2}(G_>(p^0,\vec{p}) - G_<(p^0,\vec{p})) \end{aligned} \tag{4.75}$$

Furthermore, the following relations hold and are obvious corollaries from the derivation of the spectral representation derived in chapter 5:

$$G_{++}(p) + G_{--}(p) = G_{+-}(p) + G_{-+}(p) \tag{4.76}$$

$$G_{++}(p)^* = -G_{--}(p) \qquad G_{\pm\pm}(-p) = G_{\pm\pm}(p) \tag{4.77}$$

$$G_{\pm\mp}(p)^* = -G_{\pm\mp}(p) \qquad G_{\pm\mp}(-p) = G_{\mp\pm}(p) \tag{4.78}$$

$$F^*(p) = F(p) \qquad \rho^*(p) = -\rho(p) = \rho(-p) \tag{4.79}$$

$$G^R(p)^* = G^A(p) \qquad G^R(-p) = G^A(p) \tag{4.80}$$

$$n_B(-x) = -1 - n_B(x) \tag{4.81}$$

4.3.2 Scalar Example: Real-time formalism

The 1-loop example of section 4.2.1 is recalculated in the real-time formalism. The one-loop contribution to the retarded Greens function $G^R_{\pi\pi}(p)$ of the energy-momentum tensor (4.24) is given in the real-time formalism by

$$G^R_{\pi\pi}(p) = i\int_q (i\,V_{\pi\phi\phi})^2\,(G_{++}(q+p)G_{++}(q) - G_{+-}(q+p)G_{-+}(q)) \tag{4.82}$$

Using the relations from the previous section the propagators are expressed in the Keldysh basis via F, G^A and G^R,

$$G_{\pm\pm} = i\,F \pm \tfrac{1}{2}\left(G^A + G^R\right) \tag{4.83}$$

$$G_{\pm\mp} = i\,F \pm \tfrac{1}{2}\left(G^A - G^R\right) = G_{\lessgtr}, \tag{4.84}$$

which leads to

$$\Delta G^R_{\pi\pi}(p) = \frac{i}{2}\int_q V^2_{\pi\phi\phi}(G^A(q+p)G^A(q) + G^R(q+p)G^R(q) \tag{4.85}$$

$$- 2i\,(F(q+p)G^A(q) + G^R(q+p)F(q))). \tag{4.86}$$

The first two contributions vanish as one can close the integration contour in the upper/lower halfplane where are no poles. The imaginary part is now given by

$$2\mathrm{Im}\Delta G^R_{\pi\pi}(p) = i\int_q V^2_{\pi\phi\phi}\left(F(q+p)G^A(q) - F(q+p)G^R(q) + G^R(q+p)F(q) - G^A(q+p)F^q\right) \tag{4.87}$$

$$= i\int_q V^2_{\pi\phi\phi}\left(\rho(q)F(q+p) - \rho(q+p)F(q)\right) \tag{4.88}$$

$$= \int_q V^2_{\pi\phi\phi}\rho(q)\rho(q+p)(n(q^0) - n(q^0+p^0)), \tag{4.89}$$

where the definition of the spectral function and the KMS condition was used.
In order to match the result obtained in the imaginary-time formalism (4.35), the zero-component of the loop intergation is shifted by p^0 in the second term on the RHS of (4.89). This proofs finishes the proof of the equivalancy of both formalisms for the evaluation of the presented one-loop integral. For higher loop integrals the is more cumbersome to establish the equivalency, but it holds nevertheless.

4.4 Hard Thermal Loop expansion

The main result of this thesis, the temperature depedence of $\frac{\eta}{s}$, is extrapolated to the perturbative regime of high temperatures. It turns out, that conventional perturbation theory can be improved by reorganizing the perturbation series. The reason is, that at finite temperature, infrared divergencies occur, such that diagrams with superficially higher order have contributions of equal magnitude compared to lower order diagrams. In this section a short introduction of the main ideas of HTL resummed perturbation theory is given. For simplicity, in what follows ϕ^4-theory is employed. Consider the 2-loop contribution to the scalar self-energy diagram in Fig.4.2. It is proportional to

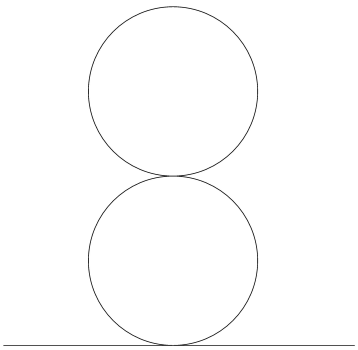

Figure 4.2: Double-bubble contribution to the self-energy in ϕ^4-theory.

$$F_{2-loop} \approx g^4 \left(T \sum_n \int \frac{d^3\vec{p}}{(2\pi)^3} \frac{1}{\omega_n^2 + \vec{p}^2} \right)^2 T \sum_{n'} \int \frac{d^3\vec{q}}{(2\pi)^3} \frac{1}{(\omega_{n'}^2 + \vec{q}^2)^2} \tag{4.90}$$

The second integral in (4.90) is infrared divergent due to the middle loop. In particular, the source for the divergence comes form the the zeroth Matsubara mode. Similar divergencies also appear in diagrams of higher orders. However, in practice the IR-divergence is screened by a thermally generated mass

$$m_{th}^2 = \frac{g^2}{24} T^2. \tag{4.91}$$

This can be incorporated by an effective propagator

$$G(p) = \frac{1}{p^2 + m^2} \tag{4.92}$$

For hard momenta $p \approx T$ the thermal mass can be omitted, while it constitutes an effective cutoff for soft momenta. The contribution of the two-bubble in Fig.4.2 with the effective propagator (4.92) contributes at order g^3 instead of g^4, as naively expected. It can be shown, that at any order of conventional perturbation series, there are diagrams, that effectively contribute to order g^3. Clearly, that signals, that a conventional perturbative series, will not converge. To get a consistent series, an infinite subset of superficially higher order must be resummed. The details are found in [162].

5 Spectral functions

'Nothing in life is to be feared, only to be understood.
Now is the time to understand more, so less is to be feared.'
Marie Curie

The spectral function is the central object of this thesis. In this chapter the basic definitions are established and the spectral representations of the two-point correlation functions in the Real-Time formalism and the Imaginary-Time formalism are derived. It will be shown that the both the real-time 2-point correlation functions and the Matsubara 2-point correlation functions can be expressed in thermal equilibrium by a single spectral function.

5.1 Spectral Representation in the real-time formalism

In this section the spectral representation for real-time two-point correlation functions is derived.

5.1.1 Off-diagonal elements of the real-time propagator

With a complete set f_i of generalized eigenfunctions of Hamiltonian H with eigenvalues E_i, the spectral representation for $G_{-+}(x,y)$ is derived as follows,

$$\begin{aligned}
G_{-+}(x,y) =& \frac{-i}{Z_\beta} \operatorname{Tr}\left(e^{-\beta H}\,\phi(x)\phi(y)\right) = \frac{-i}{Z_\beta}\sum_n \langle f_n\,,\, e^{-\beta H}\phi(x)\phi(y)\,f_n\rangle \\
=& \frac{-i}{Z_\beta}\sum_n\sum_m e^{-\beta E_n}\langle f_n\,,\,\phi(x) f_m\rangle\langle f_m\,,\,\phi(y) f_n\rangle \\
=& \frac{-i}{Z_\beta}\sum_n\sum_m e^{-\beta E_n}\langle f_n\,,\, e^{-iPx}\phi(0)e^{iPx} f_m\rangle\langle f_m\,,\, e^{-iPy}\phi(0)e^{iPy} f_n\rangle \\
=& \frac{-i}{Z_\beta}\sum_n\sum_m e^{-\beta E_n}\langle e^{iPx} f_n\,,\,\phi(0)e^{iHx} f_m\rangle\langle e^{iPy} f_m\,,\,\phi(0)e^{iPy} f_n\rangle \\
=& \frac{-i}{Z_\beta}\sum_n\sum_m e^{-\beta E_n}e^{ip_n x}e^{-ip_m x}e^{ip_m y}e^{-ip_n y}\langle f_n\,,\,\phi(0) f_m\rangle\langle f_m\,,\,\phi(0) f_n\rangle \\
=& \frac{-i}{Z_\beta}\sum_n\sum_m e^{-\beta E_n}e^{ip_n(x-y)}e^{-ip_m(x-y)}\left|\langle f_n\,,\,\phi(0) f_m\rangle\right|^2\,,
\end{aligned} \tag{5.1}$$

with the partition function

$$Z_\beta = \operatorname{Tr} e^{-\beta H}\,. \tag{5.2}$$

In the above equation it is used that the energy-momentum operator P has eigenvalues p, generates space-time translations and acts as

$$\phi(0) = e^{iPx}\phi(x)e^{-iPx} \tag{5.3}$$

on the fields, that P is symmetric and the anti-linearity of the complex inner product. The spectral density of the $-+$ two-point function in momentum space is defined as

$$\tilde\rho_{-+}(p) := \frac{1}{Z_\beta}\sum_n\sum_m e^{-\beta E_n}(2\pi)^4\delta(p_n - p_m + p)\left|\langle f_n\,,\,\phi(0) f_m\rangle\right|^2\,, \tag{5.4}$$

which is obviously a real (in momentum space!), and positive(-semi) definite quantity. The two point function G_{-+} in momentum space is now obviously proportional to the spectral density:

$$\begin{aligned}
G_{-+}(p) =& \frac{-i}{Z_\beta}\int_{(x-y)} e^{ip(x-y)}\sum_n\sum_m e^{-\beta E_n}e^{ip_n(x-y)}e^{-ip_m(x-y)}\left|\langle f_n\,,\,\phi(0) f_m\rangle\right|^2 \\
=& -i\tilde\rho_{-+}(p)\,.
\end{aligned} \tag{5.5}$$

Clearly, the above derivation can be repeated for G_{+-} just with x and y interchanged and one arrives at

$$\tilde{\rho}_{+-}(p) := \frac{1}{Z_\beta} \sum_n \sum_m e^{-\beta E_n} (2\pi)^4 \delta(-p_n + p_m + p) \, |\langle f_n \, , \, \phi(0) f_m \rangle|^2 \tag{5.6}$$

and

$$G_{+-}(p) = -i \tilde{\rho}_{+-}(p) \, . \tag{5.7}$$

By using the symmetry of the delta function in (5.4), the obvious relation

$$\tilde{\rho}_{+-}(p) = \tilde{\rho}_{-+}(-p) \, . \tag{5.8}$$

is established. Moreover, by relabeling the dummy indices m and n in (5.4), making use of the zero component of the delta function, which is nothing but the energy conservation $E_m - E_n + p^0 = 0$ and using the invariance of the matrix element under interchange of m and n one arrives at

$$\begin{aligned} \tilde{\rho}_{-+}(p) =& \frac{1}{Z_\beta} \sum_m \sum_n e^{-\beta E_m} (2\pi)^4 \delta^{(4)}(p_m - p_n + p) \, |\langle f_m \, , \, \phi(0) f_n \rangle|^2 \\ =& e^{\beta p^0} \tilde{\rho}_{+-}(p) \, . \end{aligned} \tag{5.9}$$

The above equation is nothing but the well-known KMS-condition, which is usually formulated for the two-point functions itself,

$$G_{-+}(p) = e^{\beta p^0} G_{+-}(p) \, , \tag{5.10}$$

and can also be obtained from the periodicity condition in time-direction (recall (4.10)). Note that this holds only in equilibrium, since the perodicity as well as the representation for the correlation functions with the density matrix $e^{-\beta H}$ do not hold in non-equlilibrium. A more convenient quantity than the spectral densities defined above is the standard spectral function $\rho(p)$ known from QFT textbooks, since all components of the propagator matrix G, as well as the retareded and advanced ones can be expressed in terms of this spectral function. Thus, in position space the spectral function

is defined as:

$$\begin{aligned}\rho(x,y) :=& \langle[\phi(x),\phi(y)]\rangle \\ =& \langle\phi(x)\phi(y)\rangle - \langle\phi(y)\phi(x)\rangle \\ =& i\,\left(G_{-+}(x,y) - G_{+-}(x,y)\right) \\ =& \tilde{\rho}_{-+}(x,y) - \tilde{\rho}_{+-}(x,y)\,. \end{aligned} \tag{5.11}$$

In terms of this spectral function the off-diagonal elements of the propagator are given by

$$\begin{aligned} G_{-+}(p) = -i\tilde{\rho}_{-+}(p) =& -i\,\frac{\rho(p)}{1-e^{-\beta p^0}} \\ =& -i\,\frac{\rho(p)\,e^{\beta p^0}}{e^{\beta p^0}-1} && (5.12)\\ =& -i\,\frac{\rho(p)\,\left(e^{\beta p^0}-1+1\right)}{e^{\beta p^0}-1} && (5.13)\\ =& -i\,\left(\rho(p) + \frac{\rho(p)}{e^{\beta p^0}-1}\right) && (5.14)\\ =& -i\,\rho(p)\left(1+n_\beta(p^0)\right)\,, && (5.15)\end{aligned}$$

and similarly

$$G_{+-}(p) = -i\tilde{\rho}_{+-}(p) = -i\,\rho(p)\,n_\beta(p^0) \tag{5.16}$$

with the Bose-Einstein distribution

$$n_\beta(p^0) = \frac{1}{e^{\beta p^0}-1}\,. \tag{5.17}$$

5.1.2 Diagonal elements of the Real-time propagator

The derivation of the diagonal element of the real-time propagator matrix is slightly more demanding. Considering the time-ordered, i.e. Feynman progagator and making the time-ordering explicit one has to deal with

$$G_{++}(x,y) = -i\left(\theta(x^0-y^0)\langle\phi(x)\phi(y)\rangle + \theta(y^0-x^0)\langle\phi(y)\phi(x)\rangle\right)\,, \tag{5.18}$$

with the Heaviside step function θ. The correlation functions appearing in (5.18) were already calculated above. However, the Fourier-transform is now a little more complicated due to the θ functions with pure time-arguments, so that the Fourier

transformations for space arguments $\mathbf{z} := \mathbf{x} - \mathbf{y}$ and time arguments $z^0 := x^0 - y^0$ must be performed seperately. The spectral representation for G_{++} is given by

$$\begin{aligned} G_{++}(p) =& \frac{-i}{Z_\beta} \int_{\mathbf{z}} \int_{z^0} e^{-i\mathbf{pz}} e^{ip^0 z^0} \theta(z^0) \sum_n \sum_m e^{-\beta E_n} e^{ip_n z} e^{-ip_m z} \left| \langle f_n \, , \, \phi(0) f_m \rangle \right|^2 \\ & \frac{-i}{Z_\beta} \int_{\mathbf{z}} \int_{z^0} e^{-i\mathbf{pz}} e^{ip^0 z^0} \theta(-z^0) \sum_n \sum_m e^{-\beta E_n} e^{-ip_n z} e^{+ip_m z} \left| \langle f_n \, , \, \phi(0) f_m \rangle \right|^2 \, . \end{aligned}$$

For further evaluation it is useful to insert the following integral representations for the θ function:

$$\theta(x) = \lim_{\epsilon \to 0} \frac{i}{2\pi} \int_\tau \frac{e^{-ix\tau}}{\tau + i\epsilon} \, , \tag{5.19}$$

and

$$\theta(-x) = \lim_{\epsilon \to 0} \frac{-i}{2\pi} \int_\tau \frac{e^{-ix\tau}}{\tau - i\epsilon} \, , \tag{5.20}$$

taking care of the issue of appropriate $i\epsilon$-prescriptions in the Fourier transforms. Manipulating the first term in the above expression for $G_{++}(p)$, i.e. the term proportional to $\theta(z^0)$, yields

$$\begin{aligned} & \frac{-i}{Z_\beta} \frac{i}{2\pi} \sum_m \sum_n e^{-\beta E_n} \left| \langle f_n \, , \, \phi(0) f_m \rangle \right|^2 \int_{\mathbf{z}} \int_{z^0} e^{iz^0 \left(p^0 + p_n^0 - p_m^0 \right)} e^{-i\mathbf{z}(\mathbf{p} + \mathbf{p_n} - \mathbf{p_m})} \int_{p^{0\prime}} \frac{e^{-iz^0 p^{0\prime}}}{p^{0\prime} + i\epsilon} \\ =& \frac{-i}{Z_\beta} \frac{i}{2\pi} \sum_m \sum_n e^{-\beta E_n} \left| \langle f_n \, , \, \phi(0) f_m \rangle \right|^2 (2\pi)^3 \delta^{(3)} \left(\mathbf{p} + \mathbf{p_n} - \mathbf{p_m} \right) \int_{p^{0\prime}} \frac{1}{p^{0\prime} + i\epsilon} \int_{z^0} e^{iz^0 \left(p^0 - p^{0\prime} + p_n^0 - p_m^0 \right)} \\ =& \frac{-i}{Z_\beta} \frac{i}{2\pi} \sum_m \sum_n e^{-\beta E_n} \left| \langle f_n \, , \, \phi(0) f_m \rangle \right|^2 (2\pi)^3 \delta^{(3)} \left(\mathbf{p} + \mathbf{p_n} - \mathbf{p_m} \right) \int_{p^{0\prime}} \frac{2\pi}{p^{0\prime} + i\epsilon} \delta(p^0 - p^{0\prime} + p_n^0 - p_m^0) \\ =& \frac{-i}{Z_\beta} \frac{i}{2\pi} \sum_m \sum_n e^{-\beta E_n} \left| \langle f_n \, , \, \phi(0) f_m \rangle \right|^2 (2\pi)^3 \delta^{(3)} \left(\mathbf{p} + \mathbf{p_n} - \mathbf{p_m} \right) (2\pi) \frac{1}{p^0 - p_n^0 - p_m^0 + i\epsilon} \, , \end{aligned}$$

where the limit $\epsilon \longrightarrow 0$ is, of course, implicitly understood. Eventually, the aim is to express the above in terms of the spectral function ρ, which contains a four dimensional θ function. Therefore it helps rewrite the above according to

$$\begin{aligned} & \frac{-i}{Z_\beta} \frac{i}{2\pi} \sum_m \sum_n e^{-\beta E_n} \left| \langle f_n \, , \, \phi(0) f_m \rangle \right|^2 (2\pi)^3 \delta^{(3)} \left(\mathbf{p} + \mathbf{p_n} - \mathbf{p_m} \right) \int_{p^{0\prime}} \frac{2\pi}{p^0 - p^{0\prime} + i\epsilon} \delta(p^{0\prime} + p_n^0 - p_m^0) \\ =& \frac{1}{2\pi} \int_{p^{0\prime}} \frac{\tilde{\rho}_{-+}(p^{0\prime}, \mathbf{p})}{p^0 - p^{0\prime} + i\epsilon} \, . \end{aligned} \tag{5.21}$$

The analog steps can be performed for the term proportional to $\theta(-z^0)$, which produces an additional overall minus sign and a minus sign in the $i\epsilon$ prescription due to the

different integral representation of the θ function and interchanges the labels m and n in the delta functions. Obviously this can then be expressed in terms of $\tilde{\rho}_{+-}(p^{0\prime}, p^0)$, leading to

$$G_{++}(p) = \frac{1}{2\pi} \int_{p^{0\prime}} \left(\frac{\tilde{\rho}_{-+}(p^{0\prime}, \mathbf{p})}{p^0 - p^{0\prime} + i\epsilon} - \frac{\tilde{\rho}_{+-}(p^{0\prime}, \mathbf{p})}{p^0 - p^{0\prime} - i\epsilon} \right) .$$

Similar to the off-diagonal elements, two additional representations of the above in terms of the usual spectral function ρ are desired, such that one regains the usual Feynman propagator in the limit $T \longrightarrow 0$. In order to do so, the Sokhotski-Plemelj theorem [161] is employed:

$$\lim_{\epsilon \to 0} \int_x \frac{f(x)}{x - x_0 \pm i\epsilon} = \mp i\pi f(x_0) + \mathcal{P} \int_x \frac{f(x)}{x - x_0} . \tag{5.22}$$

where $\mathcal{P}$ denote the Cauchy principal value. Applying this to the identity (5.22) leads to

$$G_{++}(p) = \frac{1}{2\pi} \mathcal{P} \int_{p^{0\prime}} \left(\frac{\tilde{\rho}_{-+}(p^{0\prime}, \mathbf{p}) - \tilde{\rho}_{+-}(p^{0\prime}, \mathbf{p})}{p^0 - p^{0\prime}} \right) - \frac{1}{2\pi} i\pi \left(\tilde{\rho}_{-+}(p^0, \mathbf{p}) + \tilde{\rho}_{+-}(p^0, \mathbf{p}) \right) .$$

Using the KMS condition for the spectral densities and the definition $\rho = \tilde{\rho}_{-+} - \tilde{\rho}_{+-}$, yields the relation

$$\begin{aligned} \frac{1}{2\pi} i\pi \left(\tilde{\rho}_{-+}(p^0, \mathbf{p}) + \tilde{\rho}_{+-}(p^0, \mathbf{p}) \right) &= \frac{1}{2\pi} i\pi \left(\rho(p^0, \mathbf{p}) + 2\tilde{\rho}_{+-}(p^0, \mathbf{p}) \right) \\ &= \frac{1}{2\pi} i\pi \left(\rho(p^0, \mathbf{p}) + 2n_\beta(p^0)\rho(p^0, \mathbf{p}) \right) \qquad (5.23) \\ &= i\rho(p^0, \mathbf{p}) \left(\frac{1}{2} + n_\beta(p^0) \right) , \qquad (5.24) \end{aligned}$$

and therefore

$$G_{++}(p) = \frac{1}{2\pi} \mathcal{P} \int_{p^{0\prime}} \left(\frac{\rho(p^{0\prime}, \mathbf{p})}{p^0 - p^{0\prime}} \right) - i\rho(p^0, \mathbf{p}) \left(\frac{1}{2} + n_\beta(p^0) \right) . \tag{5.25}$$

In addition, this representation can be rewritten, such that the zero-temperature Feynman propagator appears, and that one gets back the zero-temperature spectral representation of the time-ordered propagator. In order to achieve this, the Sokhotski-Plemelj theorem (5.22) is employed once more, and principal value is rewritten again

with an $i\epsilon$- prescription. Here, only the part with the principal value is considered :

$$\frac{1}{2\pi}\mathcal{P}\int_{-\infty}^{\infty}\mathrm{d}p^{0\prime}\left(\frac{\rho(p^{0\prime},\mathbf{p})}{p^0-p^{0\prime}}\right)=\frac{1}{2\pi}\int_{-\infty}^{\infty}\mathrm{d}p^{0\prime}\left(\frac{\rho(p^{0\prime},\mathbf{p})}{p^0-p^{0\prime}+i\epsilon}\right)+\frac{1}{2\pi}i\pi\rho(p^0,\mathbf{p})\,.$$

Together with (5.25) the intermediate result is

$$G_{++}(p)=\frac{1}{2\pi}\int_{-\infty}^{\infty}\mathrm{d}p^{0\prime}\left(\frac{\rho(p^{0\prime},\mathbf{p})}{p^0-p^{0\prime}+i\epsilon}\right)-in_\beta(p^0)\rho(p^0,\mathbf{p})\,, \tag{5.26}$$

which is also quite frequently used in the literature, and maybe the most convenient one. However, proceeding with bringing the above into the analog of the well-known zero-temperature form of the spectral respresentation of the time-ordered propagator is also useful. Now, only the the $i\epsilon$ part is considered:

$$\begin{aligned}
G_{++}(p)=&\frac{1}{2\pi}\int_{-\infty}^{\infty}\mathrm{d}p^{0\prime}\left(\frac{\rho(p^{0\prime},\mathbf{p})}{p^0-p^{0\prime}+i\epsilon}\right)-in_\beta(p^0)\rho(p^0,\mathbf{p})\\
=&\frac{1}{2\pi}\int_{-\infty}^{\infty}\mathrm{d}p^{0\prime}\left(\frac{p^0+p^{0\prime}-i\epsilon}{\left(p^0-\left(p^{0\prime}-i\epsilon\right)\right)\left(p^0+\left(p^{0\prime}-i\epsilon\right)\right)}\right)\rho(p^{0\prime},\mathbf{p})-in_\beta(p^0)\rho(p^0,\mathbf{p})\\
=&\frac{1}{2\pi}\int_{-\infty}^{\infty}\mathrm{d}p^{0\prime}\left(\frac{p^0+p^{0\prime}-i\epsilon}{\left(p^0\right)^2-\left(p^{0\prime}-i\epsilon\right)^2}\right)\rho(p^{0\prime},\mathbf{p})-in_\beta(p^0)\rho(p^0,\mathbf{p})\\
=&\frac{1}{2\pi}\int_{-\infty}^{\infty}\mathrm{d}p^{0\prime}\left(\frac{p^0+p^{0\prime}-i\epsilon}{\left(p^0\right)^2-\left(p^{0\prime}\right)^2+2p^{0\prime}i\epsilon-i^2\epsilon^2}\right)\rho(p^{0\prime},\mathbf{p})-in_\beta(p^0)\rho(p^0,\mathbf{p})
\end{aligned} \tag{5.27}$$

Now one can use that the limit $\epsilon\longrightarrow 0$ is implicitly understood and that the $i\epsilon$ in the numerator does not change the value of the integral, since it is not connected to any pole description, i.e. there is no principle value description necessary. Hence it can be dropped. Morevover, the term of order ϵ^2 in the denominator is subleading and can be dropped as well. Furthermore, it helps to rewrite the integral as an integral over $\left(p^{0\prime}\right)^2$ instead of $p^{0\prime}$. This transformation, however, is diffeomorphic only on the negative and

the positve branch separately. Therefore,first, one needs to rewrite the above as

$$\frac{1}{2\pi}\int_{-\infty}^{\infty}\mathrm{d}p^{0\prime}\left(\frac{p^0+p^{0\prime}}{\left(p^0\right)^2-\left(p^{0\prime}\right)^2+2p^{0\prime}i\epsilon}\right)\rho(p^{0\prime},\mathbf{p})-in_\beta(p^0)\rho(p^0,\mathbf{p})$$

$$=\frac{1}{2\pi}\int_{-\infty}^{0}\mathrm{d}p^{0\prime}\left(\frac{p^0+p^{0\prime}}{\left(p^0\right)^2-\left(p^{0\prime}\right)^2+2p^{0\prime}i\epsilon}\right)\rho(p^{0\prime},\mathbf{p}) \tag{5.28}$$

$$+\frac{1}{2\pi}\int_{0}^{\infty}\mathrm{d}p^{0\prime}\left(\frac{p^0+p^{0\prime}}{\left(p^0\right)^2-\left(p^{0\prime}\right)^2+2p^{0\prime}i\epsilon}\right)\rho(p^{0\prime},\mathbf{p})-in_\beta(p^0)\rho(p^0,\mathbf{p})\,. \tag{5.29}$$

Substituting the integration variable $p^{0\prime}$ in the integrals that range from $-\infty$ to 0 by $-p^{0\prime}$ and using $\rho(-p^0) = -\rho(p^0)$, leads to

$$
\begin{aligned}
&= -\frac{1}{2\pi}\int_{\infty}^{0} \mathrm{d}p^{0\prime}\left(\frac{p^0}{(p^0)^2-\left(p^{0\prime}\right)^2-2p^{0\prime}i\epsilon}\right)\rho(-p^{0\prime},\mathbf{p}) && (5.30)\\
&\quad+\frac{1}{2\pi}\int_{0}^{\infty} \mathrm{d}p^{0\prime}\left(\frac{p^0}{(p^0)^2-\left(p^{0\prime}\right)^2+2p^{0\prime}i\epsilon}\right)\rho(p^{0\prime},\mathbf{p}) && (5.31)\\
&\quad+\frac{1}{2\pi}\int_{\infty}^{0} \mathrm{d}p^{0\prime}\left(\frac{p^{0\prime}}{(p^0)^2-\left(p^{0\prime}\right)^2-2p^{0\prime}i\epsilon}\right)\rho(-p^{0\prime},\mathbf{p})\\
&\quad+\frac{1}{2\pi}\int_{0}^{\infty} \mathrm{d}p^{0\prime}\left(\frac{p^{0\prime}}{(p^0)^2-\left(p^{0\prime}\right)^2+2p^{0\prime}i\epsilon}\right)\rho(p^{0\prime},\mathbf{p}) - in_\beta(p^0)\rho(p^0,\mathbf{p}) && (5.32)\\
&= -\frac{1}{2\pi}\int_{0}^{\infty} \mathrm{d}p^{0\prime}\left(\frac{p^0}{(p^0)^2-\left(p^{0\prime}\right)^2-2p^{0\prime}i\epsilon}\right)\rho(p^{0\prime},\mathbf{p})\\
&\quad+\frac{1}{2\pi}\int_{0}^{\infty} \mathrm{d}p^{0\prime}\left(\frac{p^0}{(p^0)^2-\left(p^{0\prime}\right)^2+2p^{0\prime}i\epsilon}\right)\rho(p^{0\prime},\mathbf{p}) && (5.33)\\
&\quad+\frac{1}{2\pi}\int_{0}^{\infty} \mathrm{d}p^{0\prime}\left(\frac{p^{0\prime}}{(p^0)^2-\left(p^{0\prime}\right)^2-2p^{0\prime}i\epsilon}\right)\rho(p^{0\prime},\mathbf{p})\\
&\quad+\frac{1}{2\pi}\int_{0}^{\infty} \mathrm{d}p^{0\prime}\left(\frac{p^{0\prime}}{(p^0)^2-\left(p^{0\prime}\right)^2+2p^{0\prime}i\epsilon}\right)\rho(p^{0\prime},\mathbf{p}) - in_\beta(p^0)\rho(p^0,\mathbf{p}) && (5.34)\\
&= -\frac{1}{2\pi}\int_{0}^{\infty} \mathrm{d}p^{0\prime}\left(\frac{p^0}{(p^0)^2-\left(p^{0\prime}\right)^2-i\epsilon}\right)\rho(p^{0\prime},\mathbf{p}) && (5.35)\\
&\quad+\frac{1}{2\pi}\int_{0}^{\infty} \mathrm{d}p^{0\prime}\left(\frac{p^0}{(p^0)^2-\left(p^{0\prime}\right)^2+i\epsilon}\right)\rho(p^{0\prime},\mathbf{p}) && (5.36)\\
&\quad+\frac{1}{2\pi}\int_{0}^{\infty} \mathrm{d}p^{0\prime}\left(\frac{p^{0\prime}}{(p^0)^2-\left(p^{0\prime}\right)^2-i\epsilon}\right)\rho(p^{0\prime},\mathbf{p})\\
&\quad+\frac{1}{2\pi}\int_{0}^{\infty} \mathrm{d}p^{0\prime}\left(\frac{p^{0\prime}}{(p^0)^2-\left(p^{0\prime}\right)^2+i\epsilon}\right)\rho(p^{0\prime},\mathbf{p}) - in_\beta(p^0)\rho(p^0,\mathbf{p})\,, && (5.37)
\end{aligned}
$$

where the $2p^{0\prime}$ were dropped in the $i\epsilon$ parts in the last step since now all integrals are performed over an interval with $p^{0\prime} > 0$ and the sign of the $i\epsilon$ terms is therefore fixed. In the expressions above, integral transformation

$$
u\ : p^{0\prime}\ \longrightarrow\ u\left(p^{0\prime}\right) = \left(p^{0\prime}\right)^2\ , \tag{5.38}
$$

can be applied, which is now a diffeomorphism. The measure transforms as

$$\mathrm{d}p^{0\prime} = \frac{\mathrm{d}u}{2p^{0\prime}}\,, \tag{5.39}$$

and one arrives at

$$\begin{aligned} G_{++}(p) = &-\frac{1}{2\pi}\frac{1}{2}\int_0^\infty \mathrm{d}u \left(\frac{p^0}{\sqrt{u}}\frac{\rho(\sqrt{u},\mathbf{p})}{\left(p^0\right)^2 - u - i\epsilon}\right) + \frac{1}{2\pi}\frac{1}{2}\int_0^\infty \mathrm{d}u \left(\frac{p^0}{\sqrt{u}}\frac{\rho(\sqrt{u},\mathbf{p})}{\left(p^0\right)^2 - u + i\epsilon}\right) \\ &+\frac{1}{2\pi}\frac{1}{2}\int_0^\infty \mathrm{d}u \left(\frac{\rho(\sqrt{u},\mathbf{p})}{\left(p^0\right)^2 - u - i\epsilon}\right) + \frac{1}{2\pi}\frac{1}{2}\int_0^\infty \mathrm{d}u \left(\frac{\rho(\sqrt{u},\mathbf{p})}{\left(p^0\right)^2 - u + i\epsilon}\right) - in_\beta(p^0)\rho(p^0,\mathbf{p})\,. \end{aligned} \tag{5.40}$$

In addition to the integration over $\left(p^{0\prime}\right)^2$ and the squares in the denominator, which are already present in the equation above, eventually a representation entirely based on the Feynman $+i\epsilon$ description is desired. Once more the Sokhtsky Plemely theorem [161] is employed to rewrite the above in the desired way. Note that the principal value parts in the terms proportional to p^0 cancel each other, and therefore these terms contribute only terms with delta functions. This is expected, since if one had dropped the $i\epsilon p^{0\prime}$ terms in the denominator in (5.27), i.e. if one had a standard principal value, this principal value would be zero in the first place since there the integration is performed over a symmetric interval while the spectral function is antisymmetric and all other terms are symmetric. Hence, this cancellation of the principal values is just a manifestation of this fact and one is left with "pole-contributions" of these terms only. In summary, the

(5.40) is manipulated according to

$$
\begin{aligned}
G_{++}(p) = &-\frac{1}{2\pi}\frac{1}{2}i\pi\int_0^\infty \mathrm{d}u\,\rho(\sqrt{u},\mathbf{p})\frac{p^0}{\sqrt{u}}\,\delta\left(u-\left(p^0\right)^2\right)\\
&-\frac{1}{2\pi}\frac{1}{2}i\pi\int_0^\infty \mathrm{d}u\,\rho(\sqrt{u},\mathbf{p})\frac{p^0}{\sqrt{u}}\,\delta\left(u-\left(p^0\right)^2\right)+\frac{1}{2\pi}\frac{1}{2}\,\mathcal{PV}\int_0^\infty \mathrm{d}u\,\frac{\rho(\sqrt{u},\mathbf{p})}{\left(p^0\right)^2-u}\\
&+\frac{1}{2\pi}\frac{1}{2}i\pi\int_0^\infty \mathrm{d}u\,\rho(\sqrt{u},\mathbf{p})\,\delta\left(u-\left(p^0\right)^2\right)+\frac{1}{2\pi}\frac{1}{2}\int_0^\infty \mathrm{d}u\frac{\rho(\sqrt{u},\mathbf{p})}{\left(p^0\right)^2-u+i\epsilon}-in_\beta(p^0)\rho(p^0,\mathbf{p})\\
= &-\frac{1}{2\pi}\frac{1}{2}i\pi\int_0^\infty \mathrm{d}u\,\rho(\sqrt{u},\mathbf{p})\frac{p^0}{\sqrt{u}}\,\delta\left(u-\left(p^0\right)^2\right)\\
&-\frac{1}{2\pi}\frac{1}{2}i\pi\int_0^\infty \mathrm{d}u\,\rho(\sqrt{u},\mathbf{p})\frac{p^0}{\sqrt{u}}\,\delta\left(u-\left(p^0\right)^2\right)+\frac{1}{2\pi}\frac{1}{2}\int_0^\infty \mathrm{d}u\frac{\rho(\sqrt{u},\mathbf{p})}{\left(p^0\right)^2-u+i\epsilon}\\
&+\frac{1}{2\pi}\frac{1}{2}i\pi\int_0^\infty \mathrm{d}u\,\rho(\sqrt{u},\mathbf{p})\,\delta\left(u-\left(p^0\right)^2\right)+\frac{1}{2\pi}\frac{1}{2}i\pi\int_0^\infty \mathrm{d}u\,\rho(\sqrt{u},\mathbf{p})\,\delta\left(u-\left(p^0\right)^2\right)\\
&+\frac{1}{2\pi}\frac{1}{2}\int_0^\infty \mathrm{d}u\frac{\rho(\sqrt{u},\mathbf{p})}{\left(p^0\right)^2-u+i\epsilon}-in_\beta(p^0)\rho(p^0,\mathbf{p})\\
= &-\frac{i}{2}\int_0^\infty \mathrm{d}u\,\rho(\sqrt{u},\mathbf{p})\frac{p^0}{\sqrt{u}}\,\delta\left(u-\left(p^0\right)^2\right)+\frac{i}{2}\int_0^\infty \mathrm{d}u\,\rho(\sqrt{u},\mathbf{p})\,\delta\left(u-\left(p^0\right)^2\right)\\
&+\frac{1}{2\pi}\int_0^\infty \mathrm{d}u\,\frac{\rho(\sqrt{u},\mathbf{p})}{\left(p^0\right)^2-u+i\epsilon}-in_\beta(p^0)\rho(p^0,\mathbf{p})\,. \qquad (5.41)
\end{aligned}
$$

The delta-functions are not carried out yet, since they contain a little subtlety. For the following analysis, it is more convenient to use $u=\left(p^{0\prime}\right)^2$. Before the integral transformation was introduced, the $p^{0\prime}$-integrals were along the positive real line, $p^{0\prime}>0$. The delta functions contain the squares, $\delta\left(\left(p^{0\prime}\right)^2-\left(p^0\right)^2\right)$, but the argument of the spectral function ρ is without the square, i.e. $\rho(p^{0\prime},\mathbf{p})$. Since $p^{0\prime}>0$, the delta functions enforce

$$
p^0=p^{0\prime}>0 \qquad \text{or} \qquad p^0=-p^{0\prime}<0\,. \qquad (5.42)
$$

First, let us consider $p^0>0,\Longleftrightarrow p^0=p^{0\prime}$:
In this case, obviously

$$
\frac{p^0}{\sqrt{u}}=\frac{p^0}{p^{0\prime}}=1\,, \qquad (5.43)
$$

and the two terms in the first line after the last equality sign in (5.41) cancel, and one is left with the last line.
Considering $p^0<0,\Longleftrightarrow p^0=-p^{0\prime}$, the above fraction is -1 and the two terms do not cancel, but are equal. Considering the two terms together with the last, one finds for

the $p^0 = -p^{0\prime}$ case in the delta function

$$
\begin{aligned}
&-\frac{i}{2}\int_0^\infty \mathrm{d}u\,\rho(\sqrt{u},\mathbf{p})\frac{p^0}{\sqrt{u}}\,\delta\left(u-\left(p^0\right)^2\right)+\frac{i}{2}\int_0^\infty \mathrm{d}u\,\rho(\sqrt{u},\mathbf{p})\,\delta\left(u-\left(p^0\right)^2\right)-in_\beta(p^0)\rho(p^0,\mathbf{p})\\
&=i\rho(-p^0,\mathbf{p})-in_\beta(p^0)\rho(p^0,\mathbf{p})\\
&=-i\rho(p^0,\mathbf{p})-in_\beta(p^0)\rho(p^0,\mathbf{p})=in_\beta(-p^0)\rho(p^0,\mathbf{p})=in_\beta\left(\left|p^0\right|\right)\rho(p^0,\mathbf{p})\,,
\end{aligned}
\tag{5.44}
$$

where the last equality is true since $p^0 < 0$. Therefore, the final result is:

$$
G_{++}(p)=\frac{1}{2\pi}\int_0^\infty \mathrm{d}\left(p^{0\prime}\right)^2\frac{1}{\left(p^0\right)^2-\left(p^{0\prime}\right)^2+i\epsilon}\rho(p^{0\prime},\mathbf{p})-i\,\mathrm{sgn}(p^0)\,n_\beta\left(\left|p^0\right|\right)\rho(p^0,\mathbf{p})\,.
\tag{5.45}
$$

In the limit $T \longrightarrow 0$ the distribution function $n_\beta(p^0)$ becomes zero and one obtains the usual spectral representation in zero-temperature QFT. The above can be evaluated for the case of a free massive scalar field, where the spectral function is just given by

$$
\rho_{\text{free}}(p^2)=2\pi\,\mathrm{sgn}(p^0)\,\delta\left(p^2-m^2\right)=2\pi\,\mathrm{sgn}(p^0)\,\delta\left(\left(p^0\right)^2-\mathbf{p}^2-m^2\right)\,,
\tag{5.46}
$$

yielding

$$
G_{++,\text{free}}(p)=\frac{1}{p^2-m^2+i\epsilon}-2\pi i\,\delta\left(p^2-m^2\right)n_\beta\left(\left|p^0\right|\right)\,,
\tag{5.47}
$$

which is exactly the result given e.g. in [154]. In the limit $T \longrightarrow 0$ also yields the standard Feynman propagator in $T = 0$ perturbative QFT.

Note that usually the Feynman propagator is defined just as the correlation function $\langle T\phi(x)\phi(y)\rangle$, and the free propagator is then i times the above result, while here was calculated $-i\,\langle T\phi(x)\phi(y)\rangle$. So by multiplying the conventional result with the i in the numerator by $-i$, the above result is reproduced, constituting a consistency check that all signs and factors of i seem to be correct. The convention used here is equivalent of the one in [154], but differs from the one in [155].

The spectral representation for $G_{--}(p)$ can be obtained analog to the above derivation, just with the role of the θ functions interchanged due to anti-time ordering instead of time-ordering. Repeating the derivation, shows that the thermal part remains unchanged, while the principle value part gets an additional minus sign compared to (5.25), and, if written with an $i\epsilon$ prescription, the sign changes compared to (5.26).

Therefore

$$\begin{aligned} G_{--}(p) =& -\frac{1}{2\pi}\mathcal{PV}\int_{p^{0\prime}}\left(\frac{\rho(p^{0\prime},\mathbf{p})}{p^0-p^{0\prime}}\right) - i\rho(p^0,\mathbf{p})\left(\frac{1}{2}+n_\beta(p^0)\right) \\ =& -\frac{1}{2\pi}\int_{-\infty}^{\infty}\mathrm{d}p^{0\prime}\left(\frac{\rho(p^{0\prime},\mathbf{p})}{p^0-p^{0\prime}-i\epsilon}\right) - in_\beta(p^0)\rho(p^0,\mathbf{p})\,. \end{aligned} \tag{5.48}$$

5.1.3 Retarded and advanced propagators

To conclude the derivation, the representations for the retarded an advanced propagators are considered. These are defined as

$$G_R(x,y) = G_{++}(x,y) - G_{+-}(x,y)\,, \tag{5.49}$$

and

$$G_A(x,y) = G_{++}(x,y) - G_{-+}(x,y)\,. \tag{5.50}$$

With the expressions derived above, both retarded and advanced propagator yield:

$$G_R(p) = \frac{1}{2\pi}\int_{-\infty}^{\infty}\mathrm{d}p^{0\prime}\left(\frac{\rho(p^{0\prime},\mathbf{p})}{p^0-p^{0\prime}+i\epsilon}\right) = \frac{1}{2\pi}\mathcal{PV}\int_{-\infty}^{\infty}\mathrm{d}p^{0\prime}\left(\frac{\rho(p^{0\prime},\mathbf{p})}{p^0-p^{0\prime}}\right) - \frac{1}{2}i\,\rho(p^0,\mathbf{p})\,, \tag{5.51}$$

and

$$\begin{aligned} G_A(p) =& \frac{1}{2\pi}\int_{-\infty}^{\infty}\mathrm{d}p^{0\prime}\left(\frac{\rho(p^{0\prime},\mathbf{p})}{p^0-p^{0\prime}+i\epsilon}\right) + i\,\rho(p^0,\mathbf{p}) \\ =& \frac{1}{2\pi}\mathcal{PV}\int_{-\infty}^{\infty}\mathrm{d}p^{0\prime}\left(\frac{\rho(p^{0\prime},\mathbf{p})}{p^0-p^{0\prime}}\right) + \frac{1}{2}i\,\rho(p^0,\mathbf{p}) \end{aligned} \tag{5.52}$$

Note that there are no thermal distributions functions in the retarded or advanced propagator, and therefore the free causal propagators $G_{R,\mathrm{free}}$ and $G_{A,\mathrm{free}}$ are temperature independent, since the free spectral functions has this property. The full retarded and advanced propagtors get of course a temperature dependence from the full spectral function. From the spectral representation (5.51) of the retarded propagator it is obvious that

$$\rho(p^0,\mathbf{p}) = -2\,\mathrm{Im}G_R\,. \tag{5.53}$$

5.2 Spectral representation in the imaginary-time formalism

The derivation of the spectral representation in the imaginary time formalism is now straight forward. The euclidean (Matsubara) correlation function is obtained by Wick rotation from the retarded Greens function:

$$G_E(p^0, \mathbf{p}) = \mathbf{G_R}(\mathbf{i}\,\mathbf{p^0} - \mathbf{i}\,\epsilon) \tag{5.54}$$

Inserting the first representation of (5.51) immediately yields:

$$G_E(p^0, \mathbf{p}) = \int_{\infty}^{\infty} \frac{\mathrm{d}\mathbf{p^{0\prime}}}{\mathbf{2}\pi} \frac{\rho(\mathbf{p^{0\prime}}, \mathbf{p})}{\mathbf{i}\,\mathbf{p^0} - \mathbf{p^{0\prime}}} \tag{5.55}$$

Note, that according to (4.20) the Matsubara correlation function is relevant only at the discrete set of Matsubara frequencies.
For future use in the Maximum Entropy Method, the mixed representation $G(\tau, \mathbf{p}))$ is derived, by partially Fourier transforming (5.55) with respect to the zero-component.

$$G(\tau, \mathbf{p}) = \frac{1}{\beta} \sum_n e^{-i\,\omega_n \tau} G(\omega_n, \mathbf{p}) \tag{5.56}$$

$$= \frac{1}{\beta} \sum_n e^{-i\,\omega_n \tau} \int_{\infty}^{\infty} \frac{\mathrm{d}\omega'}{2\pi} \frac{\rho(\omega', \mathbf{p})}{i\,\omega - \omega'} \tag{5.57}$$

$$= \frac{1}{\beta} \int_{\infty}^{\infty} \frac{\mathrm{d}\omega'}{2\pi} \rho(\omega', \mathbf{p}) \sum_n e^{-i\,\omega_n \tau} \frac{1}{i\,\omega - \omega'} \tag{5.58}$$

The Matsubara summation can be carried out by the following trick: Consider an analytic function $f(z)$ for $z \in \mathbb{C} \setminus \{i\omega_n\}$ that has first order poles at $z = i\omega_n$. Then the Matsubara sum for a function $g(i\omega_n)$ can be written as:

$$\sum g(i\,\omega_n) = \frac{1}{2\pi i} \oint g(z) f(z) \mathrm{d}z \tag{5.59}$$

where the contour is made out of circles around the Matsubara frequencies. These circles can be topologically deformed, such that the contour integration is given by

(see. e.g. [155]):

$$\frac{1}{2\pi i}\oint g(z)f(z)\mathrm{d}z = \sum_{z\in\text{Poles of } g(z)} \operatorname{Res} g(z)f(z) \tag{5.60}$$

A common choice for $f(z)$ is:

$$f(z) = \beta n_\beta(z) \tag{5.61}$$

in terms of the Bose distribution function $n_\beta(z)$ at temperature $\frac{1}{\beta}$ for convergence in $Re(z) > 0$ and

$$f(z) = \beta(1 + n_\beta(z)) \tag{5.62}$$

for convergence in $Re(z) < 0$. For the case of (5.56) the only (relevant) pole is at $z = \omega$. Thus, the integral must be divided into positive and negative frequency part. The result after evaluating the Matsubara sum, i.e. after setting $z = \omega$ in all expressions:

$$G(\tau, \mathbf{p}) = \int_{\mathbf{0}}^{\infty} \frac{\mathrm{d}\omega}{\mathbf{2}\pi}\rho(\omega, \mathbf{p})(\mathbf{1} + \mathbf{n}(\omega))\mathbf{e}^{\omega\tau} + \mathbf{n}(\omega)\mathbf{e}^{-\omega\tau} \tag{5.63}$$

6 Diagrammatics

'Es kommt nicht darauf an, mit dem Kopf durch die Wand zu rennen, sondern mit den Augen die Tür zu finden.'
Werner von Siemens

In this chapter a diagrammatic expansion of the spectral function of the energy-momentum tensor correlation function in terms of spectral functions of the fundamental fields is derived. The central tool is the magic formula, which yields general correlation functions in terms of propagators and field derivatives. With some calculational effort it can be applied for the Greens functions in the real-time formalism. It then becomes obvious, that the expansion consists of a finite number of diagrams in full propagators.

6.1 The magic formula

Consider a field theory with fundamental fields $\varphi_a \, (a = 1, .., N)$, corresponding sources J^a and expectation values $\phi_a \equiv \langle \varphi_a \rangle$. Further, consider a composite operator $\Phi_{\vec{b}}[\phi_a]$ with some given index structure $\vec{b}$. Then, the expectation value with respect to the sources $\vec{J} = (J^1, ..., J^N)$ is

$$\bar{\Phi}_{\vec{b}} = \langle \Phi_{\vec{b}}[\phi_a] \rangle_{\vec{J}} = \Phi_{\vec{a}}[G_{\varphi_a \varphi_b} \frac{\delta}{\delta \varphi_b} + \phi_a] \tag{6.1}$$

with the relation

$$\frac{\delta}{\delta J^a} = G_{\varphi_a \varphi_b} \frac{\delta}{\delta \varphi_b} \tag{6.2}$$

The magic formula (6.1) is thouroughly derived in [74]. In particular, relation (6.1) allows to break down the correlation functions of the spatial traceless part of the energy-momentum tensor defined in (3.20) to full propagators of the gluon and ghost fields, by setting

$$\Phi_{ij,ij} \left[\hat{A} \right] = \pi_{ij}[\hat{A}] \pi_{ij}[\hat{A}] \tag{6.3}$$

where the hats denote the expectation values of the fluctuation field A. The magic formula yields

$$\langle \pi_{ij}[\hat{A}]\pi_{ij}[\hat{A}]\rangle = \pi_{ij}[G_{A\varphi_a}\cdot\frac{\delta}{\delta\varphi_a}+A]\,\pi_{ij}[G_{A\varphi_a}\cdot\frac{\delta}{\delta\varphi_a}+A]\,, \tag{6.4}$$

where $\vec{\varphi}=(A,C,\bar{C})$. In particular, the classical (traceless part of the) of the energy-momentum tensor is employed in momentum space

$$\pi_{ij}(p) = (F^a_{\mu i} * F^{a\,\mu}_{\ j})(p) - \frac{1}{3}\delta_{ij}(F^a_{\mu k} * F^{a\,\mu k})(p) \tag{6.5}$$

in terms of the Fourier transform of the field strength tensor (2.16). Here, $(\cdot * \cdot)$ denotes the convolution

$$(f*g)(p) = \int \frac{d^4q}{(2\pi)^4} f(q)g(p-q) \tag{6.6}$$

Note, the convention in (6.5) to use latin letters for three dimensional and color indices and greek letters for four dimensional indices. It is obvious, that (6.5) is indeed traceless.

π_{ij} can be decomposed into three classes, given by the number of gluon fields attached to the EMT-vertex, depending on whether the the abelian part (with 1 gluon field) or the non-abelian part (with 2 gluon fields) of the field-stength tensor is picked. If both abelian parts are chosen, the EMT-vertex has two leg, if both non-abelian parts are picked four legs are outgoing, and for the mix of abelian part and non-abelian part an EMT with three legs is obtained. It is convenient to seperate the generic diagrammatic part from the EMT-specific tensor structure:

$$\pi_{ij} = \alpha^{(2)\,\vec{c}}_{ij,\vec{\mu},}(p,\vec{k})\,A^{(2)\,\vec{c}\vec{\mu}}(\vec{k}) + \alpha^{(3)\,\vec{c}}_{ij,\vec{\mu},}(p,\vec{k})\,A^{(3)\,\vec{c}\vec{\mu}}(\vec{k}) + \alpha^{(4)\,\vec{c}}_{ij,\vec{\mu},}(p,\vec{k})\,A^{(4)\,\vec{c}\vec{\mu}}(\vec{k}) \tag{6.7}$$

where the $\alpha^{(n)}$'s contain the tensor structure and $A^{(n)}$ denotes the n gluon fields, in the sense that:

$$A^{(n)\,\vec{c}\vec{\mu}}(\vec{k}) = A^{c_1,\mu_1}(k_1)...A^{c_n,\mu_n}(k_n) \tag{6.8}$$

Further, in a slight abuse of notation vectors for Lorentz indices, color indices and momenta of length n are introduced, such that i.e.

$$\alpha^{(2)\,\vec{c}}_{ij,\vec{\mu},}(p,\vec{k}) = \alpha^{(2)\,c_1,c_2}_{ij,\mu_1,\mu_2}(p,k_1,k_2) \tag{6.9}$$

In addition to the usual Einstein summation rule, integration of the k_i-momenta is implied in (6.7). The $\alpha' s$ are calculated as the Taylor coefficients of (6.5) about $A = 0$. Below, the explicit expressions are given:

$$\alpha^{(2)\,c_1,c_2}_{ij,\mu_1,\mu_2}(p,k_1,k_2) = -\delta^{c_1c_2}\delta(q-k_1)\delta(p-q-k_2) \tag{6.10}$$
$$\times[\delta^{\mu\nu}(q_i(p_j-q_j)) + q\cdot(p-q)(\delta_{i\mu_1}\delta_{j\mu_2}) \tag{6.11}$$
$$-q_i(p_{\mu_1} - (q_{\mu_1})\delta_{j\mu_2} + q_{\mu_2}(p_i-q_i)\delta_{j\mu_1})] \tag{6.12}$$
$$+i \longleftrightarrow j, (\mu_n, c_n, k_n) \text{ sym., subtract trace} \tag{6.13}$$

$$\alpha^{(3)\,c_1,c_2,c_3}_{ij,\mu_1,\mu_2,\mu_3}(p,k_1,k_2,k_3) = i\,g f^{c_1,c_2,c_3}\delta(q-k_1)\delta(p-q-k_2-k_3)\delta_{j\mu_3}(q_{\mu_2}\delta_{i\mu_1} - q_i\delta_{\mu_1\mu_2}) \tag{6.14}$$
$$+i \longleftrightarrow j, (\mu_n, c_n, k_n) \text{ sym., subtract trace} \tag{6.15}$$

$$\alpha^{(4)\,c_1,c_2,c_3,c_4}_{ij,\mu_1,\mu_2,\mu_3,\mu_4}(p,k_1,k_2,k_3,k_4) = g^2 f^{ac_1c_2}f^{ac_3,c_4}\delta(q-k_1-k_2)\delta(p-q-k_3-k_4) \tag{6.16}$$
$$+i \longleftrightarrow j, (\mu_n, c_n, k_n) \text{ sym., subtract trace} \tag{6.17}$$

In each expression, the convolution integration variable is denoted by q and as above integration is implied. All other appearing convolutions are already carried out. Further, the adequate symmetrization for the $\alpha' s$ as Taylor coefficients is achieved, by adding up all permutations of the triples (μ_n, c_n, k_n). The trace is subtracted symmetrically from each diagonal element.

For the tensor structure of the EMT correlation function, each combination of pairs of $\alpha' s$ are multiplied. Such a term is labelled by

$$\alpha^{(n,m)\ \vec{c}=\vec{c_1}\frown\vec{c_2}}_{\vec{\mu}=\vec{\mu_1}\frown\vec{\mu_2}}(\vec{k}=\vec{k_1}\frown\vec{k_2}) \equiv \alpha^{(n)\,\vec{c}_1}_{ij,\vec{\mu}_1,}(p,\vec{k}_1)\otimes\alpha^{(m),\vec{c}_2}_{ij,\vec{\mu}_2,}(p,\vec{k}_2) \tag{6.18}$$

where $\vec{v} = \vec{v_1}\frown\vec{v_2}$ denotes the concatenation of vectors $\vec{v_1} = (v_1^1,..,v_1^n)$ and $\vec{v_1} = (v_2^1,...,v_2^m)$ to the vector $\vec{v} = (v_1^1,...,v_1^n,v_2^1,...,v_2^m)$.
The expressions for $\alpha^{(n,m)\ \vec{c}}_{\vec{\mu}}(\vec{k})$ are too lengthy to be given explicitly. Note, however, that there is no more dependence on i, j.

Let us now turn to the diagram part, and study the different diagram types sorted by the number of loops.

6.2 Notation and classification

Note, that the classical tensor structure of the energy-momentum tensor is considered. Thus, ghost propagators, in this approximation cannot be connected directly to the EMT-vertices. In particular, there is no term in the magic formula, giving rise to ghost contributions up to 2-loop order.

First, the notation is made explicit. For sake of convenience the hat is dropped for the field expecation values. Gluon propagators in momentum space are denoted by

$$G_{\mu\nu}^{\epsilon_1,\epsilon_2,c_1,c_2}(q_1,q_2) = \delta^{c_1,c_2}\delta^{(4)}(q_1+q_2)G_{\mu\nu}^{\epsilon_1,\epsilon_2}(q_1) \tag{6.19}$$

with the branch indices $\epsilon_1, \epsilon_2 \in \{+,-\}$. The field derivatives in (6.1) act on fields, propagators and Yang-Mills vertices according to

$$\tfrac{\delta}{\delta A^{\epsilon_1,c_1\mu_1}(q_1)} A_{\mu_2}^{\epsilon_2,c_1}(q_2) = \delta^{c_1c_2}\delta^{\epsilon_1\epsilon_2}\delta_{\mu_1\mu_2}\delta^{(4)}(q_1-q_2) \tag{6.20}$$

$$\tfrac{\delta}{\delta A_\mu^{\epsilon,c}(q)} G_{\mu_1\mu_2}^{\epsilon_1,\epsilon_2,c_1,c_2}(q_1,q_2) = -G_{\mu_1\nu_1}^{\epsilon_1,\epsilon,c_1\tilde{c_1}}(q_1,r)\Gamma^{\epsilon,\nu_1\mu\nu_2,\tilde{c_1},c,\tilde{c_2}}(r,q,s)G_{\nu_2\mu_2}^{\epsilon,\epsilon_2,\tilde{c_2}c_2}(s,q_2) \tag{6.21}$$

$$\frac{\delta}{\delta A_\mu^{\epsilon,c}(q)}\Gamma^{\epsilon_1,\mu_1,\mu_2,\mu_3,c_1,c_2,c_3}(q_1,q_2,q_3) = \delta^{\epsilon\epsilon_1}\Gamma^{\epsilon,\mu_1\mu_2\mu_3,\mu,c_1,c_2,c_3,c}(q_1,q_2,q_3,q) \tag{6.22}$$

$$\tfrac{\delta}{\delta A_\mu^{\epsilon,c_1}(q)}\Gamma^{\epsilon_1,\mu_1\mu_2\mu_3,\mu_4,c_1,c_2,c_3,c_4}(q_1,q_2,q_3,q_4) = 0 \tag{6.23}$$

with the classical structure for the 3-gluon Yang-Mills vertex

$$\Gamma_{\mu_1,\mu_2,\mu_3}^{\epsilon,c_1,c_2,c_3}(q_1,q_2,q_3) = \epsilon g f^{c_1c_2c_3}(g_{\mu_1\mu_2}(q_3-q_1)_{\mu_3}+g_{\mu_2\mu_3}(q_1-q_2)_{\mu_1}+g_{\mu_3\mu_1}(q_2-q_3)_{\mu_2}) \tag{6.24}$$

and the 4-gluon Yang-Mills vertex

$$\Gamma_{\mu_1\mu_2\mu_3\mu_4}^{\epsilon,c_1,c_2,c_3,c_4}(q_1,q_2,q_3,q_4) = -\epsilon i g^2\delta^{(4)}(q_1+q_2+q_3+q_4) \tag{6.25}$$

$$(f^{c_1c_2e}f^{c_3c_4e}(g_{\mu_1\mu_3}g_{\mu_2\mu_4}-g_{\mu_1\mu_4}g_{\mu_2\mu_3}) \tag{6.26}$$

$$+f^{c_1c_3e}f^{c_2c_4e}(g_{\mu_1\mu_2}g_{\mu_3\mu_4}-g_{\mu_1\mu_4}g_{\mu_2\mu_3}) \tag{6.27}$$

$$+f^{c_1c_4e}f^{c_2c_3e}(g_{\mu_1\mu_2}g_{\mu_3\mu_4}-g_{\mu_1\mu_3}g_{\mu_2\mu_4})) \tag{6.28}$$

Note, that the branch index determines the sign of the Yang-Mills-vertex. Each of the EMT-vertices is connected to either two, three or four gluon lines, imposing a natural classification for the diagrams. However, the number of loops varies within each class.

Therefore,

$$D^{\epsilon_1,\epsilon_2}_{n_1,n_2}(L) \tag{6.29}$$

denotes the diagrammatic part with branch indices ϵ_1, ϵ_2, the number n_1 of legs of the left EMT-vertex, the number n_2 of legs of the right EMT-vertex and L loops. The free Lorenz indices $\vec{\mu}$, color indices $\vec{c}$ and momentum variables $\vec{q}$ from the decomposition (6.7) are not explicitly carried along in $D^{\epsilon_1,\epsilon_2}_{n_1,n_2}(L)$ in order to avoid overloading of indices.

For given n_1, n_2, the minmum number of loops is given by

$$L_{min} = \lfloor \tfrac{n_1+n_2-1}{2} \rfloor \tag{6.30}$$

with the Gaussian bracket $\lfloor x \rfloor = \max\{n \in \mathbb{Z} | n \leq x\}$, while the maximum number of loops is

$$L_{max} = n_1 + n_2 - 2. \tag{6.31}$$

The validity of equations (6.30) and (6.31) can be checked by explicit evaluation of (6.4) with the deomposition (6.7) of the spatial traceless part the EMT (6.5). In particlar, the overall minimum number of loops is 1, while the maximum is assumed for $n_1 = n_2 = 4$, yielding $L_{max,total} = 6$. In the following sections the diagrams up to 2-loop order are evaluated and classified.

6.3 1-loop diagram

There obviously is merely a single 1-loop diagram, which is shown in 6.1. Its calculation works as a instructive application of the magic formula. The 1-loop contribution is

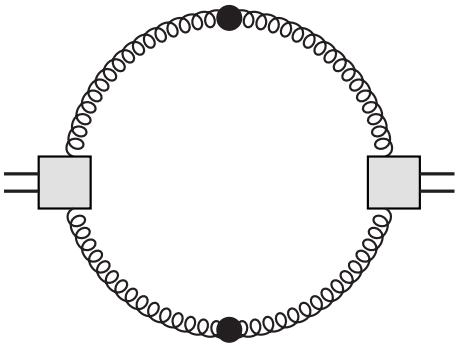

Figure 6.1: Unique 1-loop contribution to the correlation function $\langle \pi_{ij} \pi_{ij} \rangle$ of the spatial traceless part π_{ij} of the energy momentum tensor. The full Yang-Mills vertices are denoted by filled black circles, whereas the EMT vertices are depicted by gray squares.

obtained by picking the abelian parts of the field strength tensors. This corresponds to picking the first term in (6.7) which is proportional to $\alpha^{(2)}$. Thus, the magic formula is evaluated for

$$D_{2,2}^{\epsilon_1,\epsilon_2}(1) \equiv \langle A_{\mu_1}^{c_1,\epsilon_1}(k_1) A_{\mu_2}^{c_2,\epsilon_1}(k_2) A_{\mu_3}^{c_3,\epsilon_2}(k_3) A_{\mu_4}^{c_4,\epsilon_2}(k_4) \rangle_{1-loop} \tag{6.32}$$

with $D_{2,2}^{\epsilon_1,\epsilon_2}(1)$ defined in (6.29). Note, that the former two fields belong to the left EMT-vertex in Fig. 6.1 while the latter two fields belong to the right EMT-vertex.

$$D_{2,2}^{\epsilon_1,\epsilon_2}(1) = [(G^{\epsilon_1\bar{\epsilon_1}} \cdot \frac{\delta}{\delta A^{\bar{\epsilon_1}}} + A^{\epsilon_1})(G^{\epsilon_1\bar{\epsilon_2}} \cdot \frac{\delta}{\delta A^{\bar{\epsilon_2}}} + A^{\epsilon_1}) \tag{6.33}$$

$$\times (G^{\epsilon_2\bar{\epsilon_3}} \cdot \frac{\delta}{\delta A^{\bar{\epsilon_3}}} + A^{\epsilon_2})(G^{\epsilon_2\bar{\epsilon_4}} \cdot \frac{\delta}{\delta A^{\bar{\epsilon_4}}} + A^{\epsilon_2})]_{1-loop} \tag{6.34}$$

Again, the Lorenz and momentum structure has been dropped for better readability. For each field two terms can be picked, leading to $2^4 = 16$ combinations. Further, each combination can produce a number of different diagrams, as the derivatives can act on any object to the right. However, there is no finite background field, and any terms with surviving fields will vanish. Similarly, terms with remaining field derivatives vanish trivially. In particular, only the field in the rightmost term and the derivative in the leftmost term will give rise to non-vanishing contributions:

$$D_{2,2}^{\epsilon_1,\epsilon_2}(1) = [G^{\epsilon_1\bar{\epsilon_1}} \cdot \frac{\delta}{\delta A^{\bar{\epsilon_1}}}(G^{\epsilon_1\bar{\epsilon_2}} \cdot \frac{\delta}{\delta A^{\bar{\epsilon_2}}} + A^{\epsilon_1})(G^{\epsilon_2\bar{\epsilon_3}} \cdot \frac{\delta}{\delta A^{\bar{\epsilon_3}}} + A^{\epsilon_2})A^{\epsilon_2}]_{1-loop} \tag{6.35}$$

Expanding (6.35) will also produce numerous 2-loop diagrams (but no higher loop diagrams according to (6.31)), that will be considered below. For now, let us consider the 1-loop term by picking one more field, and one more field derivative. The only contributions then are the 1-loop diagram in Fig.6.1 and a disconnected diagram, which is 2-loop. The 1-loop diagram is obtained for the combination:

$$D_{2,2}^{\epsilon_1,\epsilon_2}(1) = [G^{\epsilon_1\bar{\epsilon_1}} \cdot \frac{\delta}{\delta A^{\bar{\epsilon_1}}} G^{\epsilon_1\bar{\epsilon_2}} \cdot \frac{\delta}{\delta A^{\bar{\epsilon_2}}} A^{\epsilon_2} A^{\epsilon_2}] \tag{6.36}$$

At this point it cannot be avoided to reintroduce all tensor structures for the gluon fields.

$$D_{2,2}^{\epsilon_1,\epsilon_2}(1) = G_{\mu_1\tilde{\mu_1}}^{\epsilon_1,\tilde{\epsilon_1},c_1\tilde{c_1}}(k_1,\tilde{k_1}) \cdot \frac{\delta}{\delta A_{\tilde{\mu_1}}^{\tilde{\epsilon_1},\tilde{c_1}}(\tilde{k_1})} \tag{6.37}$$

$$\times\, G_{\mu_2\tilde{\mu_2}}^{\epsilon_1,\tilde{\epsilon_2},c_2\tilde{c_2}}(k_2,\tilde{k_2}) \cdot \frac{\delta}{\delta A_{\tilde{\mu_2}}^{\tilde{\epsilon_2},\tilde{c_2}}(\tilde{k_2})} A_{\mu_3}^{\epsilon_2,c_3}(k_3) A_{\mu_4}^{\epsilon_2,c_4}(k_4) \tag{6.38}$$

$$= G_{\mu_1\mu_3}^{\epsilon_1,\epsilon_2,c_1c_3}(k_1,-k_3) G_{\mu_2\mu_4}^{\epsilon_1,\epsilon_2,c_2c_4}(k_2,-k_4) \tag{6.39}$$

$$+\, G_{\mu_1\mu_4}^{\epsilon_1,\epsilon_2,c_1c_4}(k_1,-k_4) G_{\mu_2\mu_3}^{\epsilon_1,\epsilon_2,c_2c_3}(k_2,-k_3) \tag{6.40}$$

$$= G_{\mu_1\mu_3}^{\epsilon_1,\epsilon_2,c_1c_3}(k_1,-k_3) G_{\mu_2\mu_4}^{\epsilon_1,\epsilon_2,c_2c_4}(k_2,-k_4) + \{3 \longleftrightarrow 4\} \tag{6.41}$$

The notation $\{3 \longleftrightarrow 4\}$ indicates the exchange of all indices with the respective subscripts. As expected the magic formula produces two terms for the one loop diagram. Both terms are identical under exchange of the gluon lines of one of the EMT vertices. Thus, the magic formula already naturally takes care of any symmetry factors.

Equation (6.41) can be contracted with the corresponding EMT tensor structure (6.18) for $n = m = 2$. The number of terms blows up during the calculation,which therefore cannot be shown here. The calculation is performed using Mathematica 9 employing the 'x-tensor package [163]. Here, only a sketch of the calculation is given:
The tensor structure for the finite temperature gluon propagators in Landau gauge is given in (8.1). In the real time formalism each scalar propagator receives the branch indices from the full tensorial propagator. The longitudinal and transverse scalar propagators are then expressed in terms of their respective spectral functions (review chapter 5). In a last step, the imaginary part of the full expression is taken in order to get the spectral function of the EMT. The EMT spectral function depends on the four momentum components. For the main application of this thesis, the determination of $\frac{\eta}{s}$, the zero spatial momentum limit is needed. However, this limit of $\vec{p} \to 0$ can be trivially taken.

$$\begin{aligned}
\rho_{\pi\pi}(\omega) \;=\; & \frac{2d_A}{3} \int \frac{d^4k}{(2\pi)^4} [n(k^0) - n(k^0+\omega)] \\
& \times \{V_1(k,\omega)\rho_T(k^0,\vec{k})\rho_T(k^0+\omega,\vec{k}) \\
& + V_2(k,\omega)\rho_T(k^0,\vec{k})\rho_L(k^0+\omega,\vec{k}) \\
& + V_3(k,\omega)\rho_L(k^0,\vec{k})\rho_L(k^0+\omega,\vec{k})\}\,,
\end{aligned} \tag{6.42}$$

2-loop diagram	g_{EMT}	g_{YM}	g_{Total}
Sunset	2	0	2
Maki-Thompson	0	2	2
Eight	0	2	2
Squint	1	1	2
vertex corr.	2	0	2

Table 6.1: Dependence of the two-loop diagram on the running coupling.

with $d_A = N_c^2 - 1$, and

$$\begin{aligned} V_1(k) &= 7(k^2)^2 - 10k_0^2\vec{k}^{\,2} + 7k_0^4 \\ V_2(k) &= 6k_0^2(k_0^2 - \vec{k}^{\,2}) \\ V_3(k) &= 2(k_0^2 - \vec{k}^{\,2})^2 \,. \end{aligned} \tag{6.43}$$

6.4 2-loop diagrams

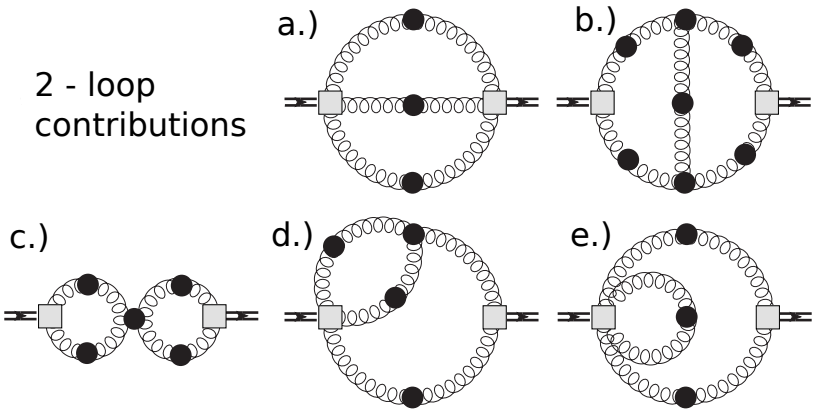

Figure 6.2: 2-Loop contributions to the correlation function $\langle \pi_{ij}\pi_{ij} \rangle$ of the spatial traceless part π_{ij} of the energy momentum tensor: Sunset (a), Maki-Thompson (b), Eight (c), Squint (d), 1-loop with a single vertex correction (e).The full Yang-Mills vertices are denoted by filled black circles, whereas the EMT vertices are depicted by gray squares.

At two loop order the contributions to the correlation function $\langle \pi_{ij}\pi_{ij} \rangle$ of the spatial traceless part π_{ij} of the energy momentum tensor, are given by the diagrams shown in Fig.6.2. Once again, for the classical energy-momentum tensor, no ghost propagators can occur at two loop level. While, the 1-loop diagram was independent of the running coupling, the 2-loop expressions are proportional to $g^2 = 4\pi\alpha_s$. However, the source of the g-factors differs among the 2-loop diagrams: The sunset diagram and the 1-loop diagram with a single vertex correction contain no Yang-Mills vertices. The dependence

on α_s comes from the g-factors in the field-strength tensor. Whereas Maki-Thompson and Eight are contributions of the Abelian part of the field strength tensor containing no g-factors. But their g^2-dependence originates from the two 3-gluon vertices and the 4-gluon vertex, respectively. The squint contribution is hybrid in this sense, with one g coming from the 3-leg EMT vertex and the other coming from the 3-gluon vertex.

The distinction is interesting, as it allows to study the results with respect to the vertex dressing. The Yang-Mills vertices were obtained from the full propagators, thus it seems reasonable to employ a temperature dependent running coupling. For the EMT vertices on the other hand, the classical ghost-free tensor expression is employed. A dressing with a running α_s has at least to be discussed. This discussion is found in 9 in the context of the discussion of the 2-loop correction to $\frac{\eta}{s}$.

Analog to the 1-loop diagrammatic part of (6.36) which led after contraction of all indices to the diagrammatic exression (6.41), in the 2-loop case all diagrams are be studied seperately.

6.4.1 Sunset

For the sunset diagram the $\alpha^{(3)}$-$\alpha^{(3)}$ contribution is picked. The diagrammatic part reads:

$$D_{3,3}^{\epsilon_1,\epsilon_2}(2) \equiv \langle A_{\mu_1}^{c_1,\epsilon_1}(k_1) A_{\mu_2}^{c_2,\epsilon_1}(k_2) A_{\mu_3}^{c_3,\epsilon_1}(k_3) A_{\mu_4}^{c_4,\epsilon_2}(k_4) A_{\mu_5}^{c_5,\epsilon_2}(k_5) A_{\mu_6}^{c_6,\epsilon_2}(k_6) \rangle_{sunset} \tag{6.44}$$

For the fields coming from the left EMT, i.e. the first three A-fields in (6.44), the field derivative is picked, whereas for the latter three fields the average is picked. The only non-vanishing contribution arises from each derivative hitting an expectation value (no background field). Analog to equation(6.41), the sunset diagrammatic part yields

$$\begin{aligned} D^{\epsilon_1,\epsilon_2}(3,3)(2) =& G_{\mu_1\mu_4}^{\epsilon_1,\epsilon_2,c_1c_4}(k_1,-k_4) G_{\mu_2\mu_5}^{\epsilon_1,\epsilon_2,c_2c_5}(k_2,-k_5) G_{\mu_3\mu_6}^{\epsilon_1,\epsilon_2,c_3c_6}(k_3,-k_6) && (6.45) \\ &+ \{\text{symmetrize } 4,5,6\} && (6.46) \end{aligned}$$

The fully contracted expression,however, is too lengthy to be given explicitly, even after seperation of combinations of longitudinal and transverse propagators.

6.4.2 Eight

For the diagram 'Eight' the $\alpha^{(2)}$-$\alpha^{(2)}$ contribution is picked. The diagrammatic part is given by expression (6.32). However, this time a different choice for the combination of field derivatives and field expectation values is picked. Obviously, for the eight, all gluon lines form a 4-gluon vertex. This is obtained by picking the three field derivatives for the three fields on the left.The first derivative hits the field generating a propagator. The second derivative, hitting the propagator generates a 3-gluon vertex, and the third derivative finally generates the 4-gluon vertex:

$$D_{2,2}^{\epsilon_1,\epsilon_2}(2,'\text{Eight}') = [G^{\epsilon_1\bar{\epsilon_1}} \cdot \frac{\delta}{\delta A^{\bar{\epsilon_1}}} G^{\epsilon_1\bar{\epsilon_2}} \cdot \frac{\delta}{\delta A^{\bar{\epsilon_2}}} G^{\epsilon_2\bar{\epsilon_3}} \cdot \frac{\delta}{\delta A^{\bar{\epsilon_3}}} A^{\epsilon_2}]_{eight} \tag{6.47}$$

The 4-gluon vertex carries a branch index $\epsilon \in \{+,-\}$. In particular, 'Eight' is the first diagram that contains diagonal elements of the real-time propagator matrix. The part of the Eight containing transverse gluon only is shown for vanishing external frequency as an example for a typical term.

$$-\frac{128}{135} g^2 (5k^2 - 7k_0^2)(5q^2 - 7q_0^2)\rho_T(k_0,k)\rho_T(q_0,q) \tag{6.48}$$

$$(n(k_0)^2(2n(q_0)+1) \tag{6.49}$$

$$F_T(q_0,q)\rho_T(k_0,k) + n(k_0)((2n(q_0)+1) \tag{6.50}$$

$$\times F_T(q_0,q)\rho_T(k_0,k) + 2n(q_0)(n(q_0)+1) \tag{6.51}$$

$$\times F_T(k_0,k)\rho_T(q_0,q)) + n(q_0) \tag{6.52}$$

$$\times (n(q_0)+1)F_T(k_0,k)\rho_T(q_0,q)) \tag{6.53}$$

6.4.3 Maki-Thompson

Maki-Thomspon is another $\alpha^{(2)}$-$\alpha^{(2)}$ contribution. Similar to the 'Eight', three field derivatives are picked. This time, however, two of the field derivatives hit propagators. There are two distinct classes of Maki-Thompson diagrams, which are called 'pure' and 'mixed'. The pure Maki-Thompson diagrams are the diagrams with either two $+$ internal Yang-Mills vertices or two $-$ vertices. These diagrams have three diagonal propagator elements (either three G^{++} propagators or three G^{--} propagators) and two off-diagonal elements. On the other hand, there are the mixed Maki-Thompson diagrams with either $+/-$ or $-/+$ combination of internal Yang-Mills vertices. Mixed Maki-Thompson diagrams do not contain any diagonal propagator elements.

The distinction is of interest, as it raises the question of convergence of each diagram type. While the off-diagonal propagator elements ensure convergence by occurence of distribution functions, the convergence of loops containing diagonal elements has to be studied more carefully. The topic of convergence is discussed in chapter 8.

6.4.4 Squint

The squint is the only 2-loop contribution of the $\alpha^{(3)}$-$\alpha^{(2)}$ ($\alpha^{(2)}$-$\alpha^{(3)}$) diagrams. The diagrammatic part of the 3-2 diagram reads:

$$D^{\epsilon_1,\epsilon_2}_{3,2}(2) \equiv \langle A^{c_1,\epsilon_1}_{\mu_1}(k_1) A^{c_2,\epsilon_1}_{\mu_2}(k_2) A^{c_3,\epsilon_1}_{\mu_3}(k_3) A^{c_4,\epsilon_2}_{\mu_4}(k_4) A^{c_5,\epsilon_2}_{\mu_5}(k_5) \rangle_{squint} \tag{6.54}$$

The odd number of gauge fields immediately requires the appearance of at least one internal Yang-Mills vertex. To obtain a non-vanishing contribution, the number of field derivatives picked must exceed the number of field expectation values. Picking four field derivatives leads to a 3-loop diagram. Thus, the squint contribution is obtained by picking three field derivatives. Similar to the one-loop case, this does not fully determine the squint diagram. The are also occuring disconnected diagrams or one gluon exchange diagrams. In Fig.6.3 the two classes of diagrams are shown. They

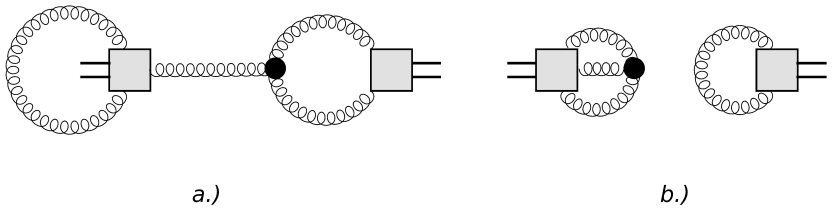

Figure 6.3: The 2-loop contribution contains one more diagram types beside the squint: The one-gluon exchange (a). Further, a fully disconnected 3-loop contribution is possible (b).

both do not contribute to the EMT spectral function. For diagram a.) it suffices to study the color structure: The 2-leg EMT-vertex in diagram (a.) is proportional to $\delta^{c_1 c_2}$. The two propagators attached to it form a 3-gluon vertex with one line of the 3-leg EMT-vertex. The 3-gluon vertex is, however, is proportional to $f^{c_1 c_2 a}$. Thus, contracting the color structure forces the diagram to vanish.

The disconnected diagram b.) vanishes, when taking the commutator of the EMT correlator. This shows, that the only non-vanishing contribution is indeed the squint.

It is obtained by the field derivatives for the three gauge fields to the left of (6.54).

6.4.5 1-loop with single vertex correction

The 1-loop with single vertex correction is the single 2-loop contribution of the $\alpha^{(4)}$-$\alpha^{(2)}$ ($\alpha^{(2)}$-$\alpha^{(4)}$) diagrams. The diagrammatics of the 4-2 case reads:

$$D_{4,2}^{\epsilon_1,\epsilon_2}(2) \equiv \langle A_{\mu_1}^{c_1,\epsilon_1}(k_1) A_{\mu_2}^{c_2,\epsilon_1}(k_2) A_{\mu_3}^{c_3,\epsilon_1}(k_3) A_{\mu_4}^{c_4,\epsilon_1}(k_4) A_{\mu_5}^{c_5,\epsilon_2}(k_5) A_{\mu_6}^{c_6,\epsilon_2}(k_6) \rangle_{vertex_corr} \quad (6.55)$$

This diagram is of certain interest for two reasons. The first is, that its structure is very similar to the leading oder 1-loop contribution with a correction of one of the EMT-vertices (even though it differs due to the different tensor structures of the EMT with 2(4) legs). Thus, its size will also be an indicator for the size of higher loop correction as the 1-loop with two vertex corrections. Secondly, the convergence of the correction loop integral will be regulated by the behaviour of the spectral function.

7 Maximum Entropy Method

'Menschen, die wie wir an die Physik glauben, wissen,
dass die Unterscheidung zwischen Vergangenheit, Gegenwart und Zukunft
nur eine besonders hartnäckige Illusion ist.'
Albert Einstein

In many branches of science the problem occurs to reconstruct objects from measurement data. Here, the term 'ojbect' includes a functional dependence, that is inferred from measurement as well as the determination of an animal species from DNA testing. Such a problem can be ambiguous in two ways. The first ambiguity, of course, lies in unavoidable measurement errors, which can be of stochastic and systematic nature. The second ambiguity, being more subtle, originates in an uncomplete measurement, in the sense, that not all information necessary for the reconstruction could be measured. Suppose, for example, the general problem of image reconstruction formulated by Frieden [164]:'Given M sampled values of an incoherent object, what can be deduced to be the most likely object?'. The word 'incoherent' is used to describe both types of ambiguity. The statement also implies, that the best reconstruction can only be the most likely, compatible with the data and contraints from a priori available information, which will be called the 'model'.
This brings about some issues: Assuming, the measurement cannot be improved, what is the best known model? How can this model be incorporated in the reconstruction? How to weigh the data with respect to the model?
An algorithm dealing with all these issues is the Maximum Entropy Method (MEM). Today, MEM is a widely applied tool in high energy physics for analysing i.e. quantum Monte Carlo data, lattice data or the reconstruction of spectra from continuum methods [165–172]. In this chapter, the algorithm will be discussed in detail. Further, an extension to non-positive images is introduced, to allow the application of the extended-MEM to gluon spectral functions.

7.1 General challenge

In this short section the general challenge to invert an integral equation is introduced. Suppose, there is some measured correlation function $G(\tau)$, that is related to some (unknown) positive (semi)-definite function $\rho(\omega)$ - which we call spectral function in anticipation of the main application - by the integral equation

$$G(\tau) = \int d\omega K(\tau, \omega)\rho(\omega) \tag{7.1}$$

where, for now, $K(\tau, \omega)$ is a known and well-behaved[1] but otherwise arbitrary integral kernel. Suppose further, $G(\tau)$ is known by measurement at $\tau_i (i = 1, ..., N_\tau)$, with uncertainties $\sigma(\tau_i)$. The aim is to calculate the best (educated) guess for the spectral function considering any a priori knowledge on its shape. Such knowledge can be the asymptotic behaviour $\rho(\omega \to \infty)$. In the case of gluons the this asymptotic behaviour is fixed by perturbation theory.

First, a naive approach to the inversion problem is introduced, to point out the difficulties of ambiguity and of over-weighting the a priori knowledge.

7.2 Naive approach to image reconstruction

It has been proposed to make a parametric ansatz $\rho_{model}(\omega, b_1, ...b_m)$ in terms of the parameters b_i for $\rho(\omega)$ [173] and minimize the likelihood L defined as[2]

$$L = \frac{1}{N} \sum_{i=1}^{N_\tau} \frac{1}{(\sigma_i)^2} \left(G(\tau_i) - G_{model}(\tau_i, b_1, ..., b_m)\right)^2 \tag{7.2}$$

with

$$G_{model}(\tau, b_1, ..., b_m) = \int d\omega K(\tau, \omega)\rho_{model}(\omega, b_1, ...b_m) \tag{7.3}$$

However, this naive approach has the inherent disadvantage of limiting the search space to the space spanned by the parameters $b_i (i = 1, ..., m)$. Therefore, on the one hand, the resulting spectral function can only be as good, as the initial guess, and secondly, no estimate on the quality of the result is possible, as there can be a different ansatz

[1] In the sense, that $K(\tau, \omega)$ is meromorphic

[2] In general, the likelihood will be non-diagonal, due to non-independent measurement uncertainties. For now, however, a diagonal likelihood is assumed for convenience. The extension to non-diagonal likelihoods is found later in this chapter.

$\bar{\rho}_{model}(\omega, \bar{b}_1, ...\bar{b}_{\bar{m}})$ with $|\bar{L}| << |L|$. An example illustrates that issue: Consider the integral kernel

$$K(\tau, \omega) = e^{-\tau\omega} \tag{7.4}$$

and a mock spectral function $\rho(\omega) = \frac{1}{2}\omega^2\Theta(\omega)$. The correlation function is

$$\begin{aligned} G(\tau) &= \frac{1}{2}\int_{-\infty}^{\infty} d\omega e^{-\tau\omega}\omega^2\Theta(\omega) && (7.5)\\ &= \frac{1}{2}\int_{0}^{\infty} d\omega e^{-\tau\omega}\omega^2 && (7.6)\\ &= \frac{1}{2}\frac{\partial^2}{\partial\bar{\tau}^2}\int_{0}^{\infty} d\omega e^{-\bar{\tau}\omega}|_{\bar{\tau}=\tau} && (7.7)\\ &= \frac{1}{2}\frac{\partial^2}{\partial\bar{\tau}^2}\frac{1}{\bar{\tau}}|_{\bar{\tau}=\tau} && (7.8)\\ &= \frac{1}{\tau^3} && (7.9)\\ & && (7.10) \end{aligned}$$

Further, a mock measurement at N values of τ in the interval $I = [0, \tau_{max}]$ yields

$$G_{meas}(\tau_i) = \frac{1 + \delta_i}{\tau_i^3} \tag{7.11}$$

with $\frac{|\delta_i|}{\tau_i^3} \leq \sigma_i$. For convenience the limiting case of $\frac{|\delta_i|}{\tau_i^3} = \sigma_i$ is considered:

$$G_{meas}(\tau_i) = \frac{1}{\tau_i^3} + \text{sign}(\delta_i)\sigma_i \tag{7.12}$$

The likelihood obtained with the true correlator as model correlator yields

$$L = \frac{1}{N}\sum_{i=1}^{N_\tau}\frac{1}{(\sigma_i)^2}\left(\frac{1}{\tau_i^3} + \text{sign}(\delta_i)\sigma_i - \frac{1}{\tau_i^3}\right)^2 = 1 \tag{7.13}$$

Now, however a different ansatz is chosen for the model spectral function:

$$\rho_{model}(\omega, b_1) = b_1\omega\Theta(\omega) \tag{7.14}$$

Obviously, the 'true' spectral function is not part of the search space. The corresponding correlator is calculated as above

$$G_{(model)}(\tau, b_1) = b_1 \frac{1}{\tau^2} \tag{7.15}$$

Even though a reasonable result cannot be expected, let us evaluate the likelihood function

$$\begin{aligned} L &= \frac{1}{N} \sum_{i=1}^{N_\tau} \frac{1}{(\sigma_i)^2} \left(\frac{1}{\tau_i^3} + \text{sign}(\delta_i)\sigma_i - b_1 \frac{1}{\tau_i^2} \right)^2 && (7.16) \\ &= \frac{1}{N} \sum_{i=1}^{N_\tau} \left(1 + \text{sign}(\delta_i) \frac{1 - b_1 \tau_i}{|\delta_i|} \right)^2 && (7.17) \\ & && (7.18) \end{aligned}$$

In all practical measurements the likelihood (7.17) will be greater than 1, but nevertheless it is possible to construct examples, such that a model function with a wrong asymptotic behaviour can yield lower likelihoods, than the true spectral function. This observation even worsens the problem, and demonstrates the need for a better algorithm, especially, when one keeps in mind, that in general one does not seek to reconstruct designed mock measurements, and the spectral function truely is unknown.

7.3 Extension of the naive approach

In this section the standard-MEM algorithm is derived. It will be shown that the introduction of an entropy term will remove the ambiguities of the MEM-image.

It is interesting to ask, why the naive method can fail in many scenarios? The answer is quite simple. Introducing a priori information of the shape of the spectral function by including adequate basis functions in the search space is not sufficient. There is no term, that explicitly punishes deviations from the correct asymptotic behaviour as the correlation data alone cannot fix the asympotics.

That becomes clear, by observing, that the large ω behaviour of ρ is governed by the correlation function in the vicinity of $\tau = 0$[3]. For discrete data, this usually implies, that only a single data point contains most information on the asymptotics.

[3]This statement is true for the kernel (7.4) and will be true for all kernels considered in this thesis.

A punishment term can be introduced in the form of an entropy, which was first formulated by Shannon [174] and subsequently applied to statistical physics by Jaynes [175, 176] and is therfore known as Shannon-Jaynes entropy. By introducing the Shannon-Jaynes entropy

$$S = \int_0^\infty d\omega \left(\rho(\omega) - m(\omega) - \rho(\omega) \log \left(\frac{\rho(\omega)}{m(\omega)} \right) \right) \tag{7.19}$$

and minimising the combined quantity

$$Q(\alpha) = L - \alpha S, \tag{7.20}$$

the naive approach is extended to punish deviations form the model. The model function $m(\omega)$ introduced in (7.19) is chosen, such that it contains the a priori known shape of the spectral function. The Lagrange multiplier α, regulates the relative weight of the data to the a priori model. In the limit $\alpha \to 0$ the naive approach is retrieved, while for $\alpha \to \infty$ the result of the extended algorithm will be $\rho(\omega) = m(\omega)$. Note, that the entropy S is always non-positive, such that $Q(\alpha)$ is bounded from below by $Q(\alpha) = 0$. To see this, both spectral function and model function are assumed to be positive definite, so that the spectral function, can be written without loss of generality as

$$\rho(\omega) = m(\omega) e^{f(\omega)} \tag{7.21}$$

Inserting (7.21) into (7.19) one finds for all $\omega \in [0, \infty]$:

$$\rho(\omega) - m(\omega) - \rho(\omega) \log \left(\frac{\rho(\omega)}{m(\omega)} \right) = m(\omega) \left(e^{f(\omega)} (1 - f(\omega)) - 1 \right) \tag{7.22}$$

with exhibits a global maximum at $f(\omega) = 0$ with value 0. This immediately follows by differentiation with respect to $f(\omega)$. In particular, the maximum is assumed for $\rho(\omega) = m(\omega)$, following from (7.21).

The Maxiumum entropy method is obtained by a certain choice for the parametrization of the spectral function. This parametrization is discussed in Section7.5. For let us assume, this choice is picked, and the naive approach, also called, Minimum Likelihood Method (MLM) is promoted to MEM.
The minimization of $Q(\alpha)$ simultaneously optimizes the image with respect to the cor-

relation data and the model. However, so far the result will depend on the choice of α. The dependence can be eliminated, by suitably averaging over α, which is discussed now in terms of Bayesian probability theory.

7.4 Bayes' theorem of conditional probability

Bayes' theorem is a general statement about conditional likelihoods. Suppose two events X, Y that occur with likelihoods $P[X], P[Y]$. Then, the likelihood $P[X|Y]$ of event X occuring given Y is [177]:

$$P[X|Y] = \frac{P[Y|X]P[X]}{P[Y]} \tag{7.23}$$

It is useful to translate the MEM idea of Section7.3 into the language of conditional probabilities. Let D be the measured correlation data including its uncertainties and M be all prior knowledge about the spectral function ρ. Then, using Bayes' theorem (7.23):

$$P[\rho|DM] = \frac{P[D|\rho M]P[\rho|M]}{P[D|M]} \tag{7.24}$$

The four conditional probabilities are easily related to the MEM quantities. The LHS gives the probability for a spectral function given data and model. The aim is to calculate the most likely spectral function, i.e:

$$\frac{\delta P[\rho|DM]}{\delta \rho} = 0 \tag{7.25}$$

On the RHS, $P[D|M]$ is merely a ρ-independent normalization factor, that does not play a role in (7.25). Assuming the measurement data is Gaussian distributed around some central value, $P[D|\rho M]$ can be written as

$$P[D|\rho M] = \frac{1}{Z_L} e^{-L} \tag{7.26}$$

with a normalisation factor Z_L and the likelihood L defined in (7.2). Finally, if $P[\rho|M]$, could be interpreted as αS with the entropy (7.19), the MEM algorithm would be very simple. However, the weight parameter α and the model function m are to be distinguished from the prior information M. To clarify this: The prior knowledge M describes the abstract collection of prior information, while the model function is an explicit representation of M. Therefore, the entropy connects to the Bayesian

probability

$$P[\rho|M\alpha m] = \frac{1}{Z_S} e^{\alpha S} \tag{7.27}$$

To obtain the most likely spectral function ρ_{opt} both α and m must be integrated out. In practice, however, only the α average is performed, such that ρ_{opt} remains model dependent. The most likely spectral function is given by

$$\rho_{opt}(\omega) = \int [d\rho] \int d\alpha \rho(\omega) P[\rho|DM\alpha m] P[\alpha|DMm] \tag{7.28}$$

where $P[\rho|DM\alpha m]$ is given by (7.24) and is usually assumed to be peaked around some $\alpha = \hat{\alpha}$, and (7.28) is written as

$$\rho_{opt}(\omega) = \int d\alpha \rho_\alpha(\omega) P[\alpha|DMm] \tag{7.29}$$

Further the probability $P[\alpha|DMm]$ is given by

$$P[\alpha|DMm] = P[\alpha|Mm] \exp\left[\tfrac{1}{2} c(\alpha) + \alpha S(\rho_{\hat{\alpha}}) - L(\rho_{\hat{\alpha}})\right] \tag{7.30}$$

in terms of an α-dependent constant $c(\alpha)$ calculated below and an integral measure, $P[\alpha|Mm]$, which cannot be further constrained. Common choices are Jeffrey's rule $P[\alpha|DMm] = \frac{1}{\alpha}$ and Laplace's rule $P[\alpha|DMm] = 1$. The freedom of choice for the integral measure represents, that introducing α supplemented the system with an arti cficial degree of freedom. However, for a sharply peaked ρ_α in α-space, the form of the measure is not relevant.

7.5 MEM algorithm

To allow a numerical approach to the problem of reconstructing the spectral image, the ω-interval is disretized to a grid of N_ω points. Thus, the kernel reduces to a $N_\tau \times N_\omega$ matrix. The discretized version of the Shannon-Jaynes entropy (7.19) reads

$$S \approx \sum_{j=1}^{N_\omega} \rho(\omega_j) - m(\omega_j) - \rho(\omega_j) \log\left(\frac{\rho(\omega_j)}{m(\omega_j)}\right) \tag{7.31}$$

The MEM-parametrisation, already mentioned before, of $\rho(\omega)$ is directly related to the transpose of the integral kernel $K^T(\tau, \omega)$. To span the most general search space for the

spectral function, a (thin) singular value decomposition [178] of $K^T(\tau, \omega)$ is performed.

$$K^T = USV^T \tag{7.32}$$

where U is a (pseudo)-orthogonal $N_\omega \times N_\tau$ matrix, S is a diagonal $N_\tau \times N_\tau$ matrix and V is an orthogonal $N_\tau \times N_\tau$ matrix. The singular value decomposition is unique, if the non-negative entries of S (the so called singular values) are sorted. Usually, the sorting is done in decreasing magnitude. The entries of U are denoted by $u_{jl}(j = 1, ...N_\omega; l = 1, ..., N_\tau)$. The spectral function is parametrised by an N_τ-dimensional parameter vector $\vec{b}$ as

$$\rho_{MEM}(\omega_i, \vec{b}) = m(\omega_i)e^{u_{il}b_l} \tag{7.33}$$

For a positive model function, the ansatz (7.33) gives a positive ρ. As the aim is to minimize (7.20), one needs to evaluate the derivatives:

$$\frac{\partial Q}{\partial b_l} = \underbrace{\frac{\partial L}{\partial b_l}}_{1} - \underbrace{\alpha \frac{\partial S}{\partial b_l}}_{2} \tag{7.34}$$

The two summands are considered separately

$$\frac{\partial L}{\partial b_l} = \frac{\partial L}{\partial G(\tau_i)} \frac{\partial G(\tau_i)}{\partial \rho(\omega_j)} \frac{\partial \rho(\omega_j)}{\partial b_l} = \frac{\partial L}{\partial G(\tau_i)} K_{ij} \rho(\omega_j) u_{jl} \tag{7.35}$$

$$-\alpha \frac{\partial S}{\partial b_l} = -\alpha \frac{\partial S}{\partial \rho(\omega_j)} \frac{\partial \rho(\omega_j)}{\partial b_l} = \alpha \log(\frac{\rho(\omega_j)}{m(\omega_j)}) \rho(\omega_j) u_{jl} = \alpha u_{jk} b_k \rho(\omega_j) u_j l \tag{7.36}$$

Inserting the Singular Value Decomposition one finds

$$0 = \frac{\partial Q}{\partial b_l} = u_{jk} \underbrace{\left((SV^T)_{ki} \frac{\partial \vec{L}}{\partial G(\tau_i)} + \alpha b_k \right)}_{=0} \rho(\omega_j) u_{jl} \tag{7.37}$$

In order for this expression to vanish, the underbraced part must vanish. That is a suitable starting point for a multidimensional non-linear minimisation algorithm, as the expression inside the braces can be written as

$$\vec{g}(\vec{b}) \equiv (SV^T)_{ki} \frac{\partial \vec{L}}{\partial G(\tau_i)} = -\alpha b_k \tag{7.38}$$

Non-linear optimisation is cumbersome, and can easily lead to instabilities. Therefore, equation (7.38) is expanded to linear order in an arbitrary adjustment of $\vec{b} \to \vec{b}_{new} =$

$\vec{b} + \delta\vec{b}$, about $\vec{b}$:

$$(XT + \alpha I_{N_\tau})\delta\vec{b} = -(\alpha\vec{b} + g(\vec{b})) \tag{7.39}$$

with the b-independent matrix

$$X = SV^T \frac{\partial^2 L}{\partial G(\tau_i)\partial G(\tau_j)} VS \tag{7.40}$$

and the b-dependent matrix

$$T = U^T \mathrm{Diag}(\rho) U \tag{7.41}$$

While a Newton solver could already attack (7.39), the algorithm is unstable. The reason is, that there is no regulation of the magnitude of adjustments $\delta\vec{b}$, so too large adjustments can occur and the linearisation (7.39) is not justified. However, the Newton algortihm can be promoted to the Levenberg-Marquardt algorithm [179] by introducing the so called Levenberg-Marquardt parameter μ into (7.39):

$$(XT + (\alpha + \mu) I_{N_\tau})\delta\vec{b} = -(\alpha\vec{b} + g(\vec{b})) \tag{7.42}$$

The adjustment is calculated for some (small) value for the Levenberg-Marquardt parameter. If the calculated adjustment exceeds some fixed upper bound, μ is increased and the adjustment is recalculated. Once the adjustment satisfies the bound condition it is accepted and the Levenberg-Marquart parameter is reset to its initial value. Obviously, the size of each component of the increment $\delta\vec{b}$ decreases, as μ is increased. The procedure is repeated until the parameter vector $\vec{b}$ has converged to $\vec{b}^{opt}_{(\alpha)}$. The resulting spectral function $\rho(\omega, \vec{b}^{opt}_{(\alpha)})$ represents the α-dependent optimal spectral function $\rho_\alpha(\omega)$ in (7.29).
In a second step the α-integral (7.30) is performed, where the calculation of the constant $c(\alpha)$ remains.

7.6 Uniqueness of the MEM solution

The simultaneous minimisation of Q with respect to the data and the model function exhibits a unique global minimum. The proof is given in this section. For the proof a theorem of basic analysis is employed.

Theorem:

Consider a real valued, smooth function $f(x_1, ..., x_n)$ with $x_i \in \mathbb{R}$, such that

$$\sum_{i,j} y_i \frac{\partial^2 f}{\partial x_i \partial x_j} y_j < 0 \tag{7.43}$$

for all $y_i \in \mathcal{R}\backslash\{0\}$[4].Then f either exhibits only one maximum or f is unbounded from above.

To proof the theorem, assume, there are 2 distinct zeros

$$\frac{\partial f(\vec{x})}{\partial x_i} = 0 \;\; (i = 1, .., n) \tag{7.44}$$

labeled by $\vec{x}_1, \vec{x}_2$. Then there is a path connecting the zeros: $x(t) = x_1 + t(x_2 - x_1)$ with $t \in [0, 1]$. The function

$$g(t) = f(\vec{x}(t)) \tag{7.45}$$

is smooth with the property

$$g'(0) = g'(1) = 0 \tag{7.46}$$

Therefore, it exists a $\bar{t} \in (0, 1)$ such that $g''(\bar{t}) = 0$ contradicting (7.43) and establishing the proof.
To proof the uniqueness of the MEM solution, it is sufficient to show, that $-Q(\alpha)[\rho]$ has a negative definite hessian matrix with respect to $\rho_l = \rho(\omega_l)$, and that $-Q(\alpha)[\rho]$ is bounded. The boundedness trivially follows from the bounds of L and S. The negative-definiteness of the Hessian is shown for αS and $-L$ seperately. From (7.31) immediately follows

$$\sum_{i,j=1}^{N_\omega} y_i \frac{\partial^2(\alpha S)}{\partial \rho_i \partial \rho_j} y_j = -\alpha \sum_{i=1}^{N_\omega} \frac{y_i^2}{\rho_i} < 0 \tag{7.47}$$

for positive definite spectral functions. On the other hand the Hessian matrix for the likelihood yields

$$\sum_{i,j=1}^{N_\omega} y_i \frac{\partial^2(-L)}{\partial \rho_i \partial \rho_j} y_j = -\sum_{i=1}^{N_\omega} \frac{\bar{y}_i^2}{\sigma_i^2} \leq 0 \tag{7.48}$$

with

$$\bar{y}_i = \sum_{l=1}^{N_\omega} K_{il} y_l. \tag{7.49}$$

[4]In other words, the Hessian matrix of f is negative definite

The Hessian matrix of the likelihood is only negative semi-definite. Once more, this demonstrates, why Minimum Likelihood Method does not provide unique results for the spectral function. However, the sum (7.20) is negative definite, guaranteeing a unique solution.

7.7 α-average

To arrive at equation (7.30), Bayes's theorem (7.23) is used once more:

$$P[\alpha|DMm] = \frac{P[D|M\alpha m]P[\alpha|Mm]}{P[D|Mm]} \tag{7.50}$$

and the spectral function is introduced by de-marginalisation

$$P[\alpha|DMm] = \int [dA] \frac{P[D|AM\alpha m]P[A|H\alpha m]P[\alpha|Mm]}{P[D|Mm]} \tag{7.51}$$

As above, $P[D|Mm]$ is a normalisation constant, which plays no role for the extrema. Inserting the likelihood and the entropy one finds

$$P[\alpha|DMm] \approx P[\alpha|Mm] \int [d\rho] \frac{e^{Q(\alpha,\rho)}}{Z_L Z_S(\alpha)} \tag{7.52}$$

The quantity $Q(\alpha, \rho)$ is expanded about the minimum $Q(\hat{\rho}_\alpha)$ to next-to-leading order:

$$Q(\alpha, \rho) = Q(\hat{\rho}_\alpha) + \frac{1}{2} \sum_{ij} \delta\rho_i \frac{\partial^2 Q}{\partial\rho_i \partial\rho_j} \delta\rho_j + O(\delta\rho^3) \tag{7.53}$$

Coveniently, in the previous section the second order partial derivatives of Q were already calculated (see (7.47) and (7.48), such that:

$$Q(\alpha, \rho) \approx Q(\hat{\rho}_\alpha) - \frac{1}{2} \sum_{ij} \frac{\delta\rho_i}{\sqrt{\rho_i}} (\alpha I_{ij} + \Lambda_{ij}) \frac{\delta\rho_j}{\sqrt{\rho_j}} \tag{7.54}$$

with

$$\Lambda_{ij} = \left[\sqrt{\rho_k} \frac{\partial^2 L}{\partial\rho_k \partial\rho_l} \sqrt{\rho_l} \right]_{ij} \tag{7.55}$$

Inserting (7.54) with rescaled coordinates $\bar{\rho}_i = 2\sqrt{\rho_i}$ into (7.52) yields

$$P[\alpha|DMm] \approx P[\alpha|Mm]\frac{e^{Q(\hat{\rho}_\alpha)}}{Z_L Z_S(\alpha)}\int [d\bar{\rho}]e^{-\frac{1}{2}\delta\bar{\rho}\cdot(\alpha I+\Lambda)\cdot\delta\bar{\rho}} \tag{7.56}$$

$$= P[\alpha|Mm]\frac{e^{Q(\hat{\rho}_\alpha)}}{Z_L Z_S(\alpha)}\frac{(2\pi)^{\frac{N_\omega}{2}}}{\sqrt{\det(\alpha I+\Lambda(\hat{A}_\alpha))}} \tag{7.57}$$

Using $Z_S = \frac{(2\pi)^{N_\omega/2}}{\alpha}$ the result can be further simplified:

$$P[\alpha|DMm] \approx P[\alpha|Mm]\frac{e^{Q(\hat{\rho}_\alpha)}}{Z_L}\sqrt{\frac{\det(\alpha I)}{\det(\alpha I+\Lambda)}} \tag{7.58}$$

Comparing this expression to (7.30) finally yields

$$c(\alpha) = \frac{1}{2}\sum_i \log\left[\frac{\alpha}{\alpha+\lambda_i}\right] \tag{7.59}$$

with the eigenvalues λ_i of Λ.
This concluded the derivation of the standard-MEM algorithm. However, so far a diagonal likelihood is assumed. In the next section this constraint will be lifted.

7.8 Measurement uncertainties

In most practical scenarios, the correlator on the LHS of (7.1) will be subjected to measurement uncertainties, which will not be independent of each other. For example are measured quantities on the lattice of neighboring lattice sites correlated. So far, this is not included in the MEM algorithm. Suppose a series of N_{meas} identical measurements $G_{(n)}$ of the correlator G is performed and the average is calculated:

$$\bar{G}(\tau_i) = \frac{1}{N_{meas}}\sum_{n=1}^{N_{meas}} G_{(n)}(\tau_i) \tag{7.60}$$

Then the measurement uncertainties can be estimated by the covariance matrix:

$$C_{ij} = \frac{1}{N_{meas}(N_{meas}-1)}\sum_{n=1}^{N_{meas}}(G_{(n)}(\tau_i)-\bar{G}(\tau_i))(G_{(n)}(\tau_j)-\bar{G}(\tau_j)) \tag{7.61}$$

which also takes into account correlations between the measurements of different grid points. For that case the likelihood cannot immediately be cast in the form of (7.2), but needs to include the off-diagonal elements of the covariance matrix:

$$L = \frac{1}{2} \sum_{i,j=1}^{N_\tau} \left(G(\tau_i) - G_{model}(\tau_i, b_1, ..., b_m)\right) C_{ij}^{-1} \left(G(\tau_j) - G_{model}(\tau_j, b_1, ..., b_m)\right) \quad (7.62)$$

Since C is a real symmetric matrix, there exists an orthogonal matrix R such that

$$R^T C R = \mathrm{Diag}[(\sigma_i)^2] \quad (7.63)$$

is diagnonal with real valued eigenvalues σ_i. Transforming both kernel and correlator by R^T such that

$$K \to \bar{K} = R^{-1}K, \qquad G \to \bar{G} = R^{-1}G \quad (7.64)$$

casts the likelihood into the form (7.2) with σ_i given by (7.63). Thus the occurence of off-diagonal contributions in the covariance matrix can be reduced to the diagonal case by redefinition of correlater and integral kernel in the likelihood. Note, that MEM can also operate, if merely the averages of the correlation function with respective average errors are known. For that case (7.2) is used directly with errors included by the choice of the σ_i. The derivation of (7.59) is not affected by a non-diagonal covariance matrix, as no assumptions on the matrix (7.55) were made.

7.9 Non-positive spectral functions

While correlated errors can be included straightforwardly into MEM, the extension to non-positive semi-definite spectral functions needs some adjustments. First, note that the ansatz for the spectral function (7.33) can change its sign only if this is incorporated a priori in the model function. In principle, that is a feasible path, however it strongly limits one of the main strengths of MEM, namely the ability to find the spectral function without hard-limiting the search space. Therefore a different approach is chosen, by making the following assumption: Even if there is a part of the spectral function that violates positivity, the minimum of ρ will still be finite. Thus, poles and essential singulaties are excluded.
If however the minimum is finite, a shifted spectral function

$$\rho_s(\omega) = \rho(\omega) + s(\omega) \quad (7.65)$$

can be found, where $s(\omega)$ is called shift function with the necessary condition

$$\Delta G(\tau) \equiv \int d\omega K(\tau, \omega) s(\omega) < \infty \tag{7.66}$$

Then the shifted correlator can be defined in a natural way as

$$G_s(\tau) = G(\tau) + \Delta G(\tau) \tag{7.67}$$

and MEM is performed for G_s. Once the Maximum Entropy Method result for the positive spectral function ρ_s is found, the shift function is substracted again and the true spectral function is obtained.
Obviously the shift function is a second input besides the model function, that can in principal influence the spectral image. Therefore, it is necessary to check the magnitude of the shift-function dependence for any results. This generelisation of standard-MEM will in the following be called extended-MEM.

8 Gluon spectral functions

'In science, all new discoveries start with someone murmuring "Huh,... that's strange!"'

Isaac Asimov

Here, the results for the gluon spectral functions are presented. Both the high temperature limit and the extrapolation to zero temperature is discussed. Further, the importance of the violation of posivity is demonstrated by comparing the gluon spectral functions obtained with extended-MEM to those obtained by standard-MEM, i.e. positive definite spectral functions.

8.1 MEM input correlators

8.1.1 finite temperature gluon propagators

Within this thesis euclidean, Landau gauge gluon propagators at finite temperature are employed as input for extended-MEM. At finite temperature the gluon propagator is given in terms of two scalar functions, the chromoelectric mode $G_L(q)$ and the chromomagnetic mode $G_T(q)$. The chromoelectric mode is longitudinal with respect to the spatial momentum, while the chromomagnetic mode is transverse with respect to the spatial momentum. Naturally, both modes are 4-d transverse, obeying the Slavnov-Taylor identities. In Landau gauge, the finite temperature gluon propagator can be written as:

$$G^{ab}_{\mu\nu}(q) = \delta^{ab}\left(P^L_{\mu\nu}(q)G_L(q) + P^T_{\mu\nu}(q)G_T(q)\right) \tag{8.1}$$

with the longitudinal and transverse polarization tensors

$$P^T_{\mu\nu}(q) = (1-\delta_{\mu 0})(1-\delta_{\nu 0})\left(\delta_{\mu\nu} - \frac{q_\mu q_\nu}{\vec{q}^2}\right) \tag{8.2}$$

$$P^L_{\mu\nu}(q) = \delta_{\mu\nu} - \frac{q_\mu q_\nu}{q^2} - P^T_{\mu\nu}(q) \tag{8.3}$$

The input for extended-MEM, the chromomagnetic and chromoelectric modes in pure SU(3) gauge theory are obtained by means of the Functional Renormalization Group. Such calculations are performed in euclidean space and yield the Matsubara propagators with a discretized zero-component in momentum space (see, Section 4.2). Therefore, for each Matsubara mode the propagator can be understood as a function of spatial momentum. The extra label for the n-th mode is denoted as $G_{T/L}(n, \vec{q})$. For convenience, the label for the zero mode is dropped, such that $G_{T/L}(0, \vec{q}) \equiv G_{T/L}(\vec{q})$. In Fig.8.1 and Fig.8.2 the zero Matsubara modes of the longitudinal and transverse gluon propagator are shown for different temperatures as functions of spatial momentum. For comparison, lattice results for the respective temperatures are shown as well. The details about the calculational method and tools are found in [180]. In particular the

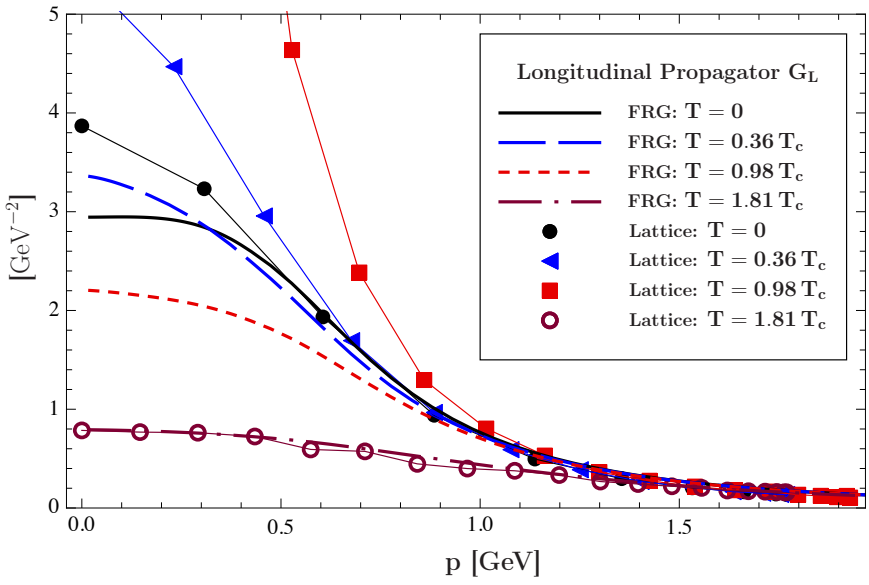

Figure 8.1: Zero Matsubara mode of the longitudinal gluon propagator $G_L(p)$ at different temperatures as a function of spatial momentum.

behaviour of the gluon propagators at low momentum is of interest. Clearly, both for FRG and lattice propagators, the seond derivative is negative in this region. This already requires, that the corresponding spectral function violates positivity. [181, 182].

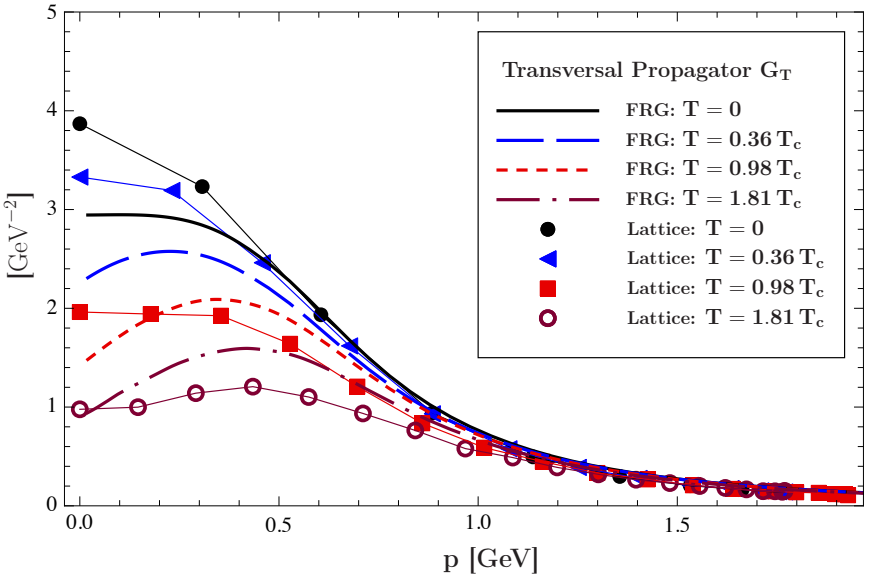

Figure 8.2: Zero Matsubara mode of the transverse gluon propagator $G_T(p)$ at diffepropertyrent temperatures as a function of spatial momentum.

8.1.2 Zero-mode approximation

It turns out, that the higher Matsubara modes $G_{T/L}(n \neq 0, \vec{q})$ are well-approximated by the zero mode:

$$G_{T/L}(n, \vec{q}) \approx G_{T/L}(\sqrt{\omega_n^2 + \vec{q}^2}) \tag{8.4}$$

with the n-th (bosonic) matsubara frequency ω_n defined in (4.20). The actual accuracy of the approximation (8.4), is studied in Fig.8.3 for transverse gluons at $T = 1.44\,T_c$ and in Fig.8.4 for longitudinal gluons at $T = 1.44\,T_c$. The black lines show the zero

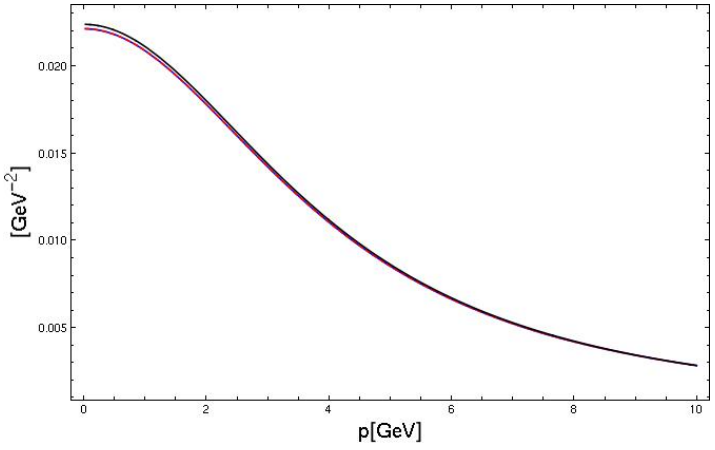

Figure 8.3: Test of the validity of equation (8.4) for the transverse gluon propagator at $T = 1.44\,T_c$. The black, blue and dashed red lines show the zeroth, first and second Matsubara mode.

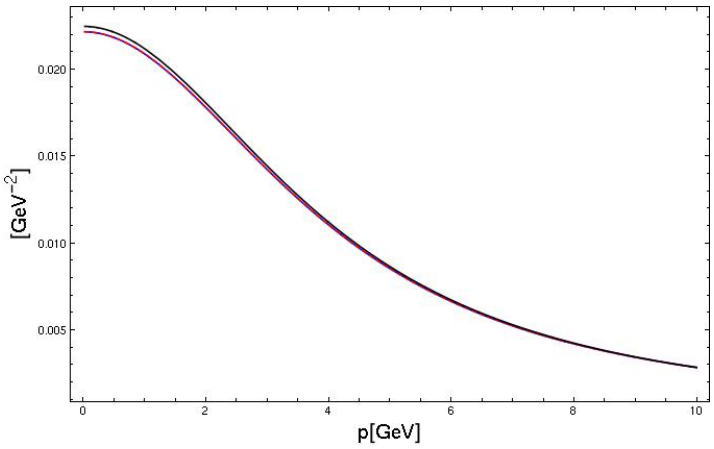

Figure 8.4: Test of the validity of equation (8.4) for the longitudinal gluon propagator at $T = 1.44\,T_c$. The black, blue and dashed red lines show the zeroth, first and second Matsubara mode.

mode, which shows a slight deviation from the first and the second mode at low spatial momenta of the order of 1%. The quality of the approximation slightly decreases with temperature. However, at the highest available temperature $T = 4.7\,T_c$ the approximation is still well within 1.5% at the largest deviation.

Even though, the zero mode approximation is quantitatively justified for the propagator, the dependence on derived quantities must be studied as well. It is well known, that e.g. the zero crossings of the Schwinger function sensitively depend on the propagator [183].

8.1.3 Matsubara imaginary time functions

In order to employ the propagators as input for extended-MEM (see equation (7.1)) the partial the Fourier transformation

$$\hat{G}_{T/L}(\tau, \vec{p}) = T \sum_{n=-\infty}^{\infty} e^{-i\omega_n \tau} G_{T/L}(n, \vec{p}) \tag{8.5}$$

with respect to the frequency/imaginary-time component is performed. Note, that $\hat{G}_{T/L}(\tau, \vec{p})$ is real, as $G_{T/L}(-n, \vec{p}) = G_{T/L}(n, \vec{p})$. Thus:

$$\hat{G}_{T/L}(\tau, \vec{p}) = T \sum_{n=-\infty}^{-1} e^{-i\omega_n \tau} G_{T/L}(n, \vec{p}) + T\, G_{T/L}(\vec{p}) + T \sum_{n=1}^{\infty} e^{-i\omega_n \tau} G_{T/L}(n, \vec{p}) \tag{8.6}$$

$$= T\, G_{T/L}(\vec{p}) + T \sum_{n=1}^{\infty} \left(e^{-i\omega_n \tau} + e^{i\omega_n \tau}\right) G_{T/L}(n, \vec{p}) \tag{8.7}$$

$$= T\, G_{T/L}(\vec{p}) + 2\, T \sum_{n=1}^{\infty} \cos(\omega_n \tau)\, G_{T/L}(n, \vec{p}) \tag{8.8}$$

For the extended-MEM reconstruction the dependence of (8.5) on the spatial momentum is merely parametric, in the sense that, for each fixed value of $p = |\vec{p}|$ there is a Matsubara imaginary time function $\hat{G}_{T/L}(\tau)$ as in (4.19).
In principle, all Matsubara modes are needed for the Fourier transform. The approximation (8.4), however, allows to perform the Fourier transformation with the zero mode only according to:

$$\hat{G}_{T/L}(\tau, \vec{p}) = T\, G_{T/L}(\vec{p}) + 2\, T \sum_{n=1}^{\infty} \cos(\omega_n \tau)\ , G_{T/L}(\sqrt{\omega_n^2 + (\vec{p})^2}) \tag{8.9}$$

This leads to the complication, that the FRG (or lattice) input, given in the momentum interval $[0, p_{max}]$ with $p_{max} = 35\text{GeV}$ must be extrapolated to arbitrary large spatial momenta. Fortunately, the UV-behavior is known from perturbation theory, and is given by

$$G_{pert}(p) \sim \tfrac{1}{p^2} \left[\text{Log}\left(\frac{p^2}{\mu^2}\right)\right]^{-\frac{13}{22}} \tag{8.10}$$

for $p \to \infty$. For the extrapolation, a continuous join of the perturbative curve to the Matsubara propagator is reached, by matchting the value of $G_{pert}(p)$ to the Matsubara propagator at the scale $p_{scale} \gg 1$. This corresponds to introducing the extrapolation propagator

$$G_{ext,L/T}(p) = \lambda_{L/T}(p_{scale})\, G_{pert}(p) \tag{8.11}$$

with the matching coefficient

$$\lambda_{L/T}(p_{scale}) = \frac{G_{L/T}(p_{scale})}{G_{pert}(p_{scale})} \tag{8.12}$$

The scale is chosen at $p_{scale} = 25GeV$ which lies deep in the perturbative region, and therefore cannot affect any non-perturbative properties of the propagator. In Fig.8.5 the extrapolation propagator is shown for the transverse gluon propagotor at $T = 1.44\,T_c$ (dashed blue). It it matched to the input propagator (red) at p_{scale}. Clearly, both propagators show the same functional dependence, such that the the extrapolation will approximately be smooth. The extrapolated gluon propagator for arbitrary momenta

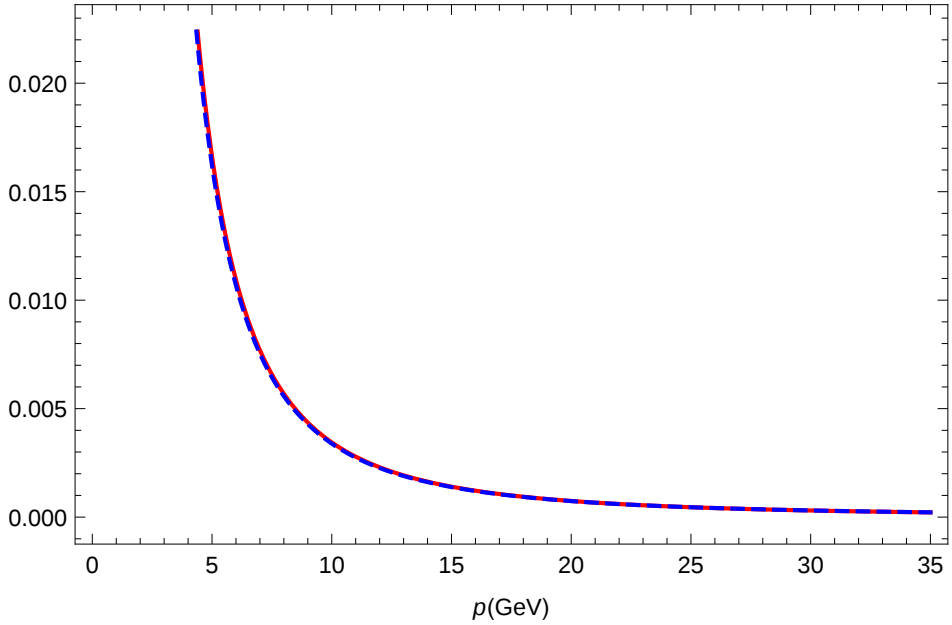

Figure 8.5: Transverse gluon propagator at $T = 1.44\,T_c$ (red) and the extrapolation propagator, with the scale fixed at $p = 25GeV$ (dashed blue).

is defined as:

$$G_{L/T}(p) = \begin{cases} G_{data,L/T}(p) & : p < p_{scale} \\ G_{ext,L/T}(p) & : p \geq p_{scale} \end{cases}$$

With the extrapolated zero mode of the gluon propagator, the Matsubara imaginary time function $\hat{G}_{T/L}(\tau, p)$ can now be calculated. In Fig.8.6 $\hat{G}_T(\tau, p)$ is shown for various temperatures, whereas in Fig.8.7 the respective functions are shown for longitudinal gluons.

The imaginary time axis covers the interval $[0, \frac{\beta}{2})$ and thus captures the full range of independent values of $\hat{G}_{T/L}(\tau, p)$ (see, (4.18)). Note again, that for the spectral reconstruction, extended-MEM is employed for each slice with constant spatial momentum. Studying such a slice more carefully, from (8.8) it follows, that the zero mode contributes a constant to $G(\tau)$. Thus, all information about the shape of the spectral function is encoded in the $n \neq 0$ Matsubara modes. In particular, it follows, that in the limit $T \to \infty$, where the higher mode contributions decrease relative to the zero

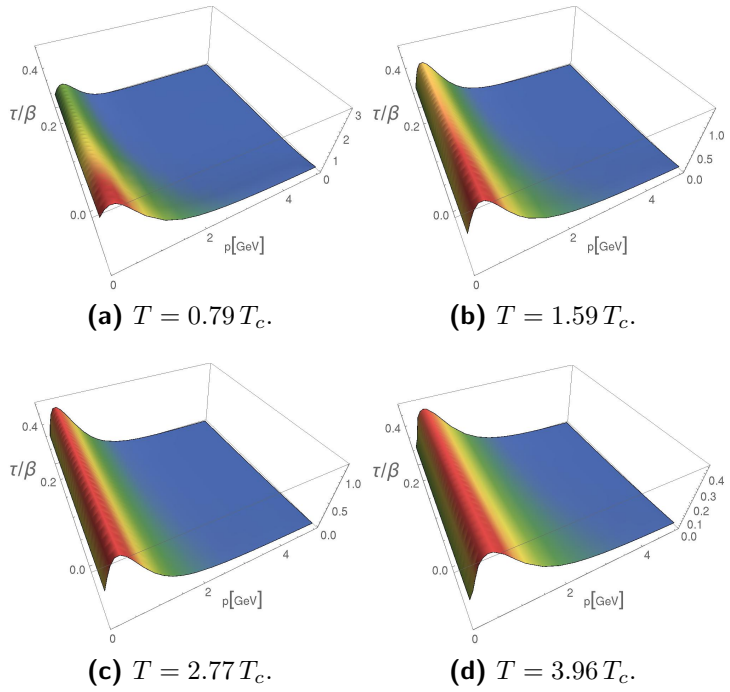

(a) $T = 0.79\,T_c$. **(b)** $T = 1.59\,T_c$.

(c) $T = 2.77\,T_c$. **(d)** $T = 3.96\,T_c$.

Figure 8.6: Thermal dependence of the transverse gluon Matsubara imaginary time function.

mode, the systematic errors of MEM will increase. Fig.8.6(d) and Fig.8.7(d) already indicate, that the main contribution to the Matsubara function is the constant from the zero mode. For Fig.8.6(d) the difference between $\hat{G}(\tau = 0, 0)$ and $\hat{G}(\tau = \frac{\beta}{2}, 0)$ is 5%. This means, that the actual relevant information is small compared to the constant 'background', and will be even more suppressed by the extended-MEM shift. Therefore, it will be interesting to see, how well extended-MEM can reconstruct the spectral functions of these high temperature propagators.

8.1.4 On systematic errors

For the discussion of systematic errors of the spectral functions, the systematic errors of the input correlators are studied. An obvious systematic error arises from the zero-mode approximation (8.4). Above, the accuracy in momentutm space was already discussed. However, a Fourier transform can amplify the errors.

In Fig. 8.8 the Matsubara function for the transverse gluon at $T = 1.44\,T_c$ is shown. Diagram (a) is obtained with the the zero mode approximation, while diagram (b) employs the Matsubara modes up to $n = 2$, and uses the zero-mode approximation for $n > 2$. There is no immediately visible difference to be observed. Nevertheless, it is of interest to see what quantivative difference is imprinted in the Matsubara function

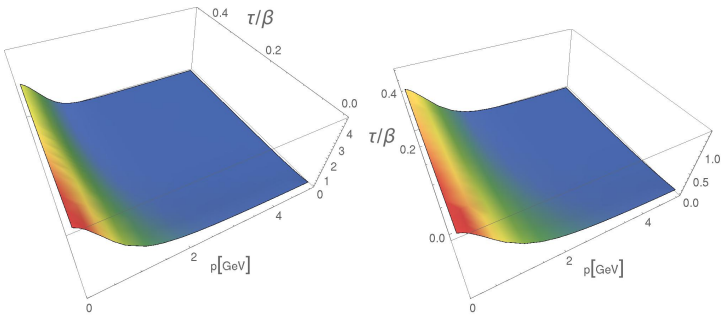

(a) $T = 0.79\,T_c$.

(b) $T = 1.59\,T_c$.

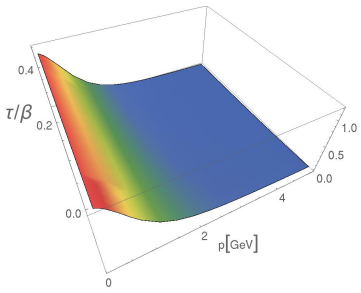

(c) $T = 2.77\,T_c$.

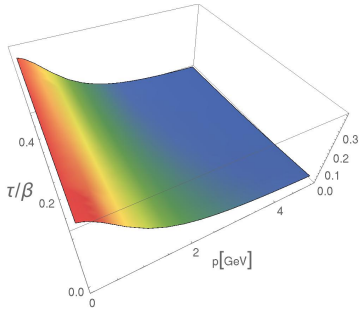

(d) $T = 3.96\,T_c$.

Figure 8.7: Thermal dependence of the longitudinal gluon Matsubara imaginary time function.

by the zero mode approximation. In particular, as the constant part of the Matsubara function is the same for (a) and (b), the relevant difference should be studied for the Matsubara functions with the constant part substracted. Therefore, the difference, normalized to the Matsubara function in diagram (a) with constant part substracted

$$\Delta G(\tau, p) = \frac{|G_0(\tau, p) - G_2(\tau, p)|}{\bar{G}_0(\tau, p)} \tag{8.13}$$

is shown in Fig.8.9. For fixed p the difference grows when τ is increased. That is in agreement with the observation, that the deviation of the higher modes from (8.4) is largest for small frequencies. The Fourier transform encodes the small frequency behaviour of the propagator in the large τ behaviour of the Matsubara function.
Thus, the small frequency resolution of the spectral function suffers from the zero mode approximation. Consequently, in this thesis, the improved zero-mode approximation is used, such that, the approximation is applied only for $n > 2$.
Further, the relative difference grows with increasing p. At $p = 4$GeV the deviation reaches 5% at $\tau = \frac{\beta}{2}$. Beyond, the deviation is growing fast. Here, spatial momenta are considered for $0 \leq p \leq 15\,T$. For $T = 1.44\,T_c$ the maximum momentum is $p_{max} = 5.7$GeV. Thus, the large p behavior of the spectral function has to be treated

with some care, even though the improved zero-mode approximation will strongly reduce this systematic effect. Generally, the growing of the difference between zero mode approximation and the improved approximation rises at $p \sim 12T - 15T$. The effect of including even higher modes in the transform (8.5) will probably not be of quantitative relevance, Nevertheless, the largest systematic error of the spectral function due to the improved zero mode approximation is expected at the low frequency behaviour at large spatial momenta.

Another source of systematic errors is, of course, the systematic error of the gluon

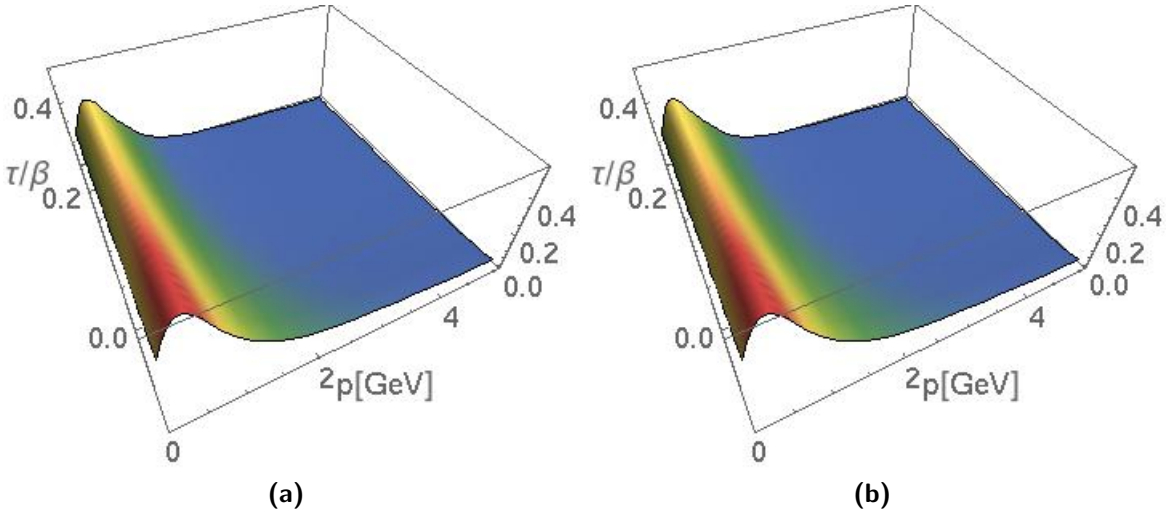

Figure 8.8: Matsubara imaginary time functions for transverse gluons at $T = 1.44\,T_c$ for the zero mode apprimation (a) and the improved zero mode approximation (b).

propagators. They are judged in this thesis, by comparing the MEM spectral functions obtained from gluon propagators of both lattice and FRG.

8.2 Model function and shift function

In this section, the model functions $m(\omega)$ and shift functions $s(\omega)$ used in the extended-MEM reconstruction of the gluon spectral functions are introduced. In principle, these functions can be chosen seperately for each slice of the spatial momentum. However, here, they are chosen independent of the spatial momentum. The justification is, that only the perturbative behaviour for large frequencies will be encoded in both model and shift function, in order to not overly restrict the spectral function. The large frequency behaviour of the spectral function, however, is approximately p-independent.

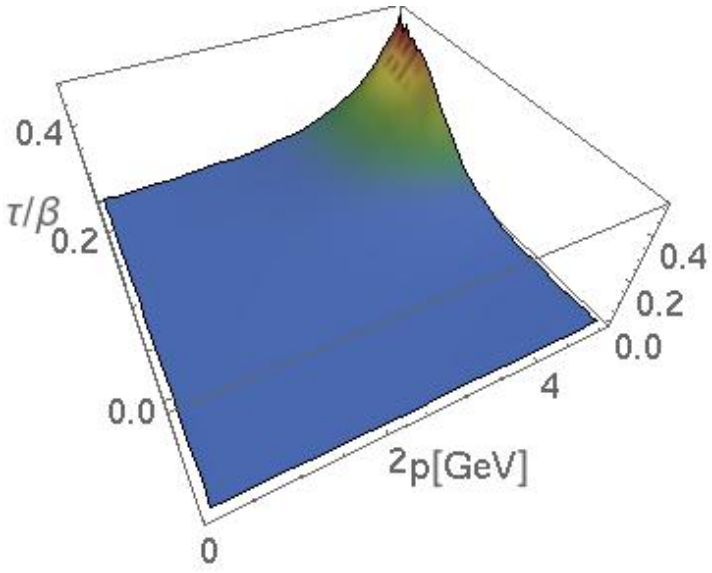

Figure 8.9: The difference of the Matsubara functions in Fig.8.8 normalized with respect to Fig.8.8 (a) subracted by the constant zero-mode contribution.

8.2.1 Model function

In order to find a suitable model function, it is helpful to consider a situation, where no prior information is available. What is the model function, encoding this in MEM? The answer is, that without prior information the introduction of the entropy term in (7.20) is obsolete. The limit of no prior information is $\alpha \to 0$ and results in the naive approach introduced in Section 7.2. This just reflects the original problem of image reconstruction from incomplete data sets.

But the intention of the question of no prior information usually is meant differently: Which model function imposes the least contraints on the spectral function? The answer to this question, is that a constant model function $m(\omega) = \omega_0$ only imposes smoothness on the spectral function. Thus, adding prior information results in deforming the model function from a constant function. In particular, here, the perturbative behaviour is known [184]:

$$\rho_{pert}(\omega) \sim -\frac{1}{\omega \left[\mathrm{Log}\,(\omega)\right]^{35/22}} \tag{8.14}$$

Clearly, the perturbative tail of the gluon spectral function is negative. Such a negative tail cannot be incorporated in the model function, which is assumed to be positive (see the discussion in Section 7.9). This, however, was expected and led to the introduction of extended-MEM in the first place.

The negative tail is shifted by a shift function $s(\omega)$ with the correct asymptotics, assuming $|s(\omega)| > |\rho(\omega)|$ for the asymptotic tail $\omega > \omega_0$, which is an necessary condition for the shift function. Then, the shifted spectral function exhibits a positive tail, with the asymptotic decay:

$$\rho_{shifted,pert}(\omega) \sim \frac{1}{\omega \left[\mathrm{Log}\,(\omega)\right]^{35/22}} \tag{8.15}$$

This behaviour is imprinted on the model function as:

$$m(\omega) = m_0\,\Theta(\omega_0 - \omega) + \left(m_0 \frac{1}{\frac{\omega}{\omega_0}\left[\frac{\mathrm{Log}(\omega)}{\mathrm{Log}(\omega_0)}\right]^{\frac{35}{22}}} \right) \Theta(\omega - \omega_0) \tag{8.16}$$

The two parameters, namely m_0 (normalization) and ω_0 (begin of asymptotic tail) can be varied to test the influence of the model function on the extended-MEM spectral function. For the step function $\Theta(x)$ a smooth representation is chosen:

$$\Theta_k(x) = \frac{1}{1 + e^{-2kx}} \tag{8.17}$$

Further, the parameters of the model function are both temperature and polarization dependent. In Fig.8.10 the generic shape of the model function (8.16) is shown in

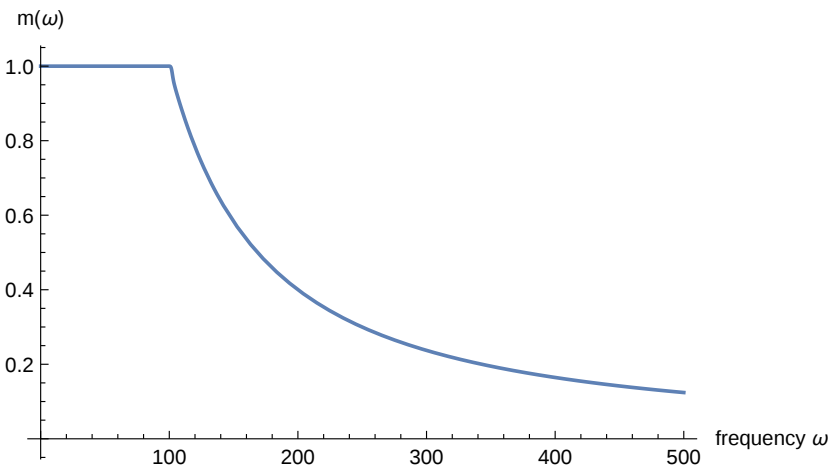

Figure 8.10: Generic form of the extended-MEM model function employed for the reconstruction of finite temperature gluon spectral functions in arbitrary units.

arbitrary units. The sharpness of the onset of the asymptotic decay can be regulated by $\Theta_k(x)$.

8.2.2 Shift function

The asymptotic behavior of the shift function was already discussed in the preceeding section. Otherwise the shift function is arbitrary with the constraints of minimality and finiteness discussed in Section 7.9. For the shift function three parameters are introduced. The maximum value s_0 (note, that $s(\omega)$ is defined positive in (7.65)) and two scale parameters ω_0, ω_1 at which the asymptotic tail and the decay towards $\omega \to 0$ starts, respectively. Further, the choice of the decay law towards $\omega = 0$ introduces a degree of freedom in the shift function.
The shift function used throughout this thesis for gluon spectral functions reads:

$$s(\omega) = h(\omega)\Theta(\omega_1 - \omega) + s_0\,\Theta(\omega - \omega_1)\Theta(\omega_0 - \omega) + \left(s_0 \frac{1}{\frac{\omega}{\omega_0}\left[\frac{\mathrm{Log}(\omega)}{\mathrm{Log}(\omega_0)}\right]^{\frac{35}{22}}} \right) \Theta(\omega - \omega_0) \quad (8.18)$$

with the requirements $\omega_0 > \omega_1$ and $h(\omega_1) = s_0$. A generic representation is shown in Fig. 8.11 for $h(\omega) = s_0 \left(\frac{\omega}{\omega_1}\right)^2$. The shift (7.66) of the Matsubara function for

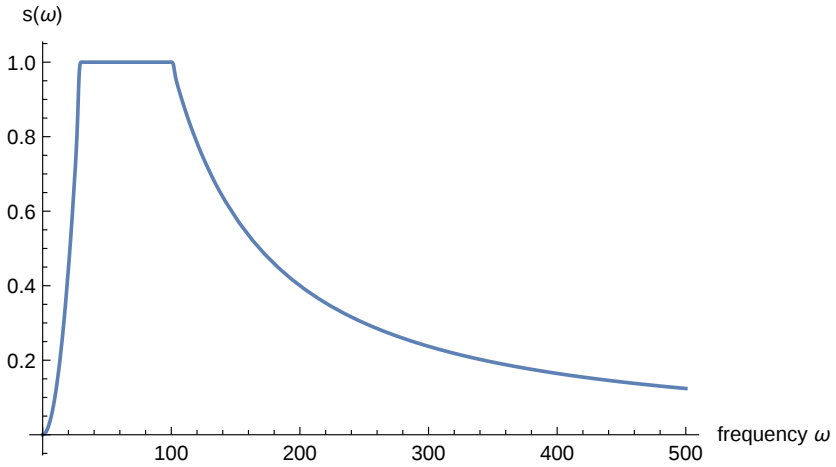

Figure 8.11: Generic form of the extended-MEM shift function employed for the reconstruction of finite temperature gluon spectral functions in arbitrary units.

$s_0 = 1$, $\omega_0 = 20$ and $\omega_1 = 1$ is shown in Fig.(8.12). Note, that $\Delta G(\tau)$ is convex everywhere, indicating a positive spectral function. To reduce the parameter space, a natural choice for the normalisation of the model function is $m_0 = s_0$. Also, the onset of the asymptotic tails for both model and shift function are chosen identical.
In conclusion, there are 3 input parameters from the prior knowledge: the maximum shift s_0, the decay scale ω_1 of the shift function and the onset of the asymptotic tail ω_0. In addition the precise form of the decay law towards vanishing frequency can be

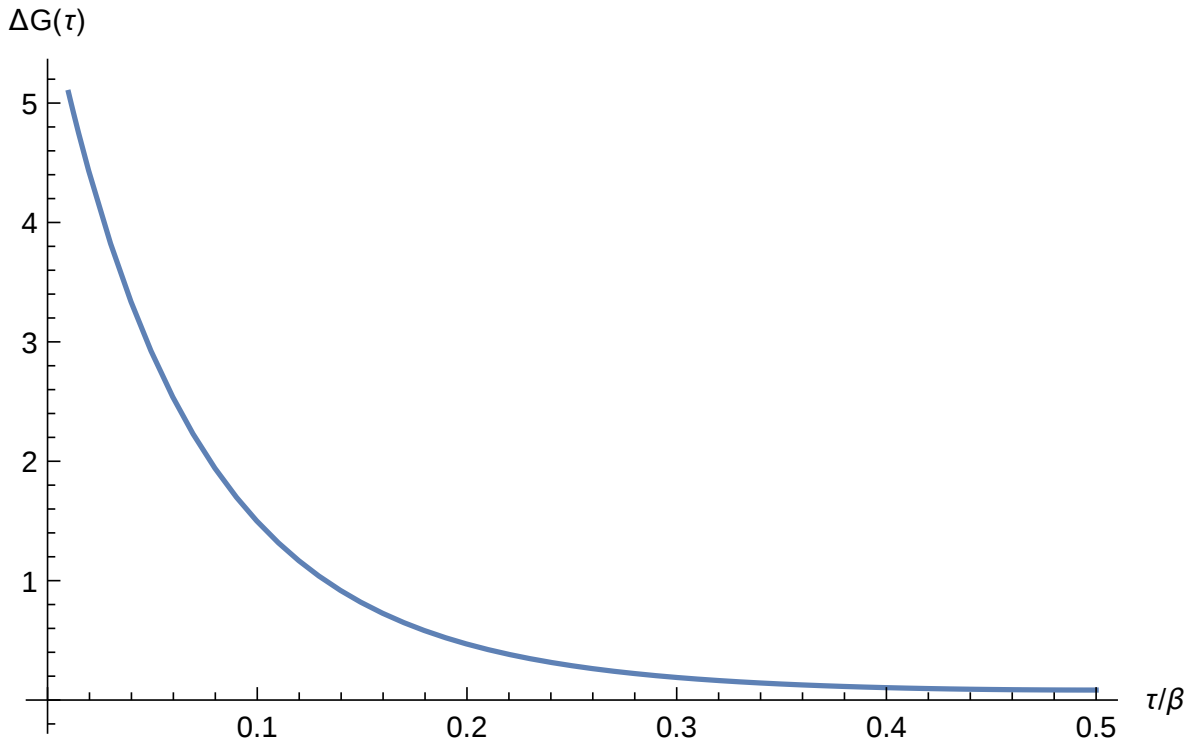

Figure 8.12: Shift of the Matsubara function $G(\tau)$, due to the shift function $s(\omega)$.

chosen freely (as long as (7.66) holds). In this thesis both algebraic and exponential decays were employed. However, the spectral functions were remarkably insensitive on the precise form.

8.3 Finite temperature gluon spectral functions

8.3.1 Simulation setup

Here, the extended-MEM results for the finite temperature gluon spectral functions are presented. For each temperature T, $N_p = 30$ independent extended-MEM simulations were performed for the spatial momenta $p_n = 0.5\,T(n-1)$ with $(n = 1, ..., 30)$. Thus, for all temperatures the momentum range $0 \leq \frac{p}{T} \leq 14.5$ is covered.

Further, the Matsubara functions (8.5) were calculated at $N_\tau = 40$ points in the interval $\tau = [0, \frac{\beta}{2})$, using a linear grid. The frequency was discretized on a linear grid with $N_{\omega,lin} = 1000$ in the interval $0 \leq \frac{\omega}{T} \leq 20$. To reliably fix the asymptotic behaviour, a logarithmically spaced grid extends the linear interval to $\omega_{max} = 10^6$. Here, $N_{\omega,log} = 200$ was chosen.

The normalisation s_0 of the shift function was chosen p-independent, such that, the shifted Matsubara correlator (7.67) is convex as a function of frequency for all (fixed) spatial momenta. To achieve this, s_0 was set to an initial (small) value. Then it was increased in stepwise until the shifted correlator exhibited convexity. This procedure was a trade-off between allowing extended MEM to scan as much of the function space as possible, and not supressing the actual data by adding a too large shift (be reminded of the discussion of constant off-sets of the Matsubara correlators at high temperatures in Section 8.1.3).

An expamle of a typical shift is shown in Fig.8.13. In diagram (a) the unshifted trans-

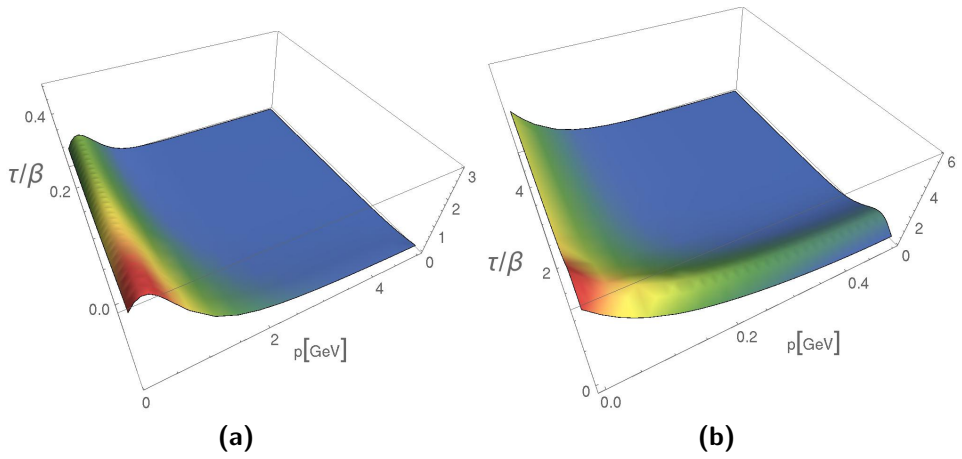

Figure 8.13: Example for the effect of a propagator shift for the transverse gluon propagator at $T = 0.77\,T_c$. In diagram a.) the unshifted Matsubara function is shown. In diagram b.) the shift is added. The shifted Matsubara function is convex as a function of frequency.

verse gluon Matsubara correlation function at $T = 0.77\,T_c$ is shown for comparison. The function in diagram (b) is obtained by minimally shifting the Matsubara function as explained above. In particular for larger spatial momenta, the shift is substantially larger than the data. This, however, does not seems to affect the extended-MEM re-contruction, so that after re-substraction of the the shift function, the spectrum will reliably be recontructed.

For the onset of the asymptotic decay of both model and shift function $\omega_0 = 15\,T$ is chosen, while for the IR decay scale of the shift function $\omega_1 = 0.5\,T$ is chosen. Both parameters were varied to study their dependence on the extended-MEM results.

8.3.2 Spectral functions of transverse gluons

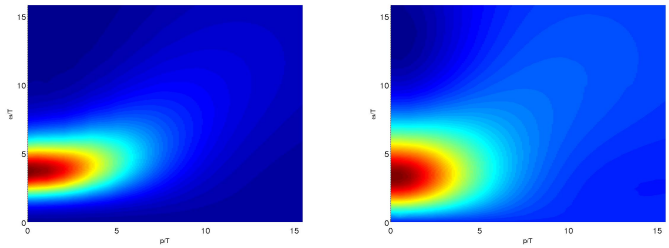

(a) $T = 0.39\,T_c$.

(b) $T = 2.35\,T_c$.

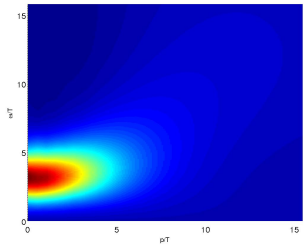

(c) $T = 0.78\,T_c$.

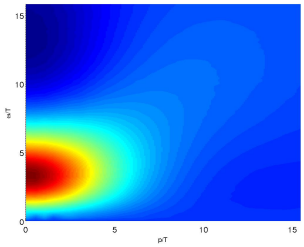

(d) $T = 2.75\,T_c$.

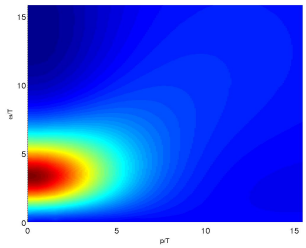

(e) $T = 1.57\,T_c$.

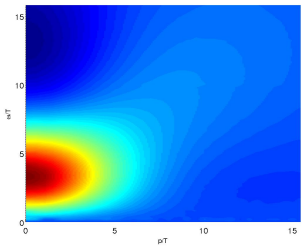

(f) $T = 3.53\,T_c$.

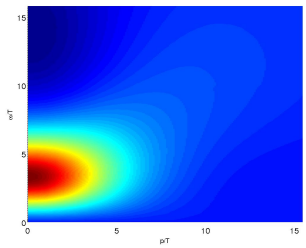

(g) $T = 1.96\,T_c$.

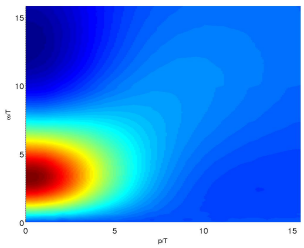

(h) $T = 3.92\,T_c$.

Figure 8.14: Thermal dependence of transverse gluon spectral functions.

In Fig.8.14 the transverse gluon spectral functions are shown for various temperatures. The axes are scaled in units of temperature. This allows to directly study the non-trivial temperature scaling. All spectral functions show common features:
For small spatial momenta the spectral functions exhibit an approximately p-independent maximum at $\omega = 2.8\,T$. Towards larger momenta the height of the maximum smears

out and bends towards the diagonal $\omega = p$. Further, there is a region where the spectral functions are negative (darkest blue region). This region is found in all gluon spectral functions at larger frequencies than the maxiumum peak. The violation of positivity seems to inhibit the bending of the central peak towards the main diagonal for low to intermediate momenta. To understand this better, observe the spectral function in Fig.8.15 a.). It shows the transverse gluon spectral function at $T = 1.96\,T_c$ from a different angle. Further the region, where the spectral function assumes negative values is colorcoded in violet (darker violet represents lower values). In diagram b.) a transverse gluon spectral function at $T = 1.44\,T_c$ is shown in the dynamical quasi-particle model [185]. In a quasi-particle model (DQPM), the spectral function is a priori positive. Clearly, the peak is sharper and the bending of the peak already sets in at lower spatial momenta, while the qualitative behavior is similar to the extended-MEM results. In diagram c.) a lower resolution standard-MEM reconstruction of the transverse gluon spectral function at $3.5\,T_c$ is shown, where the extension of MEM to non-positive spectral function was not used. The reconstructed spectral function remarkably well reproduces the features of the DQPM spectral function. This suggests that the violation of positivity has an important impact of the structure of the spectral function. The quasi-particle model seems not to cover all features of gluon spectral functions in the vicinity of the crititcal temperature. In particular, the extended-MEM spectral functions are broader compared to both the DQPM spectral function and the standard-MEM result for an a priori positive spectral function.

The extended-MEM results are remarkably stable to small variations of the extended-MEM setup. The normalization of the model function has no impact on the spectral function, whereas, slight changes of the position of the zero crossings are observed, when the onset of the asymptotic tail is varied. Changing the onset for transverse gluons at $T = 1.96\,T_c$ for $p = 0$ from $\omega_0 = 15$ to $\omega_0 = 10$, resulted in a change of the position of the zero-crossing by 5% towards lower frequency, whereas, a variation to $\omega_0 = 20$ only changed the zero-crossing by 0.5% towards larger frequencies. This finding suggests, that a too early asymptotic onset can have a systematic effect of the reconstructed spectral function. This is expected, as the entropy term punishes a deviation of the spectral function from the model function. If the asymptotic tail in the model function sets in before it is present in the spectral function, extended-MEM will find a trade-off between model and input data, that systematically pushes the spectral function towards the model.

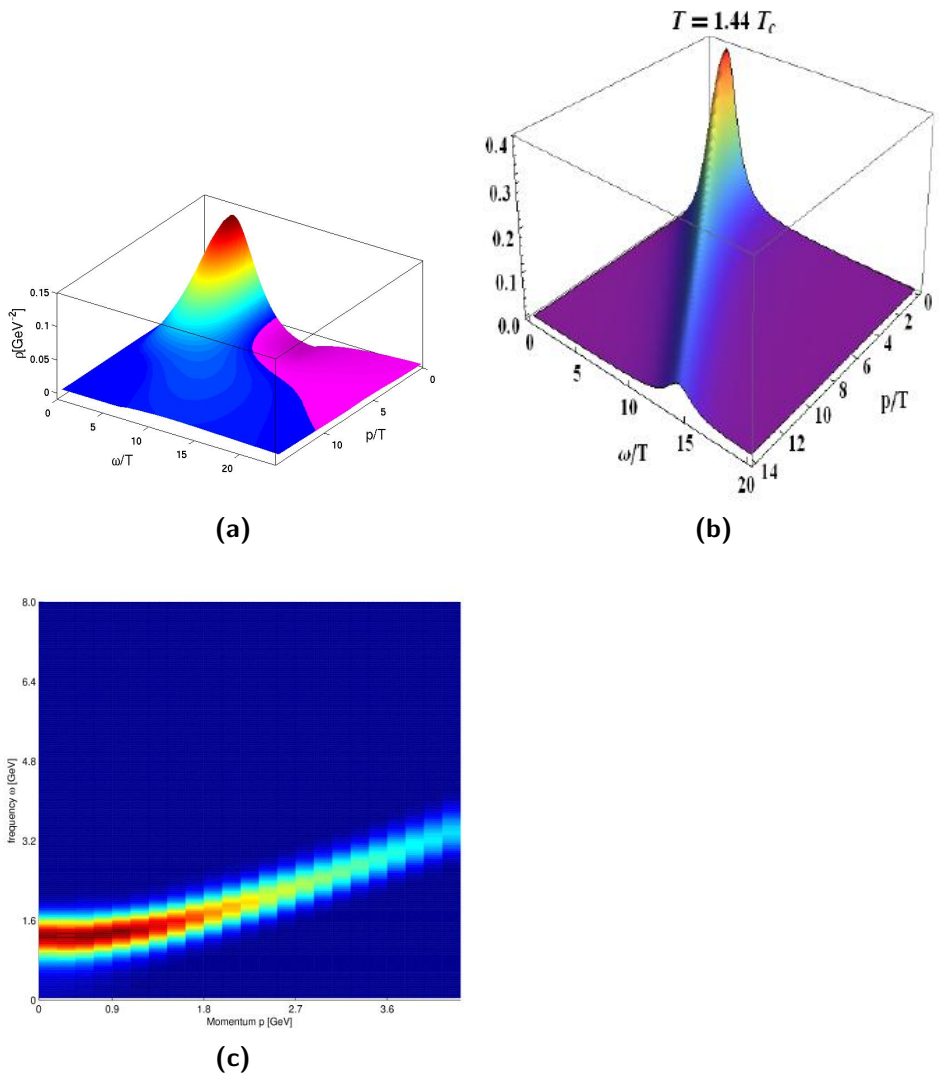

Figure 8.15: Extended-MEM transverse gluon spectral function at $T = 1.96\,T_c$ (a) from an angle that shows the bending of the peak. Further, the violation of positivity is colorcoded in violet for better visibility. Diagram (b) shows a model spectral function within the Dynamical quasi-particle model at $T = 1.44\,T_c$. The standard-MEM reconstruction of the transverse gluon spectral function at $T = 3.92\,T_c$ (c) shares the properties of (b).

Further it turned out, that the logarithmic grid for large frequencies had a stabilizing effect on the asymptotic tail of the spectral function. For a purely linear grid, either more data points were neccesary, to cover a sufficiently large interval, at the cost of performance, or the resolution at intermediate frequencies suffered. A mixed linear/logarithmic grid was also succesfully used in [186] for the reconstruction of ultracold atomic spectral functions.

8.3.3 Zero temperature limit

Another interesting aspect of the gluon spectral functions is the limit $T \to 0$. It turnes out, that extended-MEM could not reconstruct spectral functions below $T \approx 100\text{MeV}$. In Fig.8.16 such a reconstruction is shown for $T = 0.18\,T_c$. The spectrum exhibits

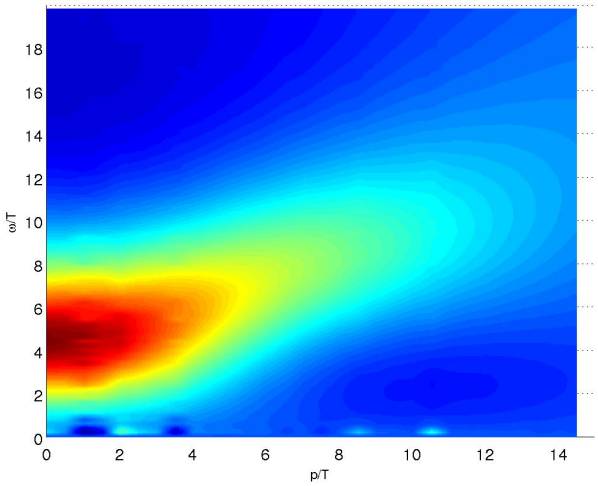

Figure 8.16: Extended-MEM reconstruction of the transverse gluon spectral function at $T = 0.18T_c$.

highly located structures at $\omega \approx 0$, which signal instabilities in the reconstruction. One reason for this behavior can be, that at zero temperature the spectral function is no longer analytic [187]. Maximum entropy reconstructions are known to become cumbersome in such cases [188, 189].
Nevertheless, the spectral function for the transverse gluon at $T = 0.39\,T_c$ already indicates, that the regime of almost linear T-scaling of the spectral function has been left. This can be seen, in the position of the maximum for zero spatial momentum. Clearly, there will be a non-zero freezeout temperature, below which the $T = 0$ limit is effectively reached. At this point, the position of the peak is no longer T-dependent. Thus in units of $\hat{\omega} = \omega/T$ the peak position will move to larger $\hat{\omega}$. This behaviour can be seen here. At $T = 0.39\,T_c$ the peak is at $\hat{\omega} = 4.1$ (compared to $\hat{\omega} \approx 2.8$ for larger temperature). Figure 8.17 visualizes this effect. It shows the $p = 0$ slices for different temperatures. The curves with maximum at $\hat{\omega} = 2.8$ correspond to temperatures $T = 0.72\,T_c ... 3.92\,T_c$. (from top to bottom). The remaining curve corresponds to $T = 0.39\,T_c$ with the shifted maximum.

It would be interesting to extract further information about the zero temperature spectral function from the available finite temperature extended-MEM results. In par-

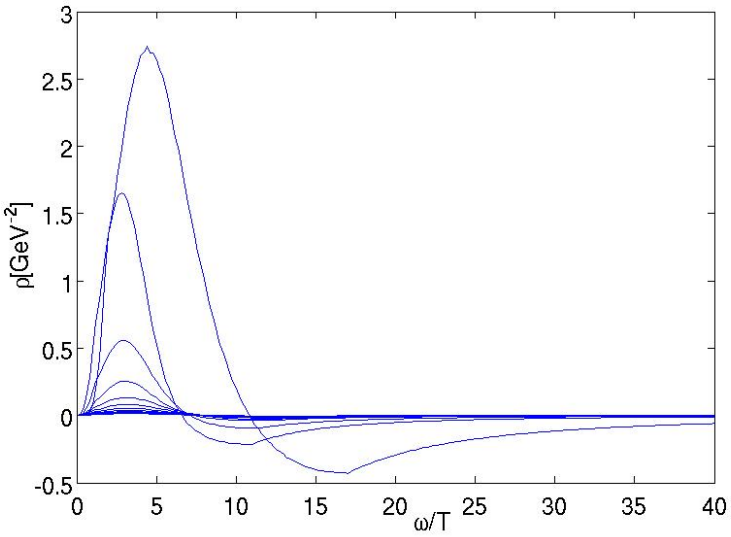

Figure 8.17: Transverse gluon spectral functions $\rho(\omega, p = 0)$ for $T = 0.39\,T_c ... T = 3.92\,T_c$. The maxima decrease with increasing temperature.

ticular, besides the maximum position, the position of the zero crossing, i.e. the scale at which the violation of positivity sets in, can be studied. In the zero temperature limit these position are expected to converge towards the same value. This was shown in a DSE framework in [187]. Fig.8.18, taken from this reference, shows the gluon spectral function in the zero temperature limit. Note, that for $T = 0$ the distinction between transverse and longitudinal tensor structure is obsolete, as there is no heat bath. Clearly, the non-analyticity, that was discussed above is visible in Fig.8.18. In the discussion of [187] the range for the position of the zero crossing is given by

$$\omega_c = 600\text{MeV} - 700\text{MeV}. \tag{8.19}$$

For the extended-MEM spectral functions, both minimum position and zero-crossing can be traced as a function of temperature. The respective results are found in Fig.8.19. Note, that the frequency axes is given in GeV. Once more, it becomes obvious, that the linear T-scaling of both maximum position (a) and zero crossing (b) is present even below the critical temperature. There seems to be a relatively sharp transition to the low temperature regime. At $T = 0.39\,T_c$ the zero crossing is found at $\omega_c = 1.1\text{GeV}$, while the maximum position is at $\omega_m = 0.41\text{GeV}$. It seems reasonable to assume, that towards the zero temperature limit, both values will converge to a value within this interval. Whether agreement with (8.19) would be made, cannot be deduced further from the available data, apart from the observation, that (8.19) is indeed contained in

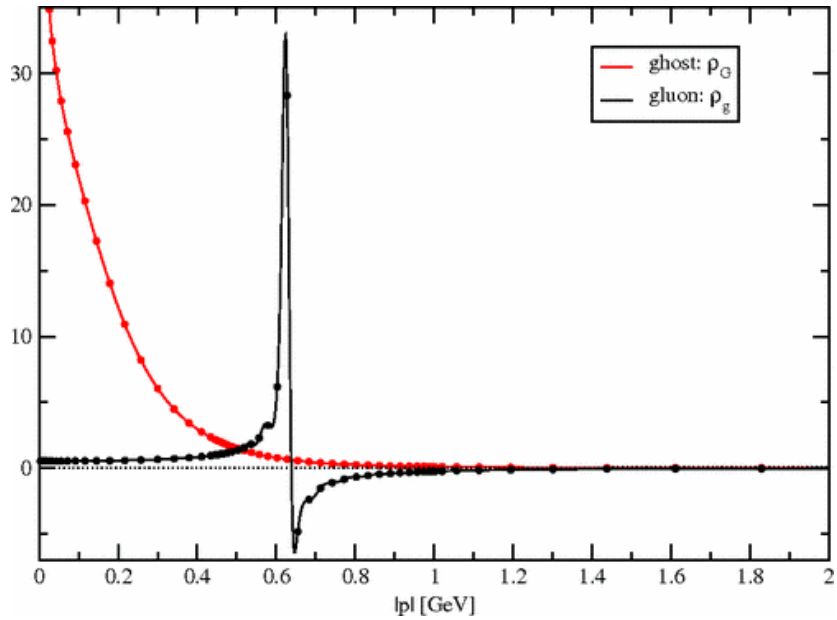

Figure 8.18: Zero temperature ghost and gluon spectral function from [187].

the rather large interval $[\omega_m, \omega_c]$.

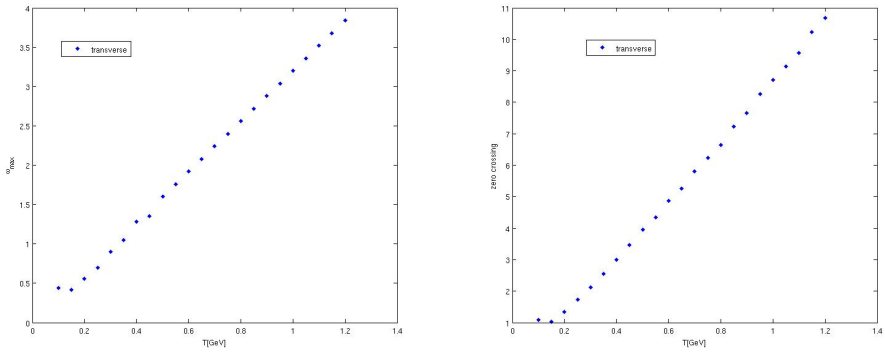

(a) **(b)**

Figure 8.19: Thermal dependence of the position of the maximum (a) and the zero crossing (b) of the transverse gluon spectral function $\rho(\omega, p = 0)$.

8.3.4 Limit of high temperatures

The opposite limit of high temperatures is of interest as well. Due to asymptotic freedom, gluons will become free (quasi-)particles in this limit. The quasi-particle, transverse gluon spectral function reads [132, 190]

$$\rho(\omega, p) = 2\pi\, Z(p)\, (\delta(\omega - \omega_D(p)) + \delta(\omega + \omega_D(p))) + \beta(\omega, p) \tag{8.20}$$

with the dispersion relation $\omega_D(p)$ and residue

$$Z(p) = \frac{\omega_D(p)\,(\omega_D^2(p) - p^2)}{3\omega_{pl}^2\omega_D(p) - (\omega_D^2(p) - p^2)^2} \tag{8.21}$$

in terms of the plasma frequency $\omega_{pl} = \frac{1}{3}g^2T^2$. Thus, HTL perturbation theory predicts a non-analytic spectral function with a spatial momentum dependent δ-pole. For the extended-MEM spectral functions, a narrowing of the peak towards larger temperatures cannot be found. A possible explanation can be, that the high temperature narrowing sets in at even higher temperatures, that were not available for the extended-MEM reconstruction. This, however, is in contradiction with common lore, that HTL resummed perturbation theory gives qualitatively accurate results for $T \approx 4\,T_c$ [191].

Another interpretation is the apparent problem of extended-MEM to reconstruct spectral functions in the high temperature regime, due to the suppression of information in the Matsubara imaginary time function. In Section 8.1.3 the dominance of the constant contribution from the zero-mode was discussed. Further, the developing non-analyticity in the high temperature gluon spectral function is certainly a cumbersome issue for extended-MEM in the first place. Nevertheless, it is interesting to see, whether the position of the peak of the extendend-MEM spectral functions agrees with (8.20). The dispersion relation $\omega_D(p)$ behaves for small spatial momentum $p \approx 0$ as [132]

$$\omega_D^2(p) \sim \omega_{pl}^2 + \frac{6}{5}p^2 \tag{8.22}$$

For the $T = 3.92\,T_c$ and the zero temperature running coupling evaluated at scale T, the plasma frequency in units of temperature is $\omega_{pl} = 2.53$. This agrees reasonably well with Fig.8.14(j). This suggests, that extended-MEM at high temperatures suffers from a systematic over-broadening of the spectral functions, which has been observed before [80]. Nevertheless, the position of the peak is a gauge-invariant information, as it corresponds to the pole of the retarded propagator, which extended-MEM seems to reconstruct reliably even in the high temperature regime.

8.4 Longitudinal gluon spectral function

To conclude the discussion of gluon spectral functions, the longitudinal spectral functions are presented. Fig.8.20 show the thermal dependence of the longitudinal gluon

spectral functions. While the qualitative features are similar to the transverse spectral functions of Fig.8.14, there are also differences. The peak position at zero spatial momentum is assumed at slightly larger frequency ($\omega^L_{peak} \approx 3.2\,T - 3.5\,T$, compared to $\omega^T_{peak} \approx 2.8\,T$).

Further, it is interesting to study the violation of positivity of both longitudinal and

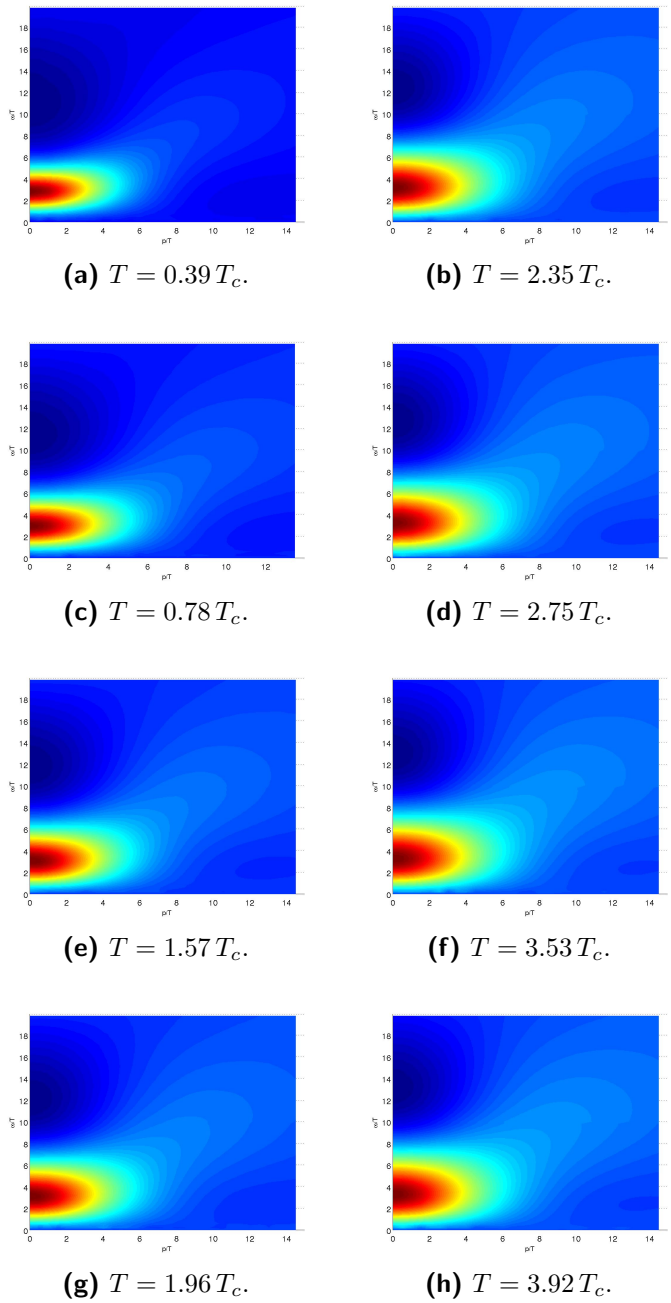

(a) $T = 0.39\,T_c$. **(b)** $T = 2.35\,T_c$.

(c) $T = 0.78\,T_c$. **(d)** $T = 2.75\,T_c$.

(e) $T = 1.57\,T_c$. **(f)** $T = 3.53\,T_c$.

(g) $T = 1.96\,T_c$. **(h)** $T = 3.92\,T_c$.

Figure 8.20: Thermal dependence of longitudinal gluon spectral functions.

transverse gluons. The degree of positivity violation is measured by the ratio $|\frac{\rho_{max}}{\rho_{min}}|$, where ρ_{max} and ρ_{min} denote maximum and minimum of the spectral function. Fig.8.21 shows the thermal evolution for transverse and longitudinal gluons. Both polarizations show a qualitatively similar increase of the ratio towards higher temperatures until a saturation sets in and the ratios remain constant. However, the interpretation, that high temperature gluons show a stronger violation of positivity would not be correct. The region of a negative spectral function merely gets more located compared to the maximum peak. Fig.8.14 and Fig.8.20, show, that the positive peak broadens over-proportional to T, while the negative dip does not.
Below T_c, the curves in 8.21 show a different behaviour, even though towards $T \to 0$, they seem to converge again, as expected.

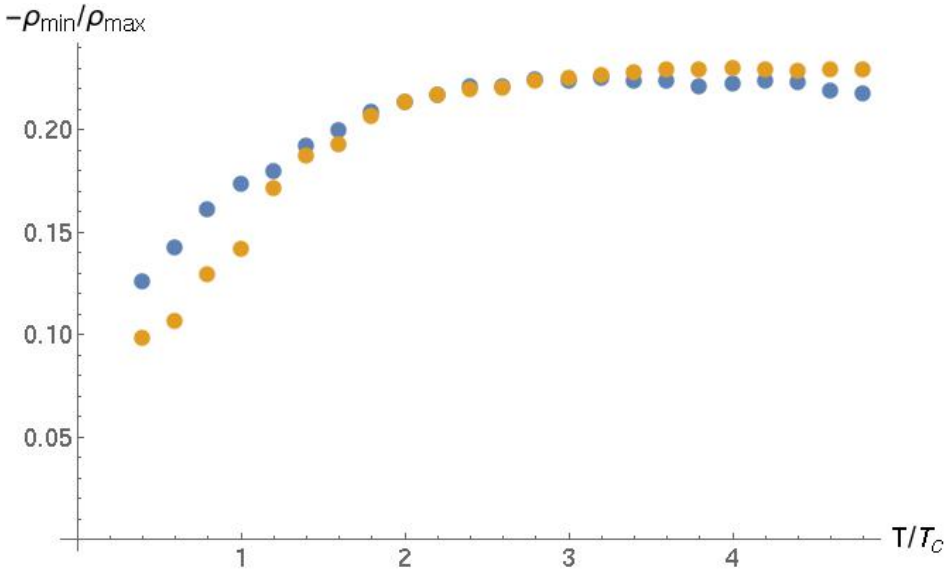

Figure 8.21: Thermal dependence of the violation of positivity of longitudinal gluons (blue) and transverse gluons (yellow) measured by the ratio of maximum to minimum of the spectral functions.

9 Shear viscosity to entropy density ratio

'Science is a field which grows continuously with ever expanding frontiers.'
John Bardeen

Science is a field which grows continuously with ever expanding frontiers. In this chapter, the results for the ratio $\frac{\eta}{s}$ are presented, calculated from the Landau gauge gluon spectral function obtained with extended-MEM using the diagrammatic representation derived in Chapter 6 for the spectral function of the EMT (3.33). First, the one loop approximation is considered, which yields already all qualitative features of $\frac{\eta}{s}$. The inclusion of the two loop diagrams turns out to be a correction, important for the quantitative precision. Of particular interest will be the extrapolation to the HTL perturbative regime and the discussion of a fitting function.

9.1 One loop $\frac{\eta}{s}$

In Fig.9.1, the extended-MEM one loop result for $\frac{\eta}{s}$ is shown. It was calculated from the extended-MEM gluon spectral functions presented and discussed in chapter 8 employing the one-loop representation of the shear viscosity (6.43) and lattice entropy from [192]. The entropy density is shown in Fig.9.2 in units of T^3. At high temperatures $\frac{s}{T^3}$ approaches the Stefan-Boltzmann limit

$$\frac{s_{SB}}{T^3} = \frac{32}{45}\pi^2 \approx 7.018 \tag{9.1}$$

At T_c the entropy density collapses, due to the change of degrees of freedom from quarks and gluons to hadrons[1]. The black data points in Fig.9.1 represent the extended-MEM

[1] In pure gauge theory, the degrees of freedom change from (quasi-)free gluons to glueballs.

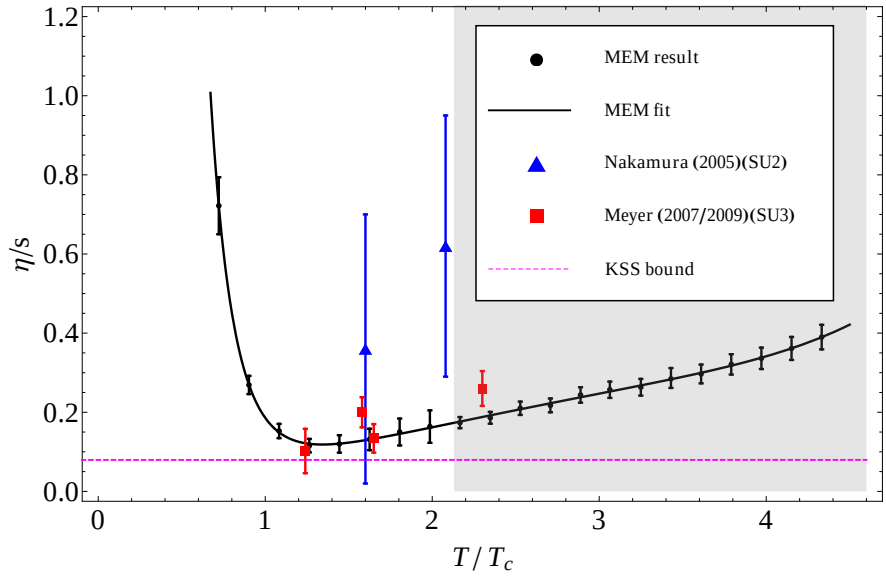

Figure 9.1: Thermal dependence of the viscosity over entropy density ratio $\frac{\eta}{s}$.

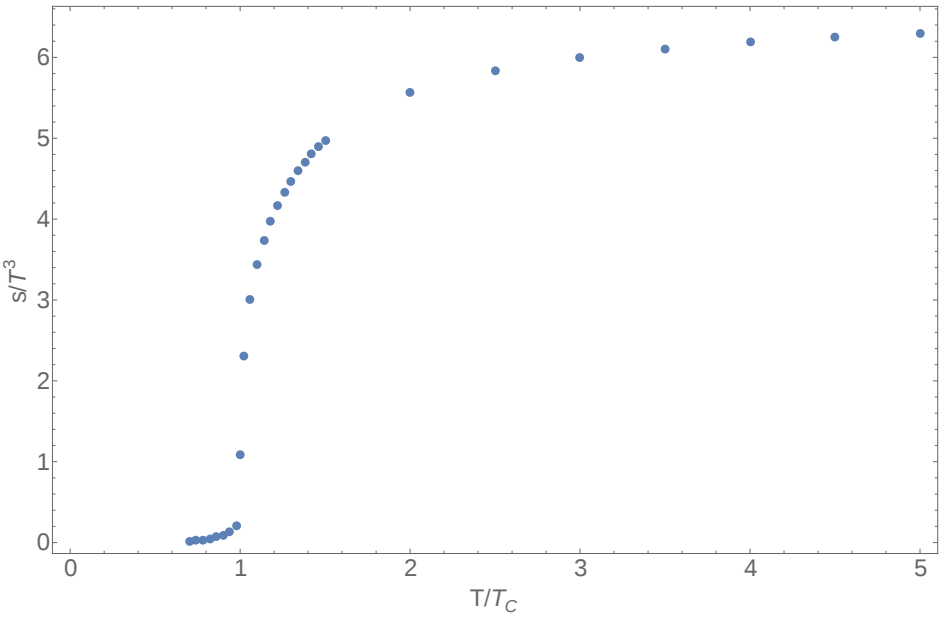

Figure 9.2: SU(3) entropy density in units of T^3 as a function of temperature in units of T_c.

results, while the black line interpolates the data points. The errors are systematic errors of the extended-MEM reconstruction. They are estimated, by varying the model function, the shift function and the precise form of the grid in frequency direction. In particular, for the model function and the shift function both overall normalisations and the onset of the asymptotic tail were varied. It turned out, that $\frac{\eta}{s}$ is insensitive to the precise form of the decay of the shift function towards zero frequency. The systematic extended-MEM error shows a slight temperature dependence, increasing towards

higher temperatures, but does not exceed 10% for $T = 4.5\,T_c$.

There is also a systematic error from the one-loop approximation. In [193] it has been discussed that higher loop corrections in an expansion in full propagators and full vertices can be minimized within an optimized RG–scheme for temperatures about T_c. Note, that even though this argument has been put forward in the context of the Polyakov loop potential, it has been applied to the effective action, that generates all correlation functions. Accordingly, the weighted difference of the full computation of the Polyakov loop potential and the one loop computation in full propagators can be used as an estimate for the systematic error of the one-loop aprroximation. However, this error estimate breaks down for high temperatures. For $T < 2.1\,T_c$ the systematic error estimation via the Polyakov loop potential is added to the extended-MEM systematic error. Above $T = 2.1\,T_c$, only extended-MEM errors are shown and the one-loop approximation of $\frac{\eta}{s}$ should be interpreted as a qualitative result. In particular in the high temperature region, higher loop corrections are expected to become relevant [131, 194]. The quantivative corrections are calculated in the next section.

For comparison, lattice results for $\frac{\eta}{s}$ are shown in Fig.9.1 as well [146, 195, 196]. The blue points are calculated for SU(2) and are expected to lie above the SU(3) results. (see (3.44)). The red points qualitatively agree with the extended-MEM results. Since the computational methods are different and independent, the agreement provides a non-trivial support for both computations.
The minimum value for the one-loop shear viscosity to entropy density ratio is found at $T_{min} = 1.25\,T_c$ with the value:

$$\left[\frac{\eta}{s}(T_{min})\right]_{\mathrm{SU(3)},1-loop} = 0.115(17) \tag{9.2}$$

This is close to, but well above the AdS/CFT bound.

9.2 Two loop $\frac{\eta}{s}$

The extension to two-loop order of the expansion of the EMT spectral function (3.33) takes into account the diagrams of Fig.6.2, that were already discussed in Section 6.4. All diagrams are proportinal to g^2. However, as discussed in the context of Table 6.1,

the origin of the coupling differs among the diagrams. Thus, the question of a consistent evaluation scale for the running coupling arises.
The finite temperature running coupling $\alpha_s(Q,T)$ is computed from the results for the dressing $z_{\bar{c}Ac}$ of the ghost-gluon vertex in [180]. It seems reasonable to employ the running coupling from this source, as it also supplied the SU(3) gluon propagators. Explicitly, the running coupling is given by

$$\alpha_s(Q,T) = \frac{z_{\bar{c}Ac}}{4\pi} \left(Q^2 G_c(Q,T)\right)^2 \left(Q^2 G_T(Q,T)\right) \tag{9.3}$$

in terms of the ghost and transverse gluon propagators G_c, G_T. In Fig.9.3 the running coupling is shown.
Before integration, each two-loop diagram depends on 5 loop variables: The two d^4p-integrations can be simplified in polar coordinates. All but one angular integrals can be carried out analytically. Only the angle Θ between the spatial momentum vectors remain. Thus, there are two frequency integrations, two spatial momentum integrations and one angular integrations[2]. A generic two-loop integral reads

$$D = \int d\omega_1 \int d\omega_2 \int dk_1 \int dk_2 \int d\Theta I(\omega_1, k_1, \omega_2, k_2, \Theta) \tag{9.4}$$

with the diagram specific integrand $I(\omega_1, k_1, \omega_2, k_2, \Theta)$. To find a sensible evaluation scale for the running coupling, for each 2-loop diagram type, the angular integration and one of the loop integrations is carried out, such that the reduced integrand

$$\hat{I}(\omega_1, k_1) = \int d\omega_2 \int dk_2 \int d\Theta I(\omega_1, k_1, \omega_2, k_2, \Theta) \tag{9.5}$$

only depends on a single set of loop integrations variables. The reduced integrand $\hat{I}(\omega_1, k_1)$ is found to be peaked for all diagrams around some diagram specific and temperature dependent $(\omega_{peak}, k_{peak})$. The running coupling, originated from internal Yang-Mills vertices is evaluated at $Q^2 = (2\pi\omega_{peak})^2 + k_{peak}^2$. In Fig. 9.4 $\hat{I}(\omega_1, k_1)$ is shown for the Eight at $T = 500$MeV. For this diagram, the peak values are $\omega_{peak} \approx T$ and $k_{peak} \approx 3\,T$. This procedure seems reasonable, as it picks out the relevant energy scale of each diagram. Note, that the main contribution comes from the momentum region, where the bending of the peak of the spectral function sets in. Thus, in particular the effect of the violation of positivity of the spectral function to inihbit the

[2]Note, that, the angular integration can also be carried out for the Eight and the 1-loop with a single vertex correction, due to the seperation of loops.

bending toward the main diagonal has a strong effect on shear viscosity. This is true for all two-loop diagrams.

On the other hand, the couplings that come from the non-Abelian part of the field

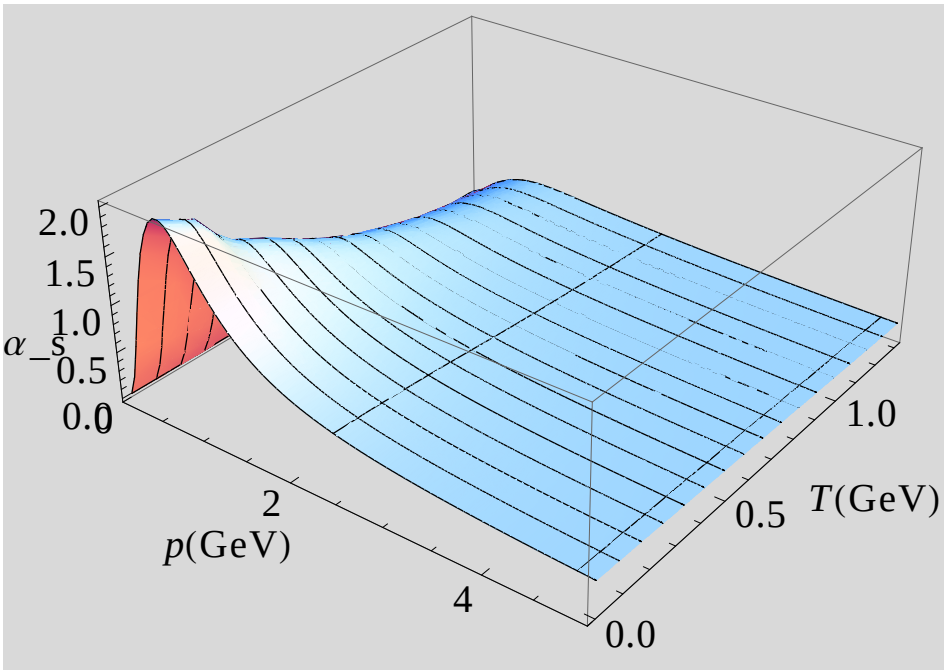

Figure 9.3: Finite temperature SU(3) running coupling $\alpha_s(Q,T)$.

strength tensor are treated differently. Naively, one could argue, that the classical energy-mometum tensor is used. Therefore, the couplings should not run at all. However, it turned out, that the vertex correction diagram would then show an insensible strong rise towards higher temperatures, which is supressed by the decay of α_s towards larger energy scales, if α_s is taken running. Also, a mere classical, undressed EMT is not RG scale invariant. Thus, the dressing of the EMT vertices, cannot be negected. However, an scale invariant EMT can be obtained by a running α_s. This, again raises the question of a reasonable scale, at which the running coupling is evaluated. In this thesis, the running coupling for the EMT vertices is evaluated at $Q = 2\pi T$. However, the precise scale only slightly changes the absolute size of the one-loop with a vertex correction, but does approximately not affect the high temperature behaviour.

This concludes the technical aspects of the two-loop diagrams. In Fig.9.5 the temperature dependence of two-loop contributions is shown. All points are normalized to the leading-order one-loop result. The points represent: Maki-Thompson(red), Eight(green), vertex correction(blue) and Sunset(grey). The Squint numerically turned out to contribute less then 1% of the the size of the Sunset diagram, and is not shown.

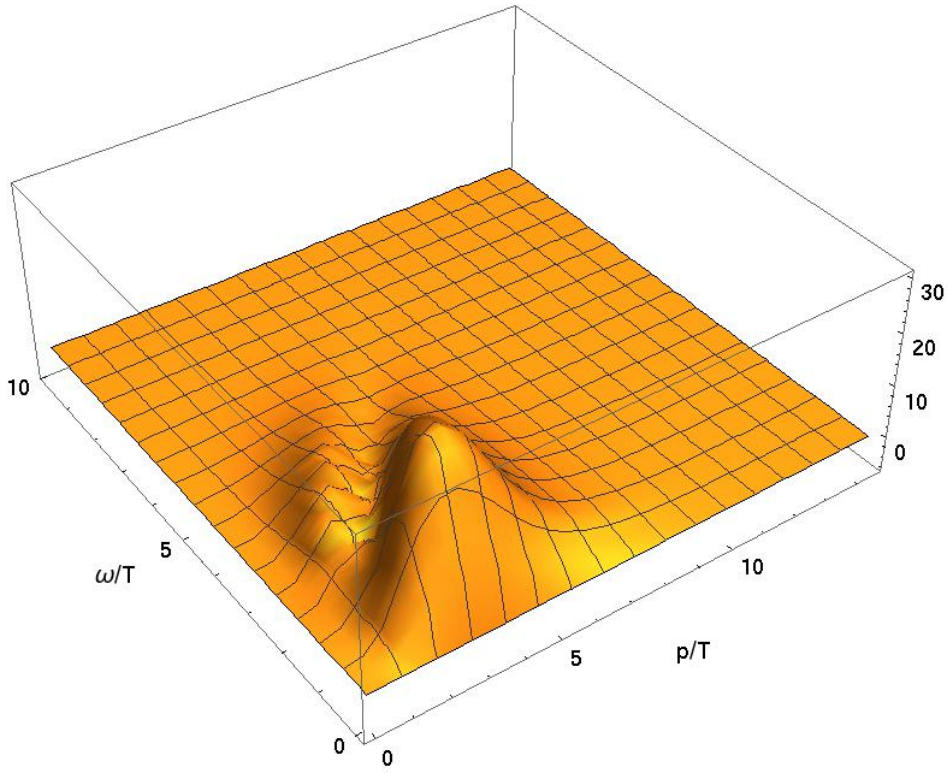

Figure 9.4: Reduced integrand $\hat{I}(\omega_1, k_1)$ for the Eight at $T = 500\text{MeV}$. The peak is located at $\omega_{peak} \approx T$ and $k_{peak} \approx 3\,T$.

The total size of all contributions is represented by the black points. It exhibits a minimum in the vicinity of T_c, which constitutes a direct confirmation of the argument of the minimization of higher loop contributions near T_c. In particular, the 10% correction is within the systematic error estimate of the one-loop approximation. Further, the size of the two-loop corrections increases towards higher temperatures. This indicates, that the corrections change the overall temperature dependence of $\frac{\eta}{s}$ in the high temperature regime. The Maki-Thompson diagram is subleading at high temperatures, followed by the Eight. Both diagrams show a steeper rise with temperature, than the one-loop contribution. This is in accordance with the discussion in [131]. Another confirmation of the validity of the diagrammatic approach is given by the vertex correction contribution. It has similar structure as the one-loop diagram and the extra loop at one of the EMT vertices cannot change the high temperature scaling. This is confirmed by the almost constant relative size vertex correction diagram towards higher temperatures.

In Fig.9.6 the absolute size of the full 2-loop extended-MEM result for $\frac{\eta}{s}$ is shown (red). For comparison, the one-loop result from Fig.9.1 is shown once more. Clearly, in the vicinity of T_c, the 2-loop corrections are within the systematic errors of the

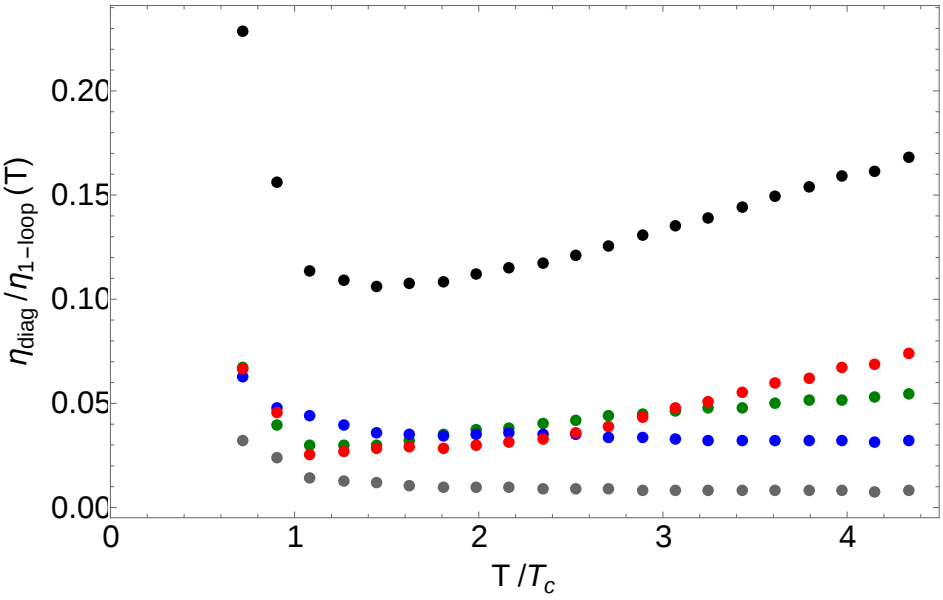

Figure 9.5: Thermal dependence of the two-loop contributions to $\frac{\eta}{s}$ normalized to the one-loop contribution. The diagrams are: Maki-Thompson(red), Eight(green), vertex correction(blue) and Sunset(grey). In addition the total size of all two loop contributions is shown(black).

one-loop approximation and the extended-MEM reconstruction. Towards higher T_c the relevance of the two-loop contributions grows. It is interesting that all two-loop contributions are positive corrections. This was not apriori clear, and is a numerical result. The Maki-Thompson diagram can be split into two classes: pure and mixed (as discussed in chapter 6. The mixed part is a negative correction, but the sum of pure and mixed is positive.

In the following two section the issues of the perturbative behaviour of $\frac{\eta}{s}$ and of a global fitting function are discussed. After that, an attempt is made, to map the SU(3) results on full QCD.

9.3 Extrapolation to the perturbative regime

A first step to find a global fit function, is the extrapolation of the extended-MEM results to high temperatures. There are available calculations of η in SU(3) and QCD in a leading-log approximation [197] and beyond leading-log [198]. For leading-log the high temperature form of η is

$$\eta = \kappa \frac{T^3}{g^4 \log(\frac{1}{g})} \tag{9.6}$$

where κ depends on the number of fermions.

The beyond leading-log shear viscosity is shown in [198] as a function of the Debye mass

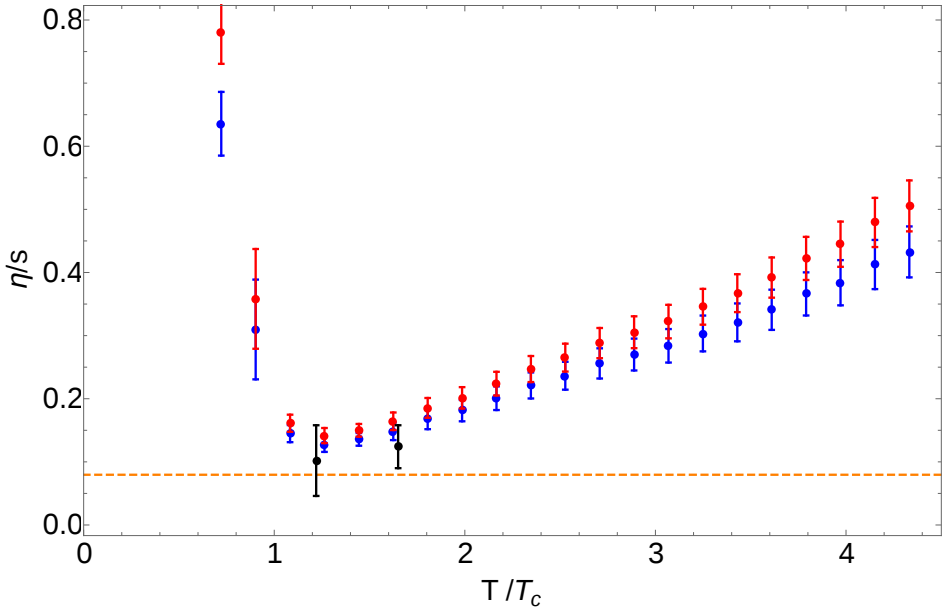

Figure 9.6: Thermal dependence of the two-loop result of $\frac{\eta}{s}$. For comparison, also the one-loop result is shown.

in units of temperature $m_D/T = g$. In order to obtain η as a function of temperature, the thermal dependence of the running coupling is needed. Note, that the available data for $\alpha_s(Q,T)$ from [180] is limited to $Q < 5\text{GeV}$ and $T < 5\,T_c$. Extrapolation of the data is possible, however, while the limit $Q \to \infty$ for fixed T is given by the zero temperature running coupling, the behaviour of α_s for $Q \approx T$ is not obvious. Thus, an extrapolation would induce large systematical errors and a different approach is chosen.

Inspecting the leading log shear viscosity (9.6) another issue is raised: What is the correct energy scale for the running coupling? Previous works use different conventions, see [199] and references therein. As in the high temperature limit, obviously temperature is the only available scale, it is reasonable to set $Q = cT$ with some constant c of order 1. Common choices are $c = 1$ and $c = 2\pi$, with regard to the factor of 2π in the Matsubara frequencies (4.20). In this thesis, c is taken as a variational fit parameter, to match the HTL viscosity to the extended-MEM data.
For the running coupling the zero-temperature perturbative α_s obtained from the two-loop β-function is employed (see Section 2.4):

$$\alpha_s(Q,T) \approx \alpha_s(Q = cT, 0) \tag{9.7}$$

In turns out, that the beyond leading log shear viscosity (divided by the lattice entropy density [192]) can be approximated by

$$\frac{\eta}{s}(T) \approx a\,\mathrm{Log}\left(\frac{cT}{\Lambda}\right)^{\gamma} \tag{9.8}$$

where $\Lambda = 0.7\mathrm{GeV}$ is the SU(3) scale and a, c, γ are variational parameters. In Fig.9.7 the data points are obtained from the beyond leading-log viscosity, with the scales $c = \pi, 2\pi, 4\pi$ for the running coupling (9.7). Clearly, the absolute value of $\frac{\eta}{s}$ is strongly dependent on the choice of the scale matching. The functional form, on the other hand is not. For all three choices of c, it was found that $\gamma = 1.457 - 1.462$ is approximately constant. In particular, γ determines the high temperature functional dependence. Thus it seems reasonable to fix this temperature dependence for the high temperature fitting function of the extended-MEM $\frac{\eta}{s}$ to the HTL value $\gamma_{HTL} = 1.46$.
For the high temperature regime the fitting function thus assumes the form:

$$\left(\frac{\eta}{s}\right)_{fit,pert}(T) = a\,\mathrm{Log}\left(\frac{cT}{\Lambda}\right)^{\gamma}_{HTL} \tag{9.9}$$

The temperature dependence of the shear viscosity to entropy density ratio below T_c can be approximated by the Hadron Resonance Gas model [200, 201]. Within this model of non-interacting hadrons and resonances, the low temperature behaviour of $\frac{\eta}{s}$ can be calculated analytically:

$$\left(\frac{\eta}{s}\right)_{fit,HRG}(T) \sim e^{-\frac{\Delta}{T}} \tag{9.10}$$

where Δ depends on the number of fermions, but will here be used as a variational parameter. The two limiting cases (9.9) and (9.10) with the parameters Δ, a, c are almost sufficient to fit the extended-MEM results for $\frac{\eta}{s}$ by

$$\left(\frac{\eta}{s}\right)_{fit}(T) = \left(\frac{\eta}{s}\right)_{fit,HRG}(T) + \left(\frac{\eta}{s}\right)_{fit,pert}(T) \tag{9.11}$$

However, the logarrithm is not real at sufficiently low temperatures. To avoid this, the perturbative part of the fitting function can be switched off by a Heavyside-step function $\Theta(T_{switch} - T)$ for $T < T_{switch}$. Similarly, the resonance gas part can be switched of above T_{switch}. To obtain a smooth curve, a mollified representation of the step function is used:

$$\Theta_m(x, k) = \frac{1}{1 + e^{-kx}} \tag{9.12}$$

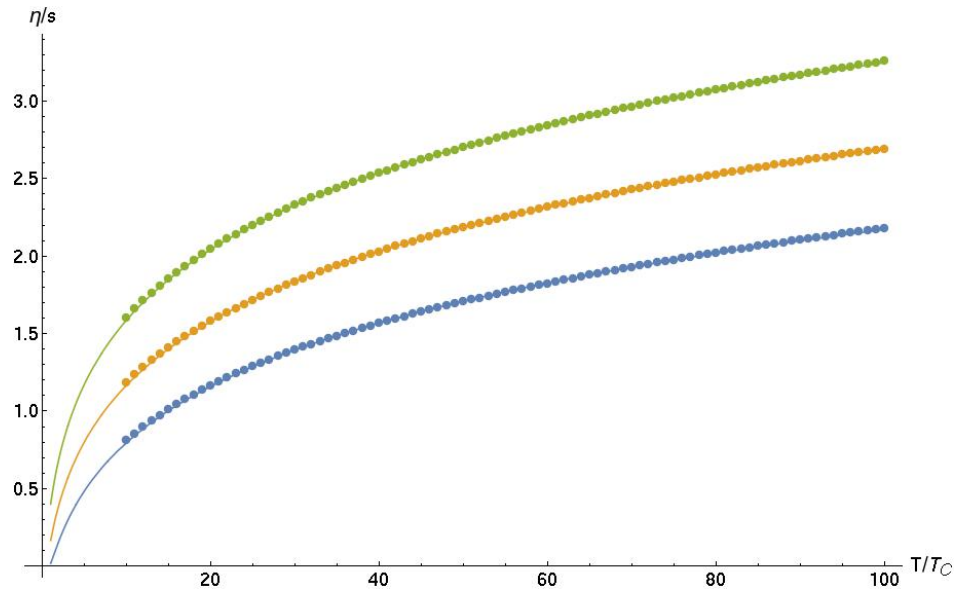

Figure 9.7: Perturbative $\frac{\eta}{s}$ as a function of temperature for $c = \pi$(blue), $c = 2\pi$(yellow), $c = 4\pi$(green). The points are obtained from the beyond leading-log viscosity in [198]. The fitting functions have the form (9.9).

which approaches $\Theta(x)$ in the limit $k \to 0$. The switch temperature T_{switch} is determined by Log $\left(\frac{cT}{\Lambda}\right) = 0$, whereas the mollification paramter k is an additional variational parameter. The final fitting function reads:

$$\left(\frac{\eta}{s}\right)_{fit}(T) = \Theta_m(T_{switch} - T, k)\left(\frac{\eta}{s}\right)_{fit,HRG}(T) + \Theta_m(T - T_{switch}, k)\left(\frac{\eta}{s}\right)_{fit,pert}(T) \tag{9.13}$$

In Fig. 9.8 the optimal fit is shown (blue), with $\Delta = 3.06$, $a = 0.313$, $c = 0.82\pi$, $k = 0.764$. The orange curve in addition shows the perturbative HTL prediction of Fig.9.7 for $c = 0.82\pi$. By construction, the fit function exhibits the correct HTL high temperature behavior. The minimum is slightly shifted to higher temperatures. The fitting function assumes the minimum at $1.35\,T_c$ (compared to $1.25\,T_c$ from extended-MEM). This is well within the systematic extended-MEM error. Fixing the minimum at the extended-MEM position would require additional fit parameters. However, in the spirit of minimizing the number of fit parameters, equation(9.13) seems to fit the data reasonably well. Note, that the comparison to HTL effectively represents a comparison of η, as the entropy density is taken from the same source for extended-MEM and HTL results. The choice of comparing $\frac{\eta}{s}$ is merely due to the importance of this dimensionless quantity.

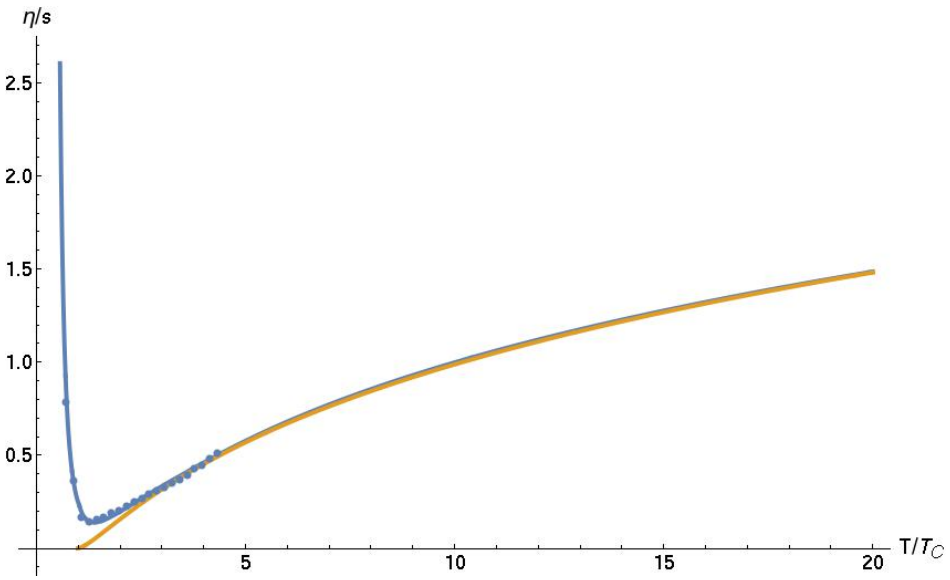

Figure 9.8: Fit of the extendend-MEM results (blue points) for $\frac{\eta}{s}$(blue curve). The values for the fit paramters are: $\Delta = 3.06$, $a = 0.313$, $c = 0.82\pi$, $k = 0.764$. The orange curve shows the perturbative HTL-$\frac{\eta}{s}$ with $c = 0.82\pi$.

9.4 Translation to QCD

In this concluding section a mapping of the pure gauge $\frac{\eta}{s}$ to full QCD is proposed. The idea extends the general argument put forward in [196]. In this reference, shear viscosity was computed on the lattice at $T = 2.3\,T_c$ for pure SU(3) gauge theory. Then a 'fugde' was proposed, by scaling the result by the ratio of the pertubative shear viscosity to entropy density ratio of SU(3) and QCD. It was argued, that it at least gives a qualitative mapping. Here, a slightly different mapping is proposed. In the high temperature regime, the entropy density is approximately constant. Thus, $\frac{\eta}{s}$ for SU(3) can be approximately written as a function of the running coupling with the beyond leading-log result from [198] for $n_f = 0$. In particular, for the 1-loop running coupling (2.28), the perturbative part (9.9) of the fit (9.13) is:

$$\left(\frac{\eta}{s}\right)^{\mathrm{SU(3)}}_{fit,pert}(T) = a\,\mathrm{Log}\left(\frac{cT}{\Lambda_{\mathrm{SU(3)}}}\right)^{\gamma_{HTL}} = a\left(\frac{1}{2\beta_0}\right)^{\gamma_{HTL}}\left(\frac{1}{\alpha_s}\right)^{\gamma_{HTL}} \tag{9.14}$$

Now, the 1-loop QCD running coupling is inserted. Both the one-loop coefficient $\beta_0^{\mathrm{SU(3)}} \to \beta_0^{\mathrm{QCD}}$ and the scale $\Lambda_{\mathrm{SU(3)}} \to \Lambda_{\mathrm{QCD}}$ change. Thus, the perturbative part of the mapping is:

$$\left(\frac{\eta}{s}\right)^{QCD}_{fit,pert}(T) = a\,\mathrm{Log}\left(\frac{cT}{\Lambda_{\mathrm{QCD}}}\right)^{\gamma_{HTL}} = \left(\frac{\beta_0^{\mathrm{SU(3)}}}{\beta_0^{\mathrm{QCD}}}\right)^{\gamma_{HTL}} a\,\mathrm{Log}\left(\frac{c\,T}{\Lambda_{\mathrm{SU(3)}}}\right)^{\gamma_{HTL}} \tag{9.15}$$

For the low temperature part of the fit, the calculation of $\frac{\eta}{s}$ in the HRG model is taken from [202]. Thus, this part is not explicitly fitted to the extended-MEM results. As for SU(3), a smooth matching of the perturbative and the HRG contribution is mediated by a mollified step function. The form of the QCD-fit equals (9.13). In Fig.9.9 the resulting mapping is shown. The QCD-$\frac{\eta}{s}$ is shown in blue, while the pure gauge result from Fig.9.8 is shown in yellow. At $2.3\,T_c$ the ratio between $\frac{\eta}{s}$ of SU(3) and QCD is

$$r = \left[\frac{\eta}{s}\right]_{\mathrm{QCD}} / \left[\frac{\eta}{s}\right]_{\mathrm{SU(3)}} = 1.14 \tag{9.16}$$

This strongly deviates from the result of $r = 1.53$ in [196]. The reason for the deviation can be the effect of the entropy, that has not been considered here. It seems resonable, to take $r = 1.53$ as a reference and rescale the the QCD-$\frac{\eta}{s}$, accordingly. The rescaled QCD-viscosity is shown in Fig.9.10. Thus, the best guess for the minimum value of $\frac{\eta}{s}$ in QCD is:

$$\left[\frac{\eta}{s}\right]^{QCD}_{min} = 0.21 \tag{9.17}$$

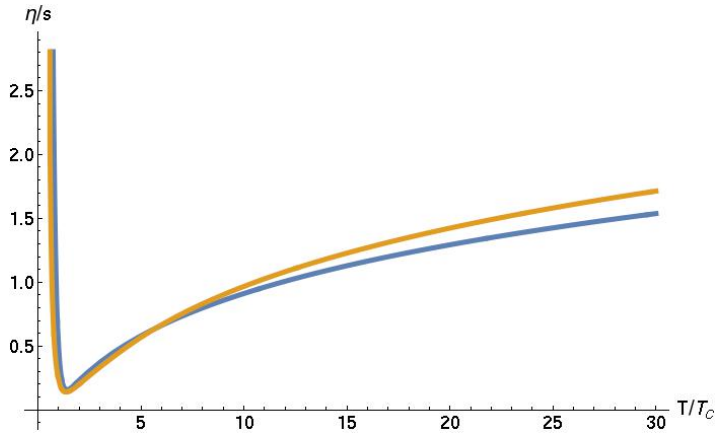

Figure 9.9: Mapping of $\frac{\eta}{s}$ of SU(3) to QCD, by considering $\frac{\eta}{s}$ approximately as a function of α_s, and the exchange $\alpha_s^{\mathrm{SU(3)}} \to \alpha_s^{\mathrm{QCD}}$.

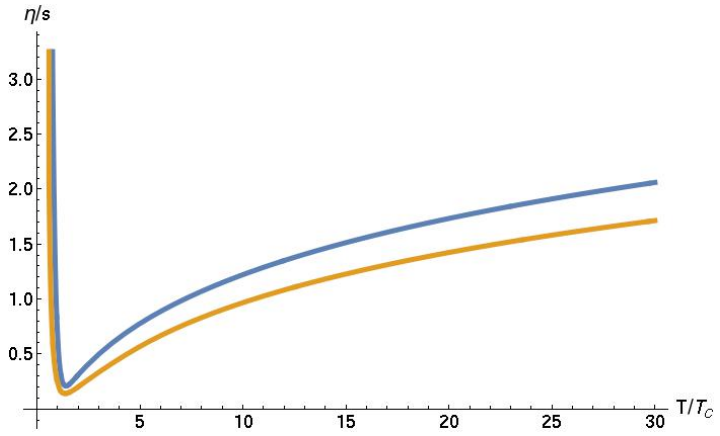

Figure 9.10: Mapping of $\frac{\eta}{s}$ of SU(3) to QCD, by considering $\frac{\eta}{s}$ approximately as a function of α_s, and the exchange $\alpha_s^{\mathrm{SU(3)}} \to \alpha_s^{\mathrm{QCD}}$. Further, the mapping is matched at $T = 2.4\,T_c$ to the result $\left[\frac{\eta}{s}\right]_{\mathrm{QCD}} / \left[\frac{\eta}{s}\right]_{\mathrm{SU(3)}} = 1.53$ from [196].

10 Summary and Outlook

In this thesis gluon spectral functions were calculated from finite temperature gluon propagators in pure SU(3) gauge theory. While many previous calculations of gluon spectral functions assumed a quasi-particle description with a positive definite spectral function, it could be shown here, that the violation of positivity in the spectral function plays a crucial role for gluons, even above the confinement/deconfinement temperature. The violation of positivity is a direct consequence of confinement, and is visible on the level of the propagators. While propagators of free particles are convex, gluon propagators exhibit a concave region at low momenta. It was motivated, that a concav propagator requires negative contributions in the spectral function.

Compared to spectral functions in the Dymnamical quasi-particle model, where the peak of the spectral function approaches the main diagonal in the frequency-momentum plane at low momenta, the bending of the spectral functions calculated in this thesis towards the main diagonal was inhibited by the region of negativity. This deviation from the quasi-particle behavior strongly influenced derived quantities as the shear viscosity to entropy density ratio $\frac{\eta}{s}$. It was shown that the leading order contribution was peaked in the frequency-momentum plane, where the bending did not set yet in. Above the critical temperature, the violation of positivity decreased, signaling, that the quasi-paricle picture becomes more accurate in the high temperature phase, as expected. However, a narrowing of the peak of the spectral function at high temperatures, as predicted by HTL perturbation theory could not be observed. Whether the narrowing sets in at higher temperatures than the highest temperature available in this thesis, or whether an unknown systematic effect on the spectral functions is present, cannot be decided conclusively. It was argued, that the loss of information in the Matsubara imaginary time function can be a reason for larger systematical errors of extended-MEM at high temperatures.

The numerical tool to compute the spectral functions has been an extended Maxium

Entropy Method. While standard MEM assumes a positive definite spectral function, the violation of positivity of the gluonic spectral functions required a revision of MEM. It turned out, that shifting the propagator with respect to a shift spectral function was able to lift the violation of positivity, without overly suppressing the data. The introduction of the shift function promoted MEM to extended-MEM, an algorithm capable of reconstructing general spectra, as long as the violation of positivity is finite.
Further applications of extended-MEM could reconstruct quark spectral functions at finite temperature in full QCD or other effective theories involving fermions. Here, however, the particle spectrum is expected to show multiple poles on top of a continuous background. This certainly will be a cumbersome goal for extended-MEM.

The main application of this thesis, the determination of $\frac{\eta}{s}$ for arbitrary (finite) temperatures yielded a first-principle calculation for this intriguing quantity. A loop representation of η in terms of gluon and ghost spectral functions was derived. Interestingly, the total number of diagrams is finite, even though the explicit evaluation of higher loop contributions turned out impractical. It was argued, that in the vicinity of the critical temperature, the higher loop contributions are supressed, while they become important in the perturbative regime. This was checked, by calculating both the leading order (one-loop) contribution and the two-loop diagrams. Indeed, the corrections due to the next-to-leading order contributions were within the systematic error of the one-loop approximation in the vicinity of T_c. For higher temperatures, the two-loop contributions grew relative to leading order, such, that they were relevant for the extrapolation to the HTL-limit. In particular, it turned out, that the Maki-Thompson diagram is subleading - in accordance with predictions.
Even higher loop contributions are not expected to change the picture qualitatively. Nevertheless, the evaluation of at least the diagrams that are expected to be leading among the three-loop contributions would be desireable. In particular, the question of renormalization could be studied. To two-loop order all diagrams are finite. The question, whether this is rather a coincidence or whether η is finite within this expansion in the first place is interesting to pursue further.

The minimum of $\frac{\eta}{s}$ is assumed for $T = 1.25\,T_c$ and lies close to, but well above the AdS/CFT bound. Further, the extended-MEM study for $\frac{\eta}{s}$ agrees with results from the lattice. This agreement constitutes a non-trivial support for both results. A fit function was provided, to both interpolate an extrapolate the extended-MEM results.

Apart from a smooth approximation for the Heavyside-step function merely three parameters were needed. Below the critical temperature, the physical degrees of freedom of QCD are hadrons, and the temperature dependence of $\frac{\eta}{s}$ can be described by a single scale parameter within the Hadron Resonance Gas (HRG) model. For pure gauge theory, there are obviously no hadrons. However, the HRG-model can still be employed with glueballs as relevant degrees of freedom. Note, that the loop representation of the spectral function of the energy-momentum tensor in terms of gluon spectral functions is also valid below T_c.
In the opposite limit of high temperatures, two parameters were needed to fit the extended-MEM results to the HTL prediction, where gluons are expected to be dominant even in a theory including fermions.

A mapping of the SU(3) results to QCD was proposed, employing next-to-leading order pertubative calculations for shear viscosity and a QCD entropy density. It will be interesting to see what predictions can be extracted from the QCD fit for the interpretation of the physics involved in heavy-ion collisions. Simulations of heavy-ion collisions create initial state density configuration for particle sheets, which are subsequently brought to collision. For the after collision dynamics in the QGP phase (after local thermal equilibrium is reached) $\frac{\eta}{s}(T)$ is a critical input. In this thesis the sensitive dependence of the final state spatial anisotropy on $\frac{\eta}{s}$ was already discussed. Thus, the fit function can help to improve HIC-simulations.

It would also be interesting to extend the framework of this thesis to full QCD. As mentioned above, the reconstruction of quark spectral functions will most probable be the strongest obstacle to overcome. Apart from that, there is, however, no fundamental or methodological issue, preventing the framework to be readily extended to full QCD.

Also, in pure SU(3) gauge theory further investigations of $\frac{\eta}{s}$ are of interest. The energy-mometum tensor was assumed with its classical tensor structure. In particular, no explicit ghost field dependence was present. Thus, ghost fields could only enter in higher loop contributions via the field derivatives in the magic formula. Further, the Yang-Mills vertices were supplied with the classical tensor structure, whereas for the coupling, a temperature and diagram dependent evaluation scale was chosen. The choices led to a consistent picture for $\frac{\eta}{s}$, leave, however, also space for further refinement.

Lately, new Bayesian reconstruction methods were proposed, using an extended search space for the spectral function [82, 203–205]. It was argued, that there are cases, where MEM cannot find the correct spectral function. For gluon spectral functions, there are no indications, that the extended-MEM employed in this thesis ran into a pathological case. Even though, it would be interesting to have an independent reconstruction technique available. Whether the new Bayesian method can reconstuct positivity violating spectral functions remains to be seen.

11 Acknowledgements

Bibliography

[1] K. Huang, *Fundamental forces of nature: the story of gauge fields*, World Scientific, 2007.

[2] W. Greiner, S. Schramm, and E. Stein, *Quantum Chromodynamics*, Physics and astronomy online library, Springer, 2002.

[3] H. Fritzsch and P. Minkowski, *Colored gluons, bjorken scaling and quark confinement*, Physics Letters B **49**, 462 (1974).

[4] K. G. Wilson, *Confinement of quarks*, Phys. Rev. D **10**, 2445 (1974).

[5] C. N. Yang and R. L. Mills, *Conservation of Isotopic Spin and Isotopic Gauge Invariance*, Phys. Rev. **96**, 191 (1954).

[6] S. Coleman and D. J. Gross, *Price of Asymptotic Freedom*, Phys. Rev. Lett. **31**, 851 (1973).

[7] D. J. Gross and F. Wilczek, *Ultraviolet Behavior of Non-Abelian Gauge Theories*, Phys. Rev. Lett. **30**, 1343 (1973).

[8] H. D. Politzer, *Reliable Perturbative Results for Strong Interactions?*, Phys. Rev. Lett. **30**, 1346 (1973).

[9] J. C. Collins and M. Perry, *Superdense Matter: Neutrons Or Asymptotically Free Quarks?*, Phys.Rev.Lett. **34**, 1353 (1975).

[10] N. Cabibbo and G. Parisi, *Exponential Hadronic Spectrum and Quark Liberation*, Phys.Lett. **B59**, 67 (1975).

[11] E. V. Shuryak, *Quark-Gluon Plasma and Hadronic Production of Leptons, Photons and Psions*, Phys.Lett. **B78**, 150 (1978).

[12] B. Freedman and L. D. McLerran, *Quark Star Phenomenology*, Phys.Rev. **D17**, 1109 (1978).

[13] G. Baym and S. Chin, *Can a Neutron Star Be a Giant MIT Bag?*, Phys.Lett. **B62**, 241 (1976).

[14] B. A. Freedman and L. D. McLerran, *Speculations on a Phase Transition Between Nuclear and Quark Matter at High Densities*, Phys. Rev. Lett. (1976).

[15] D. H. Rischke, *The Quark gluon plasma in equilibrium*, Prog.Part.Nucl.Phys. **52**, 197 (2004).

[16] K. Adcox *et al.*, *Formation of dense partonic matter in relativistic nucleus-nucleus collisions at RHIC: Experimental evaluation by the PHENIX collaboration*, Nucl.Phys. **A757**, 184 (2005).

[17] A. Andronic and P. Braun-Munzinger, *Ultrarelativistic nucleus-nucleus collisions and the quark gluon plasma*, Lect.Notes Phys. **652**, 35 (2004).

[18] J. Adams *et al.*, *Experimental and theoretical challenges in the search for the quark gluon plasma: The STAR Collaboration's critical assessment of the evidence from RHIC collisions*, Nucl.Phys. **A757**, 102 (2005).

[19] H. B. Meyer, *Transport Properties of the Quark-Gluon Plasma: A Lattice QCD Perspective*, Eur.Phys.J. **A47**, 86 (2011).

[20] A. Mocsy, P. Petreczky, and M. Strickland, *Quarkonia in the Quark Gluon Plasma*, Int.J.Mod.Phys. **A28**, 1340012 (2013).

[21] P. Steinberg, *What have we learned about the Quark-Gluon Plasma with the ATLAS detector at the LHC?*, Nucl.Phys. **A** (2014).

[22] M. Tannenbaum, *Latest Results from BNL and RHIC–2013*, (2014).

[23] I. Tserruya, *The Strongly Interacting Quark Gluon Plasma at RHIC and LHC*, EPJ Web Conf. **70**, 00022 (2014).

[24] K. Rajagopal and F. Wilczek, *The Condensed matter physics of QCD*, (2000).

[25] A. Bazavov, T. Bhattacharya, M. Cheng, C. DeTar, H. Ding, *et al.*, *The chiral and deconfinement aspects of the QCD transition*, Phys.Rev. **D85**, 054503 (2012).

[26] S. Weinberg, *The Problem of Mass*, Trans.New York Acad.Sci. **38**, 185 (1977).

[27] F. Karsch and M. Lutgemeier, *Deconfinement and chiral symmetry restoration in an SU(3) gauge theory with adjoint fermions*, Nucl.Phys. **B550**, 449 (1999).

[28] K. Fukushima, *Relation between the Polyakov loop and the chiral order parameter at strong coupling*, Phys.Rev. **D68**, 045004 (2003).

[29] C. S. Fischer, J. Luecker, and J. A. Mueller, *Chiral and deconfinement phase transitions of two-flavour QCD at finite temperature and chemical potential*, Phys.Lett. **B702**, 438 (2011).

[30] J. Braun and T. K. Herbst, *On the Relation of the Deconfinement and the Chiral Phase Transition in Gauge Theories with Fundamental and Adjoint Matter*, (2012).

[31] G. Burgio, M. Baldo, P. Sahu, and H. Schulze, *The Hadron quark phase transition in dense matter and neutron stars*, Phys.Rev. **C66**, 025802 (2002).

[32] D. Boyanovsky, *Phase transitions in the early and the present universe: From the big bang to heavy ion collisions*, page 3 (2001).

[33] U. W. Heinz and P. F. Kolb, *Early thermalization at RHIC*, Nucl.Phys. **A702**, 269 (2002).

[34] P. F. Kolb and U. W. Heinz, *Hydrodynamic description of ultrarelativistic heavy ion collisions*, (2003).

[35] P. Kolb, P. Huovinen, U. W. Heinz, and H. Heiselberg, *Elliptic flow at SPS and RHIC: From kinetic transport to hydrodynamics*, Phys.Lett. **B500**, 232 (2001).

[36] K. Dusling and D. Teaney, *Simulating elliptic flow with viscous hydrodynamics*, Phys.Rev. **C77**, 034905 (2008).

[37] H. Song and U. W. Heinz, *Suppression of elliptic flow in a minimally viscous quark-gluon plasma*, Phys.Lett. **B658**, 279 (2008).

[38] D. Molnar and P. Huovinen, *Dissipative effects from transport and viscous hydrodynamics*, J.Phys. **G35**, 104125 (2008).

[39] H. Niemi, G. S. Denicol, P. Huovinen, E. Molnar, and D. H. Rischke, *Influence of the shear viscosity of the quark-gluon plasma on elliptic flow in ultrarelativistic heavy-ion collisions*, Phys.Rev.Lett. **106**, 212302 (2011).

[40] G. Denicol, T. Kodama, and T. Koide, *The effect of shear and bulk viscosities on elliptic flow*, J.Phys. **G37**, 094040 (2010).

[41] E. V. Shuryak, *Theory of Hadronic Plasma*, Sov.Phys.JETP **47**, 212 (1978).

[42] P. Danielewicz and M. Gyulassy, *Dissipative Phenomena in Quark Gluon Plasmas*, Phys.Rev. **D31**, 53 (1985).

[43] B. Back, M. Baker, M. Ballintijn, D. Barton, B. Becker, *et al.*, *The PHOBOS perspective on discoveries at RHIC*, Nucl.Phys. **A757**, 28 (2005).

[44] I. Arsene *et al.*, *Quark gluon plasma and color glass condensate at RHIC? The Perspective from the BRAHMS experiment*, Nucl.Phys. **A757**, 1 (2005).

[45] P. Huovinen, P. Kolb, U. W. Heinz, P. Ruuskanen, and S. Voloshin, *Radial and elliptic flow at RHIC: Further predictions*, Phys.Lett. **B503**, 58 (2001).

[46] D. Teaney, J. Lauret, and E. V. Shuryak, *Flow at the SPS and RHIC as a quark gluon plasma signature*, Phys.Rev.Lett. **86**, 4783 (2001).

[47] D. Teaney, J. Lauret, and E. Shuryak, *A Hydrodynamic description of heavy ion collisions at the SPS and RHIC*, (2001).

[48] T. Hirano and K. Tsuda, *Collective flow and two pion correlations from a relativistic hydrodynamic model with early chemical freezeout*, Phys.Rev. **C66**, 054905 (2002).

[49] M. Gyulassy and L. McLerran, *New forms of QCD matter discovered at RHIC*, Nucl.Phys. **A750**, 30 (2005).

[50] D. Teaney, *The Effects of viscosity on spectra, elliptic flow, and HBT radii*, Phys.Rev. **C68**, 034913 (2003).

[51] E. V. Shuryak, *What RHIC experiments and theory tell us about properties of quark-gluon plasma?*, Nucl.Phys. **A750**, 64 (2005).

[52] A. Muronga and D. H. Rischke, *Evolution of hot, dissipative quark matter in relativistic nuclear collisions*, (2004).

[53] U. W. Heinz, H. Song, and A. K. Chaudhuri, *Dissipative hydrodynamics for viscous relativistic fluids*, Phys.Rev. **C73**, 034904 (2006).

[54] U. W. Heinz, *'RHIC serves the perfect fluid': Hydrodynamic flow of the QGP*, page 3 (2005).

[55] R. Baier, P. Romatschke, and U. A. Wiedemann, *Dissipative hydrodynamics and heavy ion collisions*, Phys.Rev. **C73**, 064903 (2006).

[56] A. Chaudhuri, *Saturation of elliptic flow and shear viscosity*, (2007).

[57] P. Kovtun, D. T. Son, and A. O. Starinets, *Viscosity in strongly interacting quantum field theories from black hole physics*, Phys.Rev.Lett. **94**, 111601 (2005).

[58] S. Gavin and M. Abdel-Aziz, *Measuring Shear Viscosity Using Transverse Momentum Correlations in Relativistic Nuclear Collisions*, Phys.Rev.Lett. **97**, 162302 (2006).

[59] P. Romatschke and U. Romatschke, *Viscosity Information from Relativistic Nuclear Collisions: How Perfect is the Fluid Observed at RHIC?*, Phys.Rev.Lett. **99**, 172301 (2007).

[60] A. Chaudhuri, *Viscous fluid dynamics in Au+Au collisions at RHIC*, (2008).

[61] R. Averbeck, *The viscosity to entropy density ratio from PHENIX data on single electron production*, J.Phys. **G35**, 104115 (2008).

[62] P. Steinberg, *First results from the LHC heavy ion program*, New J.Phys. **14**, 035006 (2012).

[63] R. Gupta, *Introduction to lattice QCD: Course*, page 83 (1997).

[64] P. de Forcrand, *Simulating QCD at finite density*, PoS **LAT2009**, 010 (2009).

[65] Y. Nambu and G. Jona-Lasinio, *Dynamical Model of Elementary Particles Based on an Analogy with Superconductivity. 1.*, Phys.Rev. **122**, 345 (1961).

[66] Y. Nambu and G. Jona-Lasinio, *Dynamical Model of Elementary Particles Based on an Analogy with Superconductivity. 2.*, Phys.Rev. **124**, 246 (1961).

[67] M. Zubkov, *Schwinger - Dyson equation and NJL approximation in massive gauge theory with fermions*, (2014).

[68] A. Grunfeld, D. Menezes, M. Pinto, and N. Scoccola, *Phase structure of cold magnetized quark matter within the SU(3) NJL model*, Phys.Rev. **D90**, 044024 (2014).

[69] R.-A. Tripolt, L. von Smekal, and J. Wambach, *Flow equations for spectral functions at finite external momenta*, (2014).

[70] A. Meistrenko, C. Wesp, H. van Hees, and C. Greiner, *Nonequilibrium dynamics and transport near the chiral phase transition of a quark-meson model*, J.Phys.Conf.Ser. **503**, 012003 (2014).

[71] R.-A. Tripolt, N. Strodthoff, L. von Smekal, and J. Wambach, *Spectral Functions for the Quark-Meson Model Phase Diagram from the Functional Renormalization Group*, Phys.Rev. **D89**, 034010 (2014).

[72] C. S. Fischer, *Infrared properties of QCD from Dyson-Schwinger equations*, J.Phys. **G32**, R253 (2006).

[73] C. Wetterich, *Exact evolution equation for the effective potential*, Phys.Lett. **B301**, 90 (1993).

[74] J. M. Pawlowski, *Aspects of the functional renormalisation group*, Annals Phys. **322**, 2831 (2007).

[75] R. Kubo, *Statistical mechanical theory of irreversible processes. 1. General theory and simple applications in magnetic and conduction problems*, J.Phys.Soc.Jap. **12**, 570 (1957).

[76] A. N. Tikhonov, *Solution of Incorrectly Formulated Problems and the Regularization Method*, Sov. Math. Dokl. **4**, 1035 (1963).

[77] J. Brolley, *Signal Processing by p Log p Maximum Entropy Analysis*, (1977).

[78] J. Brolley, R. Lazarus, B. Suydam, and H. Trussell, *Two-Dimensional Maximum Entropy Image Restoration*, (1977).

[79] M. Asakawa, T. Hatsuda, and Y. Nakahara, *Maximum entropy analysis of the spectral functions in lattice QCD*, Prog.Part.Nucl.Phys. **46**, 459 (2001).

[80] P. Petreczky, F. Karsch, E. Laermann, S. Stickan, and I. Wetzorke, *Temporal quark and gluon propagators: Measuring the quasiparticle masses*, Nucl.Phys.Proc.Suppl. **106**, 513 (2002).

[81] G. Aarts, C. Allton, M. B. Oktay, M. Peardon, and J.-I. Skullerud, *Charmonium at high temperature in two-flavor QCD*, Phys.Rev. **D76**, 094513 (2007).

[82] Y. Burnier and A. Rothkopf, *Bayesian Approach to Spectral Function Recon-*

struction for Euclidean Quantum Field Theories, Phys.Rev.Lett. **111**, 182003 (2013).

[83] M. Fukugita, M. Okawa, and A. Ukawa, *Finite-size scaling study of the deconfining phase transition in pure SU(3) lattice gauge theory*, Nuclear Physics B **337**, 181 (1990).

[84] L. G. Yaffe and B. Svetitsky, *First-order phase transition in the SU(3) gauge theory at finite temperature*, Phys. Rev. D **26**, 963 (1982).

[85] B. Lucini, M. Teper, and U. Wenger, *Properties of the deconfining phase transition in SU(N) gauge theories*, JHEP **0502**, 033 (2005).

[86] K. Holland and U.-J. Wiese, *The Center symmetry and its spontaneous breakdown at high temperatures*, (2000).

[87] G. Martinez, *Advances in Quark Gluon Plasma*, (2013).

[88] C. Bernard, T. Burch, C. E. DeTar, S. Gottlieb, U. Heller, *et al.*, *The equation of state for QCD with 2+1 flavors of quarks*, PoS **LAT2005**, 156 (2006).

[89] Y. Aoki, S. Borsanyi, S. Durr, Z. Fodor, S. D. Katz, *et al.*, *The QCD transition temperature: results with physical masses in the continuum limit II.*, JHEP **0906**, 088 (2009).

[90] C. S. Fischer and J. Luecker, *Propagators and phase structure of Nf=2 and Nf=2+1 QCD*, Phys.Lett. **B718**, 1036 (2013).

[91] A. Bazavov, T. Bhattacharya, C. DeTar, H. T. Ding, S. Gottlieb, *et al.*, *The equation of state in (2+1)-flavor QCD*, (2014).

[92] B.-J. Schaefer, J. M. Pawlowski, and J. Wambach, *The Phase Structure of the Polyakov–Quark-Meson Model*, Phys.Rev. **D76**, 074023 (2007).

[93] T. K. Herbst, J. M. Pawlowski, and B.-J. Schaefer, *The phase structure of the Polyakov–quark-meson model beyond mean field*, Phys.Lett. **B696**, 58 (2011).

[94] M. Asakawa and K. Yazaki, *Chiral Restoration at Finite Density and Temperature*, Nucl.Phys. **A504**, 668 (1989).

[95] K. Fukushima, *Phase diagrams in the three-flavor Nambu-Jona-Lasinio model with the Polyakov loop*, Phys.Rev. **D77**, 114028 (2008).

[96] R. V. Gavai and S. Gupta, *On the critical end point of QCD*, Phys. Rev. D **71**, 114014 (2005).

[97] B.-J. Schaefer and M. Wagner, *The Three-flavor chiral phase structure in hot and dense QCD matter*, Phys.Rev. **D79**, 014018 (2009).

[98] T. K. Herbst, J. M. Pawlowski, and B.-J. Schaefer, *The Impact of Fluctuations on QCD Matter*, Acta Phys.Polon.Supp. **5**, 733 (2012).

[99] H. Abuki, R. Anglani, R. Gatto, G. Nardulli, and M. Ruggieri, *Chiral crossover, deconfinement and quarkyonic matter within a Nambu-Jona Lasinio model with the Polyakov loop*, Phys.Rev. **D78**, 034034 (2008).

[100] L. McLerran, K. Redlich, and C. Sasaki, *Quarkyonic Matter and Chiral Symmetry Breaking*, Nucl.Phys. **A824**, 86 (2009).

[101] K. Fukushima and C. Sasaki, *The phase diagram of nuclear and quark matter at high baryon density*, Prog.Part.Nucl.Phys. **72**, 99 (2013).

[102] G. 't Hooft, *A Two-Dimensional Model for Mesons*, Nucl.Phys. **B75**, 461 (1974).

[103] G. 't Hooft, *A Planar Diagram Theory for Strong Interactions*, Nucl.Phys. **B72**, 461 (1974).

[104] O. Aharony, S. S. Gubser, J. M. Maldacena, H. Ooguri, and Y. Oz, *Large N field theories, string theory and gravity*, Phys.Rept. **323**, 183 (2000).

[105] H. D. Politzer, *Reliable Perturbative Results for Strong Interactions?*, Phys. Rev. Lett. **30**, 1346 (1973).

[106] D. J. Gross and F. Wilczek, *Asymptotically Free Gauge Theories. I*, Phys. Rev. D **8**, 3633 (1973).

[107] S. Bethke, *The 2009 World Average of alpha(s)*, Eur.Phys.J. **C64**, 689 (2009).

[108] O. Kaczmarek, F. Karsch, F. Zantow, and P. Petreczky, *Static quark anti-quark free energy and the running coupling at finite temperature*, Phys.Rev. **D70**, 074505 (2004).

[109] O. Kaczmarek and F. Zantow, *Static quark anti-quark interactions in zero and finite temperature QCD. I. Heavy quark free energies, running coupling and quarkonium binding*, Phys.Rev. **D71**, 114510 (2005).

[110] J. Braun and H. Gies, *Running coupling at finite temperature and chiral symmetry restoration in QCD*, Phys.Lett. **B645**, 53 (2007).

[111] A. Peshier, *Running coupling and screening in the (s)QGP*, (2006).

[112] D. H. Oaknin and A. Zhitnitsky, *Baryon asymmetry, dark matter and quantum chromodynamics*, Phys.Rev. **D71**, 023519 (2005).

[113] N. Borghini, W. Cottingham, and R. Vinh Mau, *Possible cosmological implications of the quark hadron phase transition*, J.Phys. **G26**, 771 (2000).

[114] M. Giovannini, *Cosmological magnetogenesis: What we know and what we would like to know*, (2001).

[115] J.-L. Han and R. Wielebinski, *Milestones in the observations of cosmic magnetic fields*, Chin.J.Astron.Astrophys. **2**, 293 (2002).

[116] M. Buballa, *NJL model analysis of quark matter at large density*, Phys.Rept. **407**, 205 (2005).

[117] M. G. Alford, A. Schmitt, K. Rajagopal, and T. Schäfer, *Color superconductivity in dense quark matter*, Rev.Mod.Phys. **80**, 1455 (2008).

[118] A. Adare *et al.*, *Energy Loss and Flow of Heavy Quarks in Au+Au Collisions at s(NN)**(1/2) = 200-GeV*, Phys.Rev.Lett. **98**, 172301 (2007).

[119] B. Abelev *et al.*, *Centrality dependence of charged hadron and strange hadron elliptic flow from s(NN)**(1/2) = 200-GeV Au + Au collisions*, Phys.Rev. **C77**, 054901 (2008).

[120] K. Aamodt *et al.*, *Elliptic flow of charged particles in Pb-Pb collisions at 2.76 TeV*, Phys.Rev.Lett. **105**, 252302 (2010).

[121] K. Aamodt *et al.*, *Higher harmonic anisotropic flow measurements of charged particles in Pb-Pb collisions at* $\sqrt{s_{NN}}$*=2.76 TeV*, Phys.Rev.Lett. **107**, 032301 (2011).

[122] A. Adare *et al.*, *Measurements of Higher-Order Flow Harmonics in Au+Au Collisions at* $\sqrt{s_{NN}} = 200$ *GeV*, Phys.Rev.Lett. **107**, 252301 (2011).

[123] M. A. Stephanov, K. Rajagopal, and E. V. Shuryak, *Event-by-event fluctuations in heavy ion collisions and the QCD critical point*, Phys.Rev. **D60**, 114028 (1999).

[124] B. Alver and G. Roland, *Collision geometry fluctuations and triangular flow in heavy-ion collisions*, Phys.Rev. **C81**, 054905 (2010).

[125] B. Schenke, S. Jeon, and C. Gale, *Elliptic and triangular flow in event-by-event (3+1)D viscous hydrodynamics*, Phys.Rev.Lett. **106**, 042301 (2011).

[126] M. Luzum and P. Romatschke, *Conformal Relativistic Viscous Hydrodynamics: Applications to RHIC results at s(NN)**(1/2) = 200-GeV*, Phys.Rev. **C78**, 034915 (2008).

[127] H. Song and U. W. Heinz, *Extracting the QGP viscosity from RHIC data - A Status report from viscous hydrodynamics*, J.Phys. **G36**, 064033 (2009).

[128] T. Schäfer and D. Teaney, *Nearly Perfect Fluidity: From Cold Atomic Gases to Hot Quark Gluon Plasmas*, Rept.Prog.Phys. **72**, 126001 (2009).

[129] M. A. York and G. D. Moore, *Second order hydrodynamic coefficients from kinetic theory*, Phys.Rev. **D79**, 054011 (2009).

[130] J. I. Kapusta, *Strongly interacting low viscosity matter created in heavy ion collisions*, J.Phys. **G34**, S295 (2007).

[131] S. Jeon, *Hydrodynamic transport coefficients in relativistic scalar field theory*, Phys.Rev. **D52**, 3591 (1995).

[132] G. Aarts and J. M. Martinez Resco, *Transport coefficients, spectral functions and the lattice*, JHEP **0204**, 053 (2002).

[133] G. Aarts and J. M. Martinez Resco, *Transport coefficients from the 2PI effective action*, Phys.Rev. **D68**, 085009 (2003).

[134] G. Aarts and J. M. Martinez Resco, *Shear viscosity in the O(N) model*, JHEP **0402**, 061 (2004).

[135] A. Dobado, F. J. Llanes-Estrada, and J. M. Torres-Rincon, *Minimum of eta/s and the phase transition of the Linear Sigma Model in the large-N limit*, Phys.Rev. **D80**, 114015 (2009).

[136] M. A. Valle Basagoiti, *Transport coefficients and ladder summation in hot gauge theories*, Phys.Rev. **D66**, 045005 (2002).

[137] R. Baier, P. Romatschke, D. T. Son, A. O. Starinets, and M. A. Stephanov, *Relativistic viscous hydrodynamics, conformal invariance, and holography*, JHEP **0804**, 100 (2008).

[138] J. M. Maldacena, *The Large N limit of superconformal field theories and supergravity*, Adv.Theor.Math.Phys. **2**, 231 (1998).

[139] G. Policastro, D. T. Son, and A. O. Starinets, *The Shear viscosity of strongly coupled N=4 supersymmetric Yang-Mills plasma*, Phys.Rev.Lett. **87**, 081601 (2001).

[140] A. Buchel, J. T. Liu, and A. O. Starinets, *Coupling constant dependence of the shear viscosity in N=4 supersymmetric Yang-Mills theory*, Nucl.Phys. **B707**, 56 (2005).

[141] P. Kovtun, D. T. Son, and A. O. Starinets, *Holography and hydrodynamics: Diffusion on stretched horizons*, JHEP **0310**, 064 (2003).

[142] L. P. Csernai, J. Kapusta, and L. D. McLerran, *On the Strongly-Interacting Low-Viscosity Matter Created in Relativistic Nuclear Collisions*, Phys.Rev.Lett. **97**, 152303 (2006).

[143] R. A. Lacey, N. Ajitanand, J. Alexander, P. Chung, W. Holzmann, *et al.*, *Has the QCD Critical Point been Signaled by Observations at RHIC?*, Phys.Rev.Lett. **98**, 092301 (2007).

[144] A. Jakovac, *Non-universal lower bound for the shear viscosity to entropy density ratio*, Phys.Rev. **D81**, 045020 (2010).

[145] M. Brigante, H. Liu, R. C. Myers, S. Shenker, and S. Yaida, *Viscosity Bound Violation in Higher Derivative Gravity*, Phys.Rev. **D77**, 126006 (2008).

[146] A. Nakamura and S. Sakai, *Viscosities of hot gluon: A Lattice QCD study*, Nucl.Phys. **A774**, 775 (2006).

[147] H. B. Meyer, *High-Precision Thermodynamics and Hagedorn Density of States*, Phys.Rev. **D80**, 051502 (2009).

[148] J.-W. Chen, M. Huang, Y.-H. Li, E. Nakano, and D.-L. Yang, *Phase Transitions and the Perfectness of Fluids*, Phys.Lett. **B670**, 18 (2008).

[149] A. Dobado, F. J. Llanes-Estrada, and J. M. Torres-Rincon, *eta/s and phase transitions*, Phys.Rev. **D79**, 014002 (2009).

[150] Y. Kats and P. Petrov, *Effect of curvature squared corrections in AdS on the viscosity of the dual gauge theory*, JHEP **0901**, 044 (2009).

[151] T. D. Cohen, *Is There a "Most Perfect Fluid" Consistent with Quantum Field Theory?*, Phys. Rev. Lett. **99**, 021602 (2007).

[152] A. Cherman, T. D. Cohen, and P. M. Hohler, *A Sticky business: The Status of the cojectured viscosity/entropy density bound*, JHEP **0802**, 026 (2008).

[153] J.-W. Chen, C.-T. Hsieh, and H.-H. Lin, *Minimum Shear Viscosity over Entropy Density at Phase Transition?: A Counterexample*, Phys.Lett. **B701**, 327 (2011).

[154] A. Das, *Finite temperature field theory*, volume 16, World Scientific, 1997.

[155] M. Le Bellac, *Thermal field theory*, Cambridge University Press, 2000.

[156] J. C. Mather, E. Cheng, R. Shafer, C. Bennett, N. Boggess, *et al.*, *A Preliminary measurement of the Cosmic Microwave Background spectrum by the Cosmic Background Explorer (COBE) satellite*, Astrophys.J. **354**, L37 (1990).

[157] D. Kirzhnits, *Weinberg model in the hot universe*, JETP Lett. **15**, 529 (1972).

[158] D. Kirzhnits and A. D. Linde, *Macroscopic Consequences of the Weinberg Model*, Phys.Lett. **B42**, 471 (1972).

[159] J. Lattimer and M. Prakash, *The physics of neutron stars*, Science **304**, 536 (2004).

[160] T. Matsubara, *A New approach to quantum statistical mechanics*, Prog.Theor.Phys. **14**, 351 (1955).

[161] J. Plemelj, *Problems in the sense of Riemann and Klein*, Interscience tracts in pure and applied mathematics, Interscience Publishers, 1964.

[162] J. Blaizot and E. Iancu, *QCD Perspectives on Hot and Dense Matter*, NATO science series: Mathematics, physics, and chemistry, Springer Netherlands, 2002.

[163] J. M. Martin-Garcia, *xtensor package*.

[164] B. R. FRIEDEN, *Restoring with Maximum Likelihood and Maximum Entropy*, J. Opt. Soc. Am. **62**, 511 (1972).

[165] R. Silver, D. Sivia, and J. Gubernatis, *Maximum-entropy method for analytic continuation of quantum Monte Carlo data*, Phys.Rev. **B41**, 2380 (1990).

[166] J. Gubernatis, M. Jarrell, R. Silver, and D. Sivia, *Quantum Monte Carlo simulations and maximum entropy: Dynamics from imaginary-time data*, Phys.Rev. **B44**, 6011 (1991).

[167] K. Sasaki, S. Sasaki, T. Hatsuda, and M. Asakawa, *Excited nucleon spectrum from lattice QCD with maximum entropy method*, Nucl.Phys.Proc.Suppl. **129**, 212 (2004).

[168] S. Ejiri and T. Hatsuda, *QCD level density from maximum entropy method*, PoS **LAT2005**, 183 (2006).

[169] M. Imachi, Y. Shinno, and H. Yoneyama, *Lattice field theory with the sign problem and the maximum entropy method*, SIGMA **3**, 018 (2007).

[170] P. Gubler, K. Suzuki, K. Morita, and M. Oka, *Modification of hadronic spectral functions under extreme conditions: An approach based on QCD sum rules and the maximum entropy method*, Nucl.Phys. **A914**, 512 (2013).

[171] C. P. Coughlan and D. C. Gabuzda, *Imaging VLBI polarimetry data from Active Galactic Nuclei using the Maximum Entropy Method*, EPJ Web Conf. **61**, 07009 (2013).

[172] H. J. Pirner, *Azimuthal Anisotropy in Heavy Ion Collisions from the Maximum Entropy Method*, (2014).

[173] F. Karsch and H. W. Wyld, *Thermal Green's functions and transport coefficients on the lattice*, Phys. Rev. D **35**, 2518 (1987).

[174] C. Shannon, *A Mathematical Theory of Communication*, Bell System Technical Journal **27**, 379 (1948).

[175] E. Jaynes, *Information Theory and Statistical Mechanics. II*, Phys.Rev. **108**, 171 (1957).

[176] E. Jaynes, *Information Theory and Statistical Mechanics*, Phys.Rev. **106**, 620 (1957).

[177] J. Bernardo and A. Smith, *Bayesian Theory*, Wiley Series in Probability and Statistics, Wiley, 2009.

[178] G. Golub and C. Reinsch, *Singular value decomposition and least squares solutions*, Numerische Mathematik **14**, 403.

[179] D. W. Marquardt, *An algorithm for least-squares estimation of nonlinear parameters*, Journal of the Society for Industrial & Applied Mathematics **11**, 431 (1963).

[180] L. Fister and J. M. Pawlowski, *Yang-Mills correlation functions at finite temperature*, (2011).

[181] C. S. Fischer, A. Maas, and J. M. Pawlowski, *On the infrared behavior of Landau gauge Yang-Mills theory*, Annals Phys. **324**, 2408 (2009).

[182] A. Maas, *Gluons at finite temperature in Landau gauge Yang-Mills theory*, Mod.Phys.Lett. **A20**, 1797 (2005).

[183] A. Maas, *Describing gauge bosons at zero and finite temperature*, Phys.Rept. **524**, 203 (2013).

[184] J. M. Cornwall, *Positivity violations in QCD*, Mod.Phys.Lett. **A28**, 1330035 (2013).

[185] H. Berrehrah, , for the PHSD group, private communication.

[186] R. Haussmann, M. Punk, and W. Zwerger, *Spectral functions and rf response of ultracold fermionic atoms*, Phys. Rev. A **80**, 063612 (2009).

[187] S. Strauss, C. S. Fischer, and C. Kellermann, *Analytic structure of the Landau gauge gluon propagator*, Phys.Rev.Lett. **109**, 252001 (2012).

[188] T. Yamazaki *et al.*, *Spectral function and excited states in lattice QCD with maximum entropy method*, Phys.Rev. **D65**, 014501 (2002).

[189] S.-x. Qin and D. H. Rischke, *Quark spectral function and deconfinement at nonzero temperature*, Phys. Rev. D **88**, 056007 (2013).

[190] E. Braaten and R. D. Pisarski, *Soft Amplitudes in Hot Gauge Theories: A General Analysis*, Nucl.Phys. **B337**, 569 (1990).

[191] J. Blaizot, E. Iancu, and A. Rebhan, *Selfconsistent hard thermal loop thermodynamics for the quark gluon plasma*, Phys.Lett. **B470**, 181 (1999).

[192] S. Borsanyi, G. Endrodi, Z. Fodor, S. Katz, and K. Szabo, *Precision SU(3) lattice thermodynamics for a large temperature range*, JHEP **1207**, 056 (2012).

[193] L. Fister and J. M. Pawlowski, *Confinement from Correlation Functions*, Phys.Rev. **D88**, 045010 (2013).

[194] S. C. Huot, S. Jeon, and G. D. Moore, *Shear viscosity in weakly coupled $N = 4$ super Yang-Mills theory compared to QCD*, Phys.Rev.Lett. **98**, 172303 (2007).

[195] H. B. Meyer, *A Calculation of the shear viscosity in SU(3) gluodynamics*, Phys.Rev. **D76**, 101701 (2007).

[196] H. B. Meyer, *Transport properties of the quark-gluon plasma from lattice QCD*, Nucl.Phys. **A830**, 641C (2009).

[197] P. B. Arnold, G. D. Moore, and L. G. Yaffe, *Transport coefficients in high temperature gauge theories. 1. Leading log results*, JHEP **0011**, 001 (2000).

[198] P. B. Arnold, G. D. Moore, and L. G. Yaffe, *Transport coefficients in high temperature gauge theories. 2. Beyond leading log*, JHEP **0305**, 051 (2003).

[199] M. Bluhm, B. Kampfer, and K. Redlich, *Bulk and shear viscosities of the gluon plasma in a quasiparticle description*, Phys.Rev. **C84**, 025201 (2011).

[200] N. Demir and S. A. Bass, *Shear-Viscosity to Entropy-Density Ratio of a Relativistic Hadron Gas*, Phys. Rev. Lett. **102**, 172302 (2009).

[201] P. Huovinen and P. Petreczky, *{QCD} equation of state and hadron resonance gas*, Nuclear Physics A **837**, 26 (2010).

[202] J. Noronha-Hostler, J. Noronha, and C. Greiner, *Hadron Mass Spectrum and the Shear Viscosity to Entropy Density Ratio of Hot Hadronic Matter*, Phys.Rev. **C86**, 024913 (2012).

[203] A. Rothkopf, *Improved Maximum Entropy Method with an Extended Search Space*, PoS **LATTICE2012**, 100 (2012).

[204] Y. Burnier and A. Rothkopf, *A new Bayesian approach to the reconstruction of spectral functions*, (2013).

[205] Y. Burnier and A. Rothkopf, *Benchmarking the Bayesian reconstruction of the non-perturbative heavy $Q\bar{Q}$ potential*, PoS **LATTICE2013**, 491 (2014).

Acknowledgements

Over the course of the recent years of my doctoral studies I have received support and encouragement from a number of people and organizations. I wish to seize the opportunity to express my gratitude.
First of all, I want to thank my supervisor Prof. Jan M. Pawlowski for granting me the opportunity to be part of his research team in an intriguing field of physics. His guidance and experience helped me greatly to finalize this thesis in its current form.

I further want to thank Dr. Leonard Fister for providing finite temperature SU(3) gluon propagators, which were the basis of my analysis. Discussions help me to understand the features of and challenges for the Functional Renormalisation Group a lot better. He also is greatly acknowledged for his collaboration on publications.

My thanks go to Dr. Nils Strodthoff and Nicolai Christiansen, who strived with me in the tedious task of extending the one-loop study of transport coefficients to the two-loop level. In this time we encountered many drawbacks and new challenges, that deepened my understanding of numerics and calculus. Collaborating with Nils and Nicolai was a unique pleasure and is well remembered.

Special thanks are directed to Prof. Axel Maas, who invited me to Jena, to learn basic concepts of lattice simulations in non-Abelian gauge theories. Not only, did he invest his time in many discussions, but also gave me a beautiful tour of the city.

Fruitful discussions with Dr. Alexander Rothkopf increased my insights into the Maximum Entropy Method. I want to thank him for pointing out validity checks to me, that I was not aware of before.

For financial support, I wish to acknowledge the Landesgraduiertenförderung Baden-Württemberg via the Research Training Group "Quantum Many-body Dynamics and Nonequilibrium Physics", who granted me a scholarship in my first years.

In addition I want to thank the Institut für theoretische Physik and Prof. Jan M. Pawlowski for extending my financial support to the end of my doctoral studies.

Highly appreciated is the support of the members of the secretaries office at Philosophenweg 16, who had answers to all the problems, theoretical physicists cannot deal on their own.

I want to express my invaluable gratitude to my family, whose support has always been unwavering and unconditionally. In particular, my mother, Marianne Haas, was always there for me, when help was needed.

I probably would not be where I am today without Frank-Martin Haas, who inspired my desire for physics and stimulated my sense of logic very early in my life.

Last, but not least, my deepest thanks and appreciation are for my girlfriend Paolina Manolova. She is the most special person I have ever met, and I am in love with her for many years now. She is always at my side, and the best advisor I know.